Synthesis, Assembly and Thermo-Responsivity of Polymer-Functionalized Magnetic Cobalt Nanoparticles

Li Tan
Geb. 05.09.1988

Univ.-Diss.

zur Erlangung des akademischen Grades
"doctor rerum naturalium"
(Dr. rer. nat.)
in der Wissenschaftsdisziplin "Polymerchemie"

eingereicht an der
Mathematisch-Naturwissenschaftlichen Fakultät
Institut für Chemie
der Universität Potsdam

Potsdam, October 2, 2018
Hauptbetreuer: Prof. Dr. Alexander Böker
weitere Gutachter: Prof. Dr.Andreas Taubert, Prof. Dr. Michael Maskos

Try not to become a man of success, rather than becoming a man of value.

Albert Einstein

Published online at the
Institutional Repository of the University of Potsdam:
URN urn:nbn:de:kobv:517-opus4-418153
http://nbn-resolving.de/urn:nbn:de:kobv:517-opus4-418153

Erklärung

Hiermit erkläre ich, dass ich die beigefügte Dissertation selbstständig verfasst und keine anderen als die angegebenen Hilfsmittel genutzt habe. Alle inhaltlich übernommenen Stellen habe ich als solche gekennzeichnet.

Ich versichere außerdem, dass ich die Dissertation nur in diesem und keinem anderen Promotionsverfahren eingereicht habe und, dass diesem Promotionsverfahren keine endgültig gescheiterten Promotionsverfahren vorausgegangen sind.

Potsdam, 17. June. 2018. Li Tan

Publications and Posters

Publications:

[1] **Li Tan**, Bing Liu, Konrad Siemensmeyer, Ulrich Glebe, Alexander Böker. Synthesis of thermo-responsive nanocomposites of superparamagnetic cobalt nanoparticles/poly(*N*-isopropylacrylamide). *J. Colloid Interface Sci.*, **2018**, *526*, 124-134.

[2] **Li Tan**, Bing Liu, Konrad Siemensmeyer, Ulrich Glebe, Alexander Böker. Synthesis of superparamagnetic and ferromagnetic cobalt nanoparticles by varying the stabilizing polymeric surfactant. *Polymers*, **2018**, *10*, 1053.

[3] **Li Tan**, Bing Liu, Ulrich Glebe, Alexander Böker. Magnetic-field-induced assembly of superparamagnetic cobalt nanoparticles at liquid-air interface. **2018**, (revised).

Conference Posters:

[1] Synthesis of Thermo-Responsive Nanocomposites of Superparamagnetic Cobalt Nanoparticles
L. Tan, B. Liu, U. Glebe, A. Böker
"Kolloid-Tagung Multiresponsive Systems", München, 9–11.October.2017

[2] Synthesis and Assembly of Responsive Cobalt Nanoparticles
L. Tan, B. Liu, U. Glebe, A. Böker
Polydays, Potsdam, 28–30.September.2016

Contents

Abbreviations

Materials

α-CD	α-cyclodextrin
BIBB	α-bromoisobutyryl bromide
Boc	*Tert*-butyloxycarbonyl
DCB	Dichlorobenzene
DCM	Dichloromethane
DDAB	Didodecyldimethylammonium bromide
DMF	*N,N*-dimethylformamide
DMSO	Dimethyl sulfoxide
DOA	Dioctylamine
DPA	Dopamine
GAL	4-gallic acid
HBA	Hydroxybenzoic acid
HPP	3-(4-hydroxyphenyl)propionic acid
MEMA	Methoxyethylmethacrylate
Me_6TREN	Tris[2-(dimethylamino)ethyl]amine
NIPAM	*N*-isopropylacrylamide
$NOBF_4$	Nitrosonium tetrafluoroborate
OA	Oleic acid
OEGMA	Oligo(ethyleneglycol)methylethermethacrylate
PAA-PS	Poly(acrylic acid)-*block*-polystyrene
TDA	Tridodecylamine
PDEAAM	Poly (*N,N*-diethylacrylamide)
PDEAEMA	Poly(*N,N*-diethylaminoethyl methacrylate)
PDEAEAM	Poly[*N*-[2- (diethylamino)ethyl acrylamide]
PDMAEMA	Poly(*N,N*-dimethylaminoethyl methacrylate)
PEG	Polyethylene glycol
TMAOH	Tetramethylammonium hydroxide
PNIPAM	Poly(*N*-isopropylacrylamide)
TOP	Trioctylphosphine
TOPO	Trioctylphosphine oxide
PS-*b*-PEO	Poly(styrene-*b*-ethylene oxide)
PS	Polystyrene
P(MMA-*r*-EA-*r*-VPy)	Methyl methacrylate-*random*-ethyl acrylate-*random*-*N*-vinyl-pyrrolidone
$P(MOE_2MA_x–OEGMA_y)$	Poly(co-2-(2-methoxyethoxy)ethylmethacrylate)$_x$–hydroxyl-terminated oligo(ethylene glycol) methacrylate)$_y$

Characterization and measurements:

ATR	Attenuated total reflection
BIM	Brewster angle microscopy
DC	Direct current
DLS	Dynamic light scattering
FT-IR	Fourier transform infrared
GPC	Gel permeation chromatography
GISAXS	Grazing incidence small-angle X-ray scattering
^{1}H-NMR	Proton nuclear magnetic resonance
MALDI-ToF	Matrix-assisted laser desorption/ionization time-of-flight
SEM	Scanning electron microscopy
SFM	Scanning force microscopy
SQUID	Superconducting quantum interference device
TEM	Transmission Electron Microscopy
TGA	Thermogravimetric analysis
WAXS	Wide angle X-ray Scattering
XPS	X-ray photoelectron spectroscopy
XRR	X-ray reflectivity

General abbreviations and symbols:

1-D	One-dimensional
2-D	Two-dimensional
3-D	Three-dimensional
AC	Alternating current
ATRP	Atom transfer radical polymerization
CRP	Controlled radical polymerization
ρ	Density
ε	Epsilon
Fcc	Face-centered-cubic
FC	Field cooling
H	Magnetic field
Hc	Coercivity
Hcp	Hexagonal closed-packed
HOPG	Highly oriented pyrolytic graphite
LB	Langmuir-Blodgett
LCST	Lower critical solution temperature
$M_{(org)}$	Molecular weight of initiator or polymer

MNPs	Magnetic nanoparticles
MRI	Magnetic resonance imaging
Mr	Remanence magnetization
Ms	Saturation magnetization
N_A	Avogadro's number
NPs	Nanoparticles
NMP	Nitroxide-mediated polymerization
$N_{(NPs)}$	Number of Co NPs respectively
$N_{(org)}$	Number of initiator or polymer
PDI	Polydispersity index
R	Radius
RAFT	Reversible addition-fragmentation chain transfer
RCA	Radio Corporation of America
SI-ATRP	Surface-initiated atom transfer radical polymerization
$S_{(NPs)}$	Surface area of NPs
SPM	Superparamagnetic
T_C	Cloud point temperature
V	Volume
VPTT	Volume phase transition temperature
$W_{(org)}$	Weight loss percentage of initiator or polymer
$W_{(NPs)}$	Weight percentage of Co NPs
χ	Volume susceptibility
ZFC	Zero-field cooling

Units:

a.u.	Arbitrary units
Da	Dalton
K	Kelvin
mM	Milimolar
nm	Nanometer
T	Tesla

1 Motivation

Nanomaterials are defined as materials with at least one dimension in the range of 1-100 nanometers. In the last few decades, nanomaterials have shown great influence on modern science and have been used in many fields such as information storage,[1–3] energy storage,[4,5] food industry,[6] sensing,[7–9] catalysis,[10,11] biomedicine[12] and coatings.[13,14] Among all types of nanomaterials, magnetic nanoparticles (MNPs) are one of the most widely investigated types of nanoparticles in biomedicine. The unique properties of MNPs derive from the high surface-to-volume ratio of these nanoscale magnets which differ from their bulk materials. The extensive use of MNPs in biological imaging, therapeutic applications and magnetic energy storage is mainly attributed to their outstanding magnetic features.[15–18] The magnetic properties of ferromagnetic NPs are dominated by a hysteresis loop showing remanence and coercivity. When the size of such NPs is reduced below a critical diameter, the particles become superparamagnetic.[19] In contrast to the hysteresis loop of ferromagnetic materials, the superparamagnetic nanoparticles have zero coercivity. This means that they are magnetized in an external magnetic field and reach their saturation magnetization rapidly, but no residual magnetization remains once the field has been removed. This makes superparamagnetic (SPM) NPs especially interesting for biological applications, because they do not agglomerate in the body after removal of the applied magnetic field, and thus there is much less concern about blood blockage and thrombosis.[20] Of various magnetic materials, cobalt, with the relatively high saturation magnetization of 161 emu/g (compared to magnetite (Fe_3O_4) of 92 emu/g),[21] have great potential applications in various fields, such as ferrofluids, high density information storage, and magnetic resonance imaging (MRI).[22–24]

High-density information storage is one of the most promising applications for magnetic nanoparticles. Magnetic devices made from magnetic nanoparticles show a more dense data storage capability even than the hard drives in the most advanced computers. This requires a stable magnetization of highly ordered superstructures.[25,26] In this case, a deep understanding the assembly behavior of magnetic nanoparticles is essential for the design of magnetic media with high density storage. The assembly of magnetic nanoparticles induced by magnetic field has the big advantage that the magnetic field can be controlled remotely and the response of MNPs to magnetic field is fast.[27,28] Although numerous studies have been reported for the magnetic-field-induced assembly of magnetic nanoparticles into 1-D superstructures,[29–34] a deeper and overall investigation of the assembly behavior of MNPs is of great significance.

Nanoparticles tend to agglomerate which would restrict their applicability. In order to prevent MNPs from agglomeration, surfactants like small molecules (e.g., oleic acid, trioctylphosphine oxide and oleylamine) have been widely used as. surfactants to stabilize MNPs.[35,36] The ligands not only provide protection against oxidation and aggregation, but also can affect the growth of MNPs.[37–41] In addition to small molecules as surfactants, several examples for the synthesis of magnetic nanoparticles with polymer shells have also been reported.[42–44] On the one hand, the polymeric surfactants provide advantages over small molecules due to the stronger repulsive force to stabilize magnetic nanoparticles.[45] On the other hand, the

composition of the polymer can be tuned through copolymerization or post-functionalization. Furthermore, the development of controlled/living free radical polymerization enables the synthesis of a wide range of polymers with precise molecular weight and composition, which exhibits prominent advantages for the synthesis of magnetic nanoparticles/shell hybrids with tunable thickness and composition.[42,46] Therefore, the synthesis of polymer-coated Co NPs will be studied in this work.

In general, monodisperse and well-defined MNPs are synthesized via a thermolysis of metal precursors by using hydrophobic small molecules as surfactants. However, their biological applications, which require dispersion in hydrophilic or aqueous media, are limited.[47,48] Thus, there is a great significance in the surface modification of hydrophobic nanoparticles. Meanwhile, polymers cannot only stabilize nanoparticles, moreover, they can impart further functionality. For instance, stimuli-responsive polymers are responsive to stimuli, such as temperature, pH, light and electric / magnetic field.[49–54] Such smart polymers have been applied in many fields, including medicine and biology.[55,56] Among the above mentioned smart polymers, temperature-responsive polymers are the most studied. Some of the thermo-responsive polymers have a lower critical solution temperature (LCST), below which the polymer is homogeneously dissolved in aqueous medium, and above it, the polymer exhibits a phase separation with the solvent.[57–59] The combination of superparamagnetic and thermo-responsive properties in hybrid nanoparticles would be promising for future applications e.g. in biomedicine.

References

1. Affronte, M. Molecular nanomagnets for information technologies. *J. Mater. Chem.* **19,** 1731–1737 (2009).
2. Tseng, R. J. *et al.* Digital memory device based on tobacco mosaic virus conjugated with nanoparticles. *Nat. Nanotechnol.* **1,** 72–77 (2006).
3. Sellmyer, D. & Skomski, R. *Advanced Magnetic Nanostructures*. (Springer, 2006).
4. Seayad, A. M. & Antonelli, D. M. Recent advances in hydrogen storage in metal-containing inorganic nanostructures and related materials. *Adv. Mater.* **16,** 765–777 (2004).
5. Dresselhaus, M.S.; Thomas, I. . Alternative energy technologies. *Nature* **414,** 332–337 (2001).
6. Dingman, J. Nanotechnology: its impact on food safety. *J. Environ. Health* **70,** 47–50 (2008).
7. Kong, J. *et al.* Nanotube molecular wires as sensors. *Science.* **287,** 622–625 (2000).
8. Collins, P. G., Bradley, K., Ishigami, M. & Zettl, A. Extreme oxygen sensitivity of electronic properties of carbon nanotubes. *Science.* **287,** 1801–1805 (2000).
9. Ansari, A. A., Alhoshan, M., Alsalhi, M. S. & Aldwayyan, A. S. Prospects of nanotechnology in clinical immunodiagnostics. *Sensors* **10,** 6535–6581 (2010).
10. Enterkin, J. A., Poeppelmeier, K. R. & Marks, L. D. Oriented catalytic platinum nanoparticles on high surface area strontium titanate nanocuboids. *Nano Lett.* **11,** 993–997 (2011).
11. Galvis, H. M. T. Supported iron nanoparticles as. *Science.* **835,** 1–5 (2012).
12. Farokhzad, O. C. & Langer, R. Impact of nanotechnology on drug delivery. *ACS Nano* **3,** 16–20

(2009).

13. Feil, F., Fürbeth, W. & Schütze, M. Nanoparticle based inorganic coatings for corrosion protection of magnesium alloys. *Surf. Eng.* **24,** 198–203 (2008).
14. Lee, D., Rubner, M. F. & Cohen, R. E. All-nanoparticle thin-film coatings. *Nano Lett.* **6,** 2305–2312 (2006).
15. de Dios, A. S. & Díaz-García, M. E. Multifunctional nanoparticles:analytical prospects. *Anal. Chim. Acta* **666,** 1–22 (2010).
16. Frey, N. A., Peng, S., Cheng, K. & Sun, S. Magnetic nanoparticles:synthesis, functionalization, and applications in bioimaging and magnetic energy storage. *Chem. Soc. Rev.* **38,** 2532 (2009).
17. Corot, C., Robert, P., Idée, J. M. & Port, M. Recent advances in iron oxide nanocrystal technology for medical imaging. *Adv. Drug Deliv. Rev.* **58,** 1471–1504 (2006).
18. Mornet, S., Vasseur, S., Grasset, F. & Duguet, E. Magnetic nanoparticle design for medical diagnosis and therapy. *Forunal Mater. Chem.* **14,** 2161–2175 (2004).
19. Kolhatkar, A. G., Jamison, A. C., Litvinov, D., Willson, R. C. & Lee, T. R. Tuning the magnetic properties of nanoparticles. *Int. J.Mol. Sci.***14,** 15977–16009 (2013).
20. Akbarzadeh, A., Samiei, M. & Davaran, S. Magnetic nanoparticles: preparation, physical properties, and applications in biomedicine. *Nanoscale Res. Lett.* **7,** 144 (2012).
21. Zalich, M. A., Vadala, M. L., Riffle, J. S., Saunders, M. & St. Pierre, T. G. Structural and magnetic properties of cobalt nanoparticles encased in siliceous shells.*Chem. Mater.* **19,** 6597–6604 (2007).
22. Shimizu, T. Fabrication of pulsatile cardiac tissue grafts using a novel 3-dimensional cell sheet manipulation technique and temperature-responsive cell culture surfaces. *Circ. Res.* **90,** e40–e48 (2002).
23. Dumestre, F. *et al.* Shape control of thermodynamically stable cobalt nanorods through organometallic chemistry. *Angew. Chemie - Int. Ed.* **41,** 4286–4289 (2002).
24. Parkes, L. M. *et al.* Cobalt nanoparticles as a novel magnetic resonance contrast agent-relaxivities at 1.5 and 3 Tesla. *Contrast Media Mol. I.* **3,** 150–156 (2008).
25. Reiss, G. & Hütten, A. Magnetic nanoparticles:applications beyond data storage. *Nat. Mater.* **4,** 725–726 (2005).
26. Sun, S., Murray, C. B., Weller, D., Folks, L. & Moser, A. Monodisperse FePt nanoparticles and ferromagnetic FePt nanocrystal superlattices. *Science.* **287,** 1989–1992 (2000).
27. Timonen, J. V. I., Latikka, M., Leibler, L., Ras, R. H. A. & Ikkala, O. Switchable static and dynamic self-assembly of magnetic droplets on superhydrophobic surfaces. *Science.* **341,** 253–257 (2013).
28. Cho, M. H. *et al.* A magnetic switch for the control of cell death signalling in in vitro and in vivo systems. *Nat. Mater.* **11,** 1038–1043 (2012).
29. Singamaneni, S., Bliznyuk, V. N., Binek, C. & Tsymbal, E. Y. Magnetic nanoparticles: recent advances in synthesis, self-assembly and applications. *J. Mater. Chem.* **21,** 16819 (2011).
30. Ngo, A. T. & Pileni, M. P. Cigar-shaped ferrite nanocrystals: Orientation of the easy magnetic

axes. *J. Appl. Phys.* **92,** 4649–4652 (2002).

31. Pileni, M. P. Nanocrystal self-assemblies:fabrication and collective properties. *J. Phys. Chem. B* **105,** 3358–3371 (2001).
32. Wiedwald, U., Spasova, M., Farle, M., Hilgendorff, M. & Giersig, M. Ferromagnetic resonance of monodisperse Co particles. *J. Vac. Sci. Technol. A Vacuum, Surfaces, Film.* **19,** 1773–1776 (2001).
33. Sahoo, Y. *et al.* Field-directed self-assembly of magnetic nanoparticles. 3380–3383 (2004).
34. Ngo, A. T. & Pileni, M. P. Assemblies of ferrite nanocrystals:partial orientation of the easy magnetic axes. *J. Phys. Chem. B.* 53–58 (2001).
35. Kang, Y. & Murray, C. B. Synthesis and electrocatalytic properties of cubic Mn-Pt nanocrystals (nanocubes). *J. Am. Chem. Soc.* **132,** 7568–7569 (2010).
36. Park, J., Joo, J., Soon, G. K., Jang, Y. & Hyeon, T. Synthesis of monodisperse spherical nanocrystals. *Angew. Chemie-Int. Ed.* **46,** 4630–4660 (2007).
37. Puntes, V. F., Krishnan, K. M. & Alivisatos, A. P. Colloidal nanocrystal shape and size control: The case of cobalt. *Science.* **291,** 2115–2117 (2001).
38. Puntes, V. F., Krishnan, K. & Alivisatos, A. Synthesis of colloidal cobalt nanoparticles with controlled size and shapes. *Top. Catal.* **19,** 145–148 (2002).
39. Bao, Y., An, W., Heath Turner, C. & Krishnan, K. M. The critical role of surfactants in the growth of cobalt nanoparticles. *Langmuir* **26,** 478–483 (2010).
40. Bao, Y., Beerman, M., Fakhomov, A. B. & Krishnan, K. M. Controlled crystalline structure and surface stability of cobalt nanocrystals. *J. Phys. Chem. B* **109,** 7220–7222 (2005).
41. Puntes, V. F., Zanchet, D., Erdonmez, C. K. & Alivisatos, A. P. Synthesis of hcp-Co nanodisks. *J. Am. Chem. Soc.* **124,** 12874–12880 (2002).
42. Pyun, J. Nanocomposite materials from functional polymers and magnetic colloids. *Polym. Rev.* **47,** 231–263 (2007).
43. Burke, N. A. D., Stöver, H. D. H. & Dawson, F. P. Magnetic nanocomposites:preparation and characterization of polymer-coated iron nanoparticles. *Chem. Mater.* **14,** 4752–4761 (2002).
44. Leslie-Pelecky, D. L. & Rieke, R. D. Magnetic properties of nanostructured materials. *Chem. Mater.* **8,** 1770–1783 (1996).
45. Hess, P. H. & Parker, P. H. Polymers for stabilization of colloidal cobalt particles. *J. Appl. Polym. Sci.* **10,** 1915–1927 (1966).
46. Korth, B. D. *et al.* Synthesis, assembly, and functionalization of polymer-coated ferromagnetic nanoparticles. in *ACS Symposium Series* **996,** 272–285 (2008).
47. Medintz, I. L., Uyeda, H. T., Goldman, E. R. & Mattoussi, H. Quantum dot bioconjugates for imaging, labelling and sensing. *Nat. Mater.* **4,** 435–446 (2005).
48. Bruchez Jr., M. Semiconductor nanocrystals as fluorescent biological labels. *Science.* **281,** 2013–2016 (1998).
49. Tanaka, T., Nishio, I., Sun, S.-T. & Ueno-Nishio, S. Collapse of gels in an electric field. *Science.* **218,** 467–469 (1982).

50. Wei, M., Gao, Y., Li, X. & Serpe, M. J. Stimuli-responsive polymers and their applications. *Polym. Chem.* **8,** 127–143 (2017).

51. Thévenot, J., Oliveira, H., Sandre, O. & Lecommandoux, S. Magnetic responsive polymer composite materials. *Chem. Soc. Rev.* **42,** 7099 (2013).

52. Dai, S., Ravi, P. & Tam, K. C. pH-Responsive polymers:synthesis, properties and applications. *Soft Matter* **4,** 435 (2008).

53. Shum, P., Kim, J. M. & Thompson, D. H. Phototriggering of liposomal drug delivery systems. *Adv. Drug Deliv. Rev.* **53,** 273–284 (2001).

54. Heskins, M. & Guillet, J. E. Solution properties of poly(*N*-isopropylacrylamide). *J. Macromol. Sci. Part A-Chem.* **2,** 1441–1455 (1968).

55. Hu, J. & Liu, S. Responsive polymers for detection and sensing applications: Current status and future developments. *Macromolecules* **43,** 8315–8330 (2010).

56. Pattanashetti, N. A., Heggannavar, G. B. & Kariduraganavar, M. Y. Smart biopolymers and their biomedical applications. *Procedia Manuf.* **12,** 263–279 (2017).

57. Zhang, Q., Weber, C., Schubert, U. S. & Hoogenboom, R. Thermoresponsive polymers with lower critical solution temperature:from fundamental aspects and measuring techniques to recommended turbidimetry conditions. *Mater. Horiz.* **4,** 109–116 (2017).

58. Gandhi, A., Paul, A., Sen, S. O. & Sen, K. K. Studies on thermoresponsive polymers:phase behaviour, drug delivery and biomedical applications. *Asian J. Pharm. Sci.* **10,** 99–107 (2015).

59. Weber, C., Hoogenboom, R. & Schubert, U. S. Temperature responsive bio-compatible polymers based on poly(ethylene oxide) and poly(2-oxazoline)s. *Prog. Polym. Sci.* **37,** 686–714 (2012).

2 Fundamentals

2.1 Overview

Magnetic nanoparticles (MNPs) are submicron moieties (with the size range of 1-100 nm) made of magnetic materials and have been widely investigated in biomedicine. The unique properties of MNPs and their applications in magnetic energy storage, biological imaging and therapeutic applications mainly derive from their magnetic properties, more precisely, their superparamagnetism.[1–4] MNPs are superparamagnetic below a critical diameter and in this case can be magnetized by an external magnetic field rapidly but no residual magnetization remains once the field has been removed.

This chapter will give an overview of the properties and recent studies on the synthesis, self-assembly, surface modification of MNPs. Various examples of the fabrication of thermo-responsive MNPs core/shell nanocomposites via surface-initiated atom transfer radical polymerization (SI-ATRP) will also be reviewed in this chapter.

2.2 Magnetic Materials

Magnetic materials consist of many magnetic dipoles. The strength and orientation of these dipoles is characteristic for different magnetic properties. Generally, based on the different response of intrinsic magnetic dipoles and the net magnetization in the presence or absence of an applied magnetic field, magnetic materials can be classified into 5 types: diamagnetic, paramagnetic, ferromagnetic, ferrimagnetic, and antiferromagnetic.[5,6] As shown in Figure 2.1, there are no magnetic dipoles in the absence of a magnetic field in diamagnetic materials, while in the presence of an external magnetic field, dipoles are induced which are directed opposite to the applied field. Paramagnetic materials consist of randomly distributed magnetic dipoles without an applied magnetic field and these dipoles are aligned in the direction of the applied magnetic field in the presence of a magnetic field. For the ferromagnetic materials, the magnetic dipoles are oriented in the same direction already without an applied magnetic field. Ferrimagnetic materials consist of antiparallel magnetic dipoles of different strength, so that a net magnetization remains in the absence of the magnetic field. However, for the antiferromagnetic materials, the adjacent antiparallel magnetic dipoles are counterbalanced in the absence of any magnetic field.

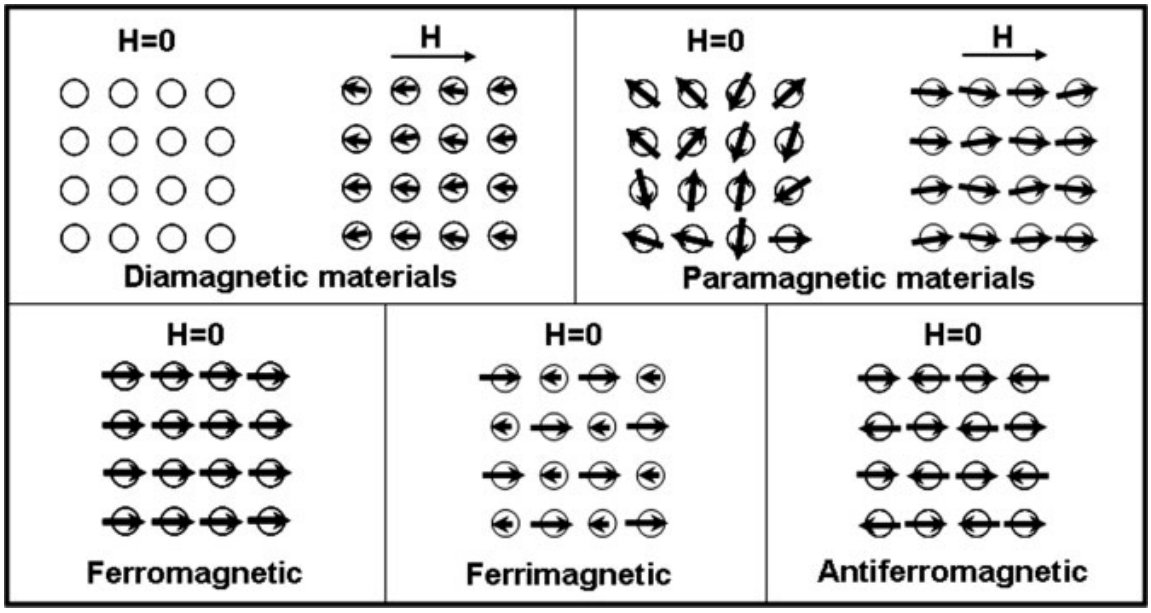

Figure 2.1 Schematic illustration of magnetic dipoles of different magnetic materials in the presence and absence of an external magnetic field. Reprinted from reference.[5]

In order to better understand the magnetic behavior, it is of fundamental importance to know some key parameters: saturation magnetization (Ms), remanence magnetization (Mr) and coercivity (Hc).[7] Diamagnetic and paramagnetic materials get magnetized in presence of an external magnetic field, each magnetic dipole is independently affected by the applied magnetic field with direction opposite or parallel to the magnetic field, respectively. The magnetization is dependent on the strength of the magnetic field and reduced to zero after removing the applied magnetic field. As shown in Figure 2.2, their overall magnetization is comparably low. The magnetization is higher for ferromagnetic materials and reaches a maximum value, which is referred to as saturation magnetization (Ms). However, the magnetization of ferromagnetic materials is not reduced to zero after removal of the applied magnetic field, and the remaining magnetization at zero field is called remanence magnetization (Mr). The intensity of the required external magnetic field to reduce the magnetization of ferromagnetic materials to zero is called coercivity (Hc). Therefore, a hysteresis loop is observed for ferromagnetic materials. Superparamagnetism exists in magnetic materials which are composed of very small crystallites. When exposed to an external magnetic field, the magnetic moment of overall crystallites aligns at the direction of the applied magnetic field, and no magnetization remains after removal of the external magnetic field. Hence, the coercivity is zero for superparamagnetic materials.

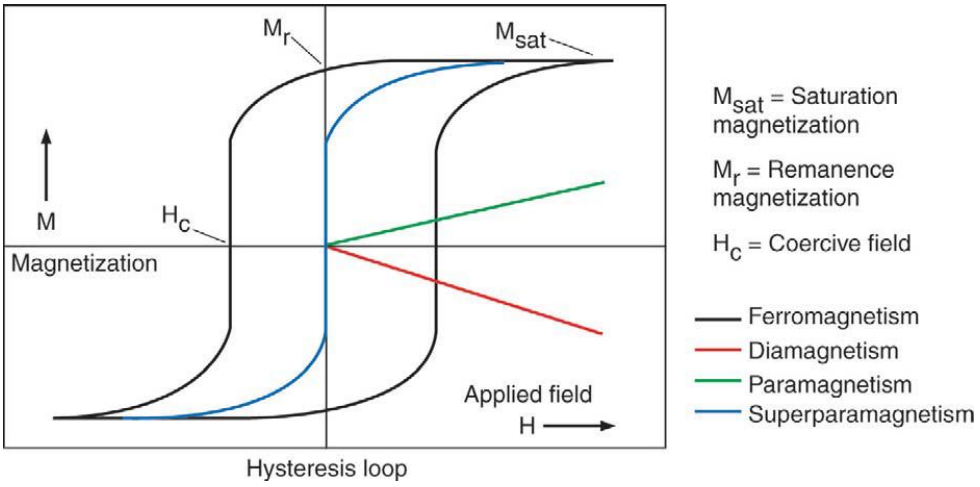

Figure 2.2 Magnetic behavior of different types of magnetic materials under the influence of an applied field, the X-axis is the applied field, and the Y-axis is the magnetization of the applied magnetic field (emu/g). Reprinted from reference.[7]

2.3 Superparamagnetic Nanoparticles (MNPs)

Due to the unique magnetic response behavior to the external magnetic field, superparamagnetic nanoparticles have been applied in many fields (e.g., biomedicine). Thus, it is of great significance to study magnetic nanoparticles in detail. The magnetic behavior of MNPs can be influenced by a lot of factors such as size,[5,7,8] and temperature.[5] As shown in Figure 2.3a, from energetic point of view, larger magnetic nanoparticles favorably form multi-domain walls. When the size of MNPs reduces to a certain value r_c, MNPs favor to be in the single-domain regime. If the size further decreases, a critical value r_0 is reached, below which MNPs exhibit superparamagnetic properties. Figure 2.3b shows different MNPs and their behavior as a function of size, for example, the r_0 for cobalt is around 10 nm.[8]

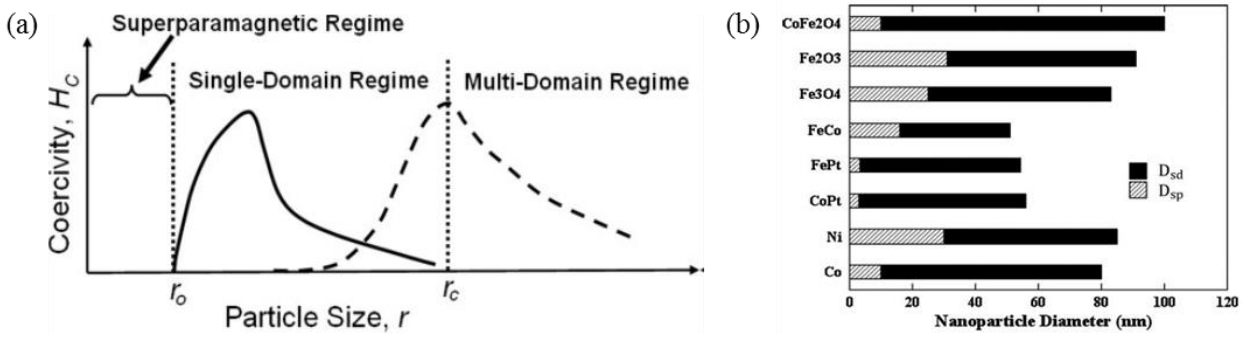

Figure 2.3 (**a**) Transition from superparamagnetic to single- to multi-domain regimes in dependence of the particle size. Reprinted from reference.[5] (**b**) Superparamagnetic regime D_{sp} and single domain regime D_{sd} for nanoparticles of different compositions. Reprinted from reference.[8]

The blocking temperature (T_B) is an important parameter to describe superparamagnetic nanoparticles. This is a transition point between the thermal energy and magnetic anisotropy energy. Experimentally, the blocking temperature value is measured from a magnetization-temperature curve. Normally, the sample is first cooled down to a very low temperature (e.g., 5 K) in the absence of magnetic field, the magnetic

moments are frozen along an easy axis of the particles, which will be random, thus, the total magnetization is zero in the system. Then a weak magnetic field is applied and the magnetization is measured with increasing the temperature to room temperature, this process is called zero-field cooling (ZFC). In the field cooling (FC) measurement, the process is repeated, but the magnetic field is already applied during the cooling of the sample. Then the sample is warmed up again to reach room temperature under the same magnetic field. As shown in Figure 2.4, in the ZFC curve, the magnetization first increases because the moments of magnetic nanoparticles are gradually unblocked and align along the applied magnetic field. Then the magnetiztaion decreases due to the thermal aggitation. The temperature at the maximum point is defined as the blocking temperature.[9] The blocking temperature is also size dependent, it increases with the mean size of the nanoparticles.[10,11]

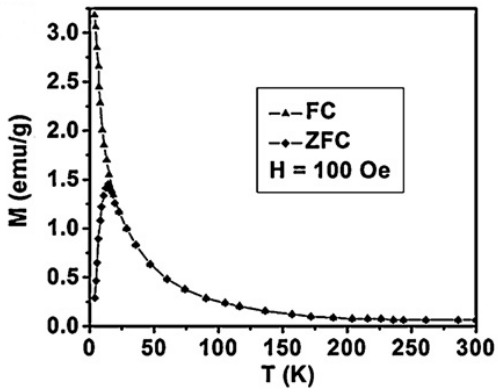

Figure 2.4 Temperature dependence of magnetization of Co nanoparticles of 3 nm in diameter, measured under ZFC and FC process, respectively. Reprinted from reference.[9]

As can be seen in Figure 2.2, superparamagnetic NPs are magnetized in an external magnetic field and reach their saturation magnetization rapidly. However, they exhibit no residual magnetization when the applied magnetic field is removed. This makes superparamagnetic NPs especially promising for biological applications.[12,13] On one hand, superparamagnetic NPs exhibit a strong and rapid response to an external magnetic field, and on the other hand, they do not agglomerate in the body after removal of the applied magnetic field. Hence there is much less concern about blood blockage and thrombosis.[14]

2.4 Synthesis of Magnetic Nanoparticles with Small Molecular Surfactants

Numerous studies about the synthesis of superparamagnetic nanoparticles have been reported either by the decomposition or reduction of metal precursor in aqueous or organic solvent.[15,16,25–28,17–24] However, well-defined nanoparticles with narrow size distribution are generally obtained by decomposition of metal precursor at high temperature.[15–23] This process can be divided into two steps: the organometallic precursor decomposes at high temperature to form nucleation nanocrystals, followed by the growth of the nuclei. Because of the large surface-to-volume ratio, the surface effect becomes very significant. Thus, surfactants are essential to stabilize and disperse magnetic nanoparticles in solvent during the synthesis procedure. Hydrophobic molecules like oleic acid (OA), oleylamine and trioctylphosphine oxide (TOPO) are commonly used for the preparation of magnetic nanoparticles. The size and shape of the nanoparticles

can be controlled by many factors, including temperature, surfactant, reaction time and the concentration of the precursor. Usually, a large ratio of surfactant/precursor forms more small nuclei and results in smaller nanocrystals. The particle size can also be tuned by the chain length of the surfactant stabilizers. For example, longer chain surfactants like trioctylphosphines slow down the growth step, resulting in smaller sizes, while shorter chain surfactants like tributylphosphines promote nanoparticles growth, leading to larger sizes. Different surfactants play different roles in the growth of nanoparticles. The combination of surfactants like oleic acid and trioctylphosphine oxide can effectively control the size of nanocrystals, in which OA binds tightly to the surface of the nanocrystals and hinders the growth, while TOPO binds weaker but promotes the growth. Similarly, Bao *et al.* showed through both computational and experimental study that the surfactants oleic acid (OA), trioctylphosphine oxide (TOPO) and dioctylamine (DOA) affected the nucleation and growth of Co NPs differently.[19] Three different growth pathways were formulated by varying the surfactant species. The combination of OA and TOPO leads to single crystalline nanoparticles through a diffusional growth pathway; however, the combination of OA and DOA results in multiple-grained nanoparticles via an aggregation growth process, and Ostwald ripening appears only in the presence of TOPO.[19] The Ostwald ripening process occurs when the nucleation happens not at the same time or the growth of nuclei do not occur simultaneously.[19,29,30] In this process, due to the high surface energy of small particles, they are re-deposited onto larger nanocrystals, which leads to a broader size distribution. If the growth rate is further increased, other shapes like disks and rods can be formed.[22,31] This effect can be further promoted by the rate of surfactants' adhesion to specific crystal planes.[32] For example, cobalt nanodisks with hcp phase were obtained by injecting cobalt carbonyl into a mixture of OA and TOPO; by fixing the concentration of OA, the diameter of the nanodisks was proportional to the concentration of TOPO (Figure 2.5).[32]

On the other hand, Hyeon's group developed a method to synthesize 2 nm spherical iron nanoparticles by using a mixture of trioctylphosphine oxide and trioctylphosphine (TOP). By adding didodecyldimethylammonium bromide (DDAB), the formed spherical nanoparticles were transferred to nanorods. The resulting iron nanorods are 2 nm in width and the length can be adjusted by varying the concentration of DDAB. The authors thought that the irreversible binding of DDAB on the center region of the growing nanoparticles is the reason for the transformation of spherical to rod-shaped iron nanoparticles.[33]

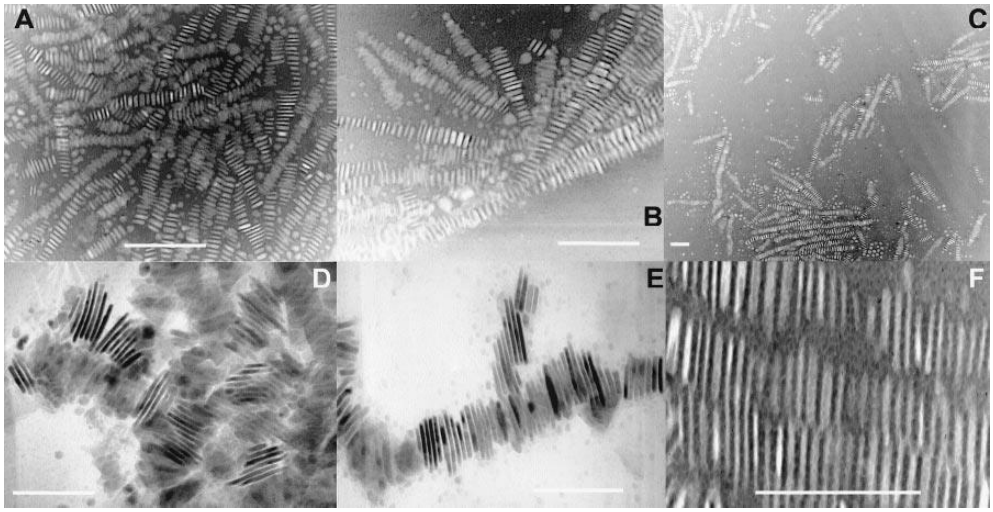

Figure 2.5 (A, B and C) Assemblies of hcp-Co rods (4 nm × 25 nm), reactants: 600 mg $Co_2(CO)_8$, 0.1 ml oleic acid and 200 mg TOPO; (D, E and F) assemblies of hcp-Co rods (4 nm × 75 nm), reactants: 600 mg $Co_2(CO)_8$ with 0.1 ml oleic acid and 300 mg TOPO. Scale bar 100 nm. Reprinted from reference.[32]

2.5 Surface Modification of Magnetic Nanoparticles

The decomposition of precursors at high temperature usually leads to magnetic nanoparticles with a narrow size distribution, and provides tunability in size and shape. However, these magnetic nanoparticles are normally stabilized by hydrophobic ligands, like oleic acid (OA) and/or oleylamine, which render the particles hydrophobic.[34,35] As a consequence, their biological applications, which require dispersion in hydrophilic or aqueous medium, are limited.[36,37] Thus, there is a great significance in the surface modification of hydrophobic nanoparticles. There are three general methods to modify the surface of nanoparticles: ligand exchange, ligand modification and additional layer coating (Figure 2.6).

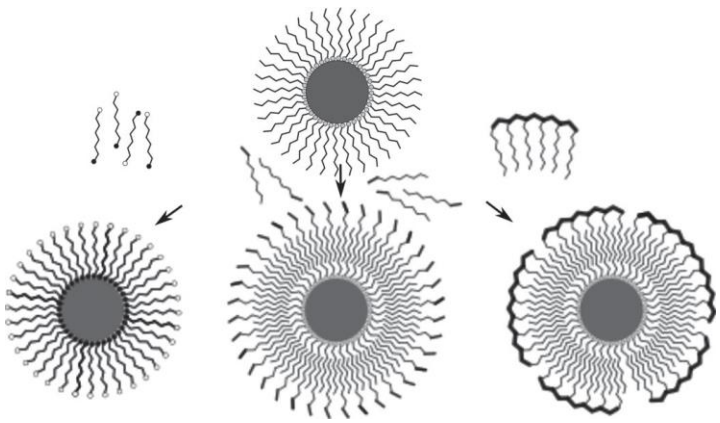

Figure 2.6 Illustration of surface modification through ligand exchange (left) and additional layer coating (middle: small molecules; right: polymers). Reprinted from reference.[38]

2.5.1 Ligand modification

Due to the hydrophilic hydroxyl groups and hydrophobic cavities which can interact with hydrophobic molecules to form a complex, cyclodextrins were used to transfer oleic acid-coated iron oxide from hydrophobic solvent into aqueous medium by forming a complex of α-cyclodextrin (α-CD) and oleic

acid.[39] Cai *et al.*, Herranz *et al,* and Wang *et al.* transferred oleic acid-stabilized iron oxide into water by oxidizing oleic acid into azelaic acid ($HOOC(CH_2)_7COOH$) (Figure 2.7).[40–42]

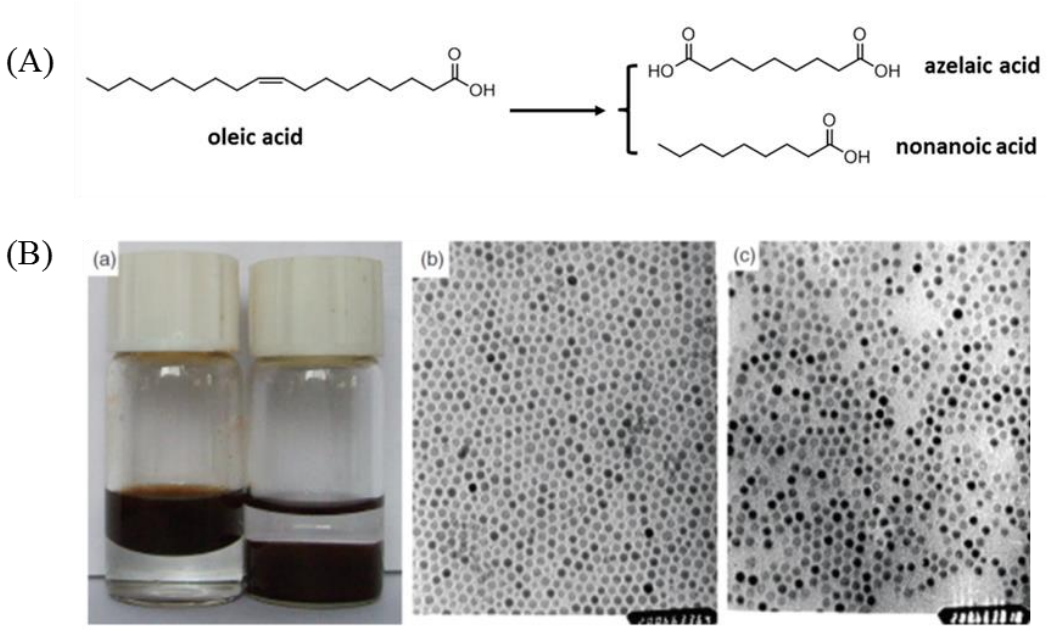

Figure 2.7 (A) Illustration of the oxidation reaction of oleic acid, reprinted from reference.[41] (B): (a) Photographs of iron oxide nanoparticles before (left) and after (right) phase transfer from hexane into water; (b,c) TEM images before (b) and after (c) phase transfer. Reprinted from reference.[42]

The ligand modification method allows for efficient transfer of hydrophobic nanoparticles into an aqueous medium, however, it is only applicable to certain systems and the oxidation of the oleic acid ligand can also cause the oxidation of some magnetic nanoparticles.

2.5.2 Additional layer coating

Additional layer coating denotes the adsorption of amphiphilic molecules or polymers (in most cases) onto the surface of hydrophic nanoparticles through hydrophobic interaction. The advantages of this method are that it is independent of the nanoparticle materials, and the chemical and physical properties of the coated nanoparticles are unaltered. Poly(maleic anhydride) copolymers are commonly used as amphiphilic polymers to transfer hydrophobic nanoparticles into water.[43–46] Such copolymers are synthesized by copolymerization of maleic anhydride with olefins, and many of them are commercially available and cheap.[45] For example, Corato *et al.* developed a strategy to transfer spherical γ-Fe_2O_3 NPs and heterodimeric FePt-Fe_xO_y NPs into water through hydrophobic interaction between amphiphilic poly(maleic anhydride-alt-1-octadecene) and hydrophobic ligands oleic acid and oleylamine.[45] During this process, poly(maleic anhydride-alt-1-octadecene) and nanoparticles were mixed in chloroform. After the slow evaporation of the solvent, a cross-linker molecule, bis(hexamethylene)triamine, in chloroform was added. A thin film was obtained after evaporation of chloroform, which can be dispersed in sodium borate buffer through sonication (Figure 2.8).

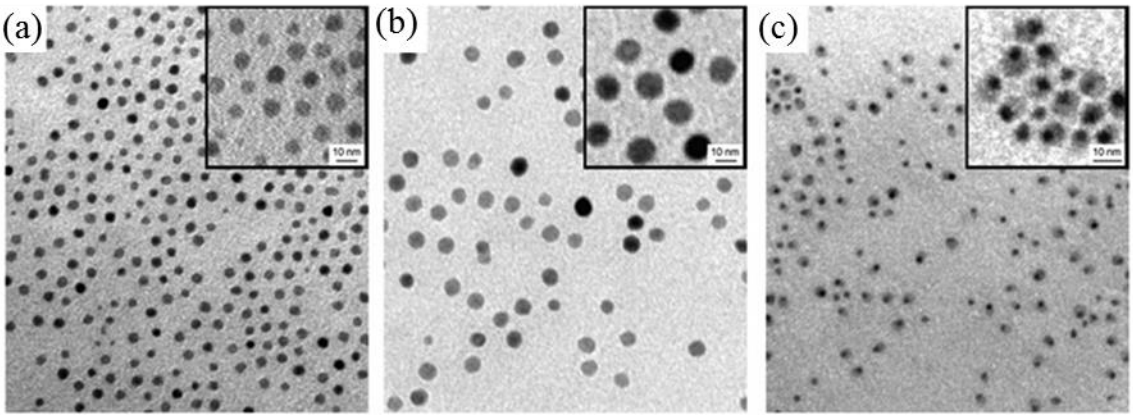

Figure 2.8 TEM images of poly (maleic anhydride-alt-1-octadecene)-coated nanoparticles: spherical γ-Fe_2O_3 NPs of 8.2 nm in diameter (a) and 12.9 in diameter (b); FePt-Fe_xO_y heterodimers of 8.7 nm in length (c). Reprinted from reference.[45]

Amphiphilic polymers based on a poly(maleic anhydride) backbone provide a lot of advantages for phase-transfer and functionalization of hydrophobic magnetic nanoparticles: firstly, the maleic anhydride moieties can react with amine end-functional organic molecules with high yield; secondly, no additional molecules for coupling are needed; thirdly, functional molecules (e.g., amino-terminated polyethylene glycol (PEG)) can be incorporated to the amphiphilic polymers to functionalize magnetic nanoparticles. Parak's group successfully transferred magnetic Fe_2O_3, $CoPt_3$ and Fe_3O_4 nanoparticles into water by using an amphiphilic polymer based on a poly(maleic anhydride) backbone.[43,46] Incorporation of functionality (e.g., PEG, biotin and galactose) into polymer (isobutylene-alt-maleic anhydride) shell around magnetic nanoparticles can reduce nonspecific adhesion (PEG) and introduce specific binding sites (biotin and galactose).[46] Other amphiphilic polymers to coat nanoparticles are polyethylene glycol-based polymers.[47–49] Yu *et al.* developed a highly efficient method to phase transfer hydrophobic iron oxide nanocrystals into water.[49] As shown in Figure 2.9A, the as-prepared iron oxide nanocrystals were well-dispersed in aqueous medium and could be conjugated with biomolecules. The water dispersion of the iron oxide nanocrystals showed negligible cytotoxicity to human dermal fibroblast cells and breast cancer cells, indicating their potential biomedical applications. Wang's group reported a general surface modification strategy to transfer hydrophobic Fe_3O_4 nanocrystals into water by encapsulating nanoparticles into carboxylated phospholipids and polymer micelles. After encapsulation, the nanoparticles maintained their original properties, size and shape (as shown in Figure 2.9B). Due to the carboxylic and PEG groups, the modified nanoparticles are biocompatible and bioconjugatable with antibodies for bioimaging, which has a potential application in nanomedicine and nanobiotechnology.[47]

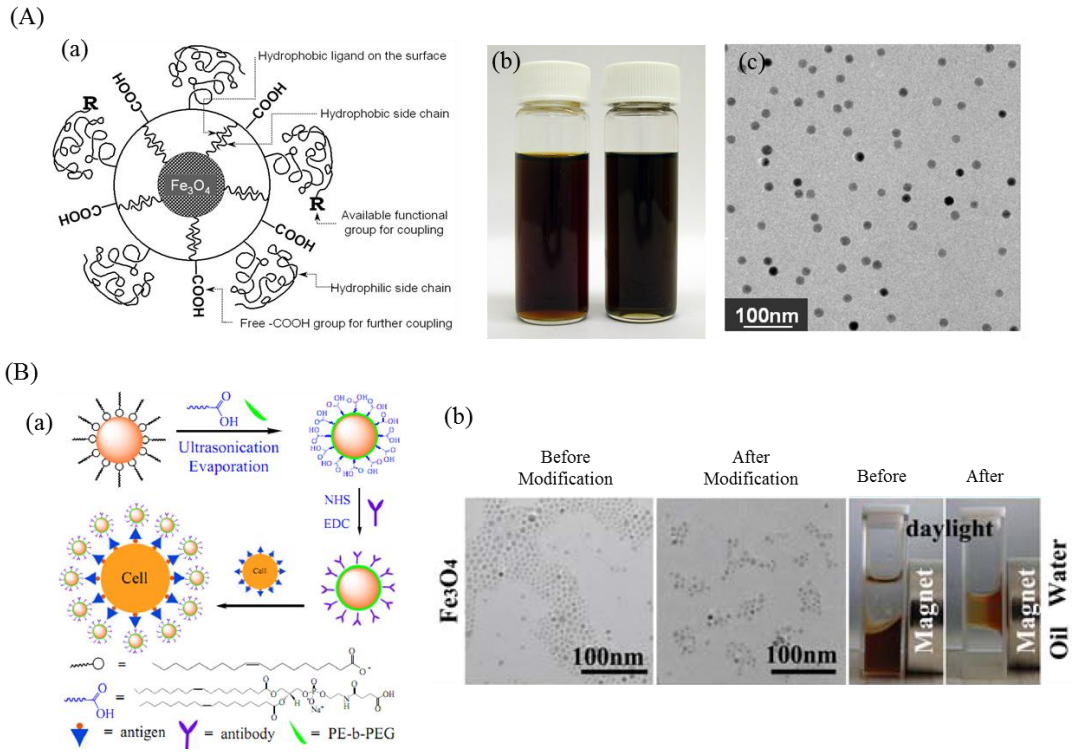

Figure 2.9 (A): (a) Illustration of the structure of water-dispersed iron oxide nanoparticles; (b) photographs of iron oxide nanocrystals dispersion in chloroform (left) and water (right); (c) cryo-TEM image of iron oxide nanocrystals in water. Reprinted from reference.[49] (B): (a) Illustration of surface modification of NPs and their bioconjugation to HepG2 living cancer cells; (b) TEM images and photographs of various inorganic nanoparticles before and after encapsulation. Reprinted from reference.[47]

In general, the large number of contact points between surfactants and the amphiphilic polymers and their hydrophobic interaction prevent the desorption of the polymers from the surface of nanoparticles, thus the encapsulated nanoparticles are stable in aqueous environment.

2.5.3 Ligand exchange

The surfactants bound to the surface of nanoparticles not only control the growth of the nanoparticles during the synthesis, but also protect nanoparticles from aggregation. The stabilization of nanoparticles is determined by the balance between attractive interaction—van der Waals, hydrophobic interaction and dipole-dipole interaction (magnetic nanoparticles) and repulsive interaction—steric repulsion and electrostatic repulsion. If the repulsive interaction dominates, nanoparticles are stable; otherwise, nanoparticles tend to aggregate. Normally, the surfactants are bound to the surface of nanoparticles through a coordinative bond. In details, the O and N atoms in functional groups (-COOH, -PO, and $-NH_2$) of surfactants donate the lone-pair electrons to the empty d-orbits of metal atoms.[19] This bond is generally not strong, and surfactants and nanoparticles undergo a dynamic binding and unbinding process. That means, the surfactants can be removed by access washing, which, on the one hand, leads to aggregated nanoparticles, and on the other hand, new ligands can rebind to the surface of nanoparticles to stabilize them. The latter is called ligand exchange process, which is carried out with the incoming ligands having

stronger binding to the nanoparticles surfaces and/or a higher concentration than the original surfactants, ensuring a quick and efficient replacement.

Dopamine (DPA) has a high affinity to the Fe_3O_4 surface and has been used as a ligand to transfer hydrophobic nanocrystals into water.[50,51] Sun's group reported that a DPA-PEG based ligand can replace oleylamine and keep Fe_3O_4 nanoparticles stable in water or in a physiological environment (Figure 2.10A). Moreover, the PEG coated-nanoparticles showed only a very low level of uptake in macrophage cells, which means that the innate immune system has low effect on these nanoparticles, as shown in Figure 2.10A (c). The multiple carboxylic groups on the particles surface render them potentially applicable in drug delivery, bio-imaging and bio-detection.[50] Hydroxamic acid shows stronger binding than phosphonic acid or carboxylic acid to the iron oxide surface.[52,53] Peng's group synthesized a ligand containing polyethylene glycol terminated organic dendrons and a hydroxamic acid group to replace hydrophobic ligands, forming so-called dendron-nanocrystals. These dendron-nanocrystals are stable against acid etching and thermal treatment.[53]

Silanes are also used to replace original small molecular ligands. For example, Palma *et al.* developed a ligand exchange procedure by using silanes with various end groups to functionalize ferrite magnetic nanoparticles with carboxylic acid and amino groups, as well as poly(ethylene glycol). The water dispersible NPs were stable against mild acid and alkaline solution, enabling their biological applications.[54]

Other small molecules can also be used for ligand exchange. For example, Salgueiriño-Maceira *et al.* transferred oleic acid/oleylamine-capped Fe_xPt_{1-x} nanoparticles from hexane into water by using a phase transfer agent tetramethylammonium hydroxide (TMAOH). The TMAOH ligand replaced the original ligands and formed an electrostatic double layer, which ensured a highly stable water dispersion even at high concentration.[55] Wang *et al.* reported a facile and efficient ligand exchange process by using small-molecule ligands such as 4-gallic acid (GAL), hydroxybenzoic acid (HBA) and 3-(4-hydroxyphenyl)propionic acid (HPP) to replace the original ligands on the surface of FePt and FeO_x nanoparticles, followed by dispersing them into various polar and protic solvents without aggregation. These dispersions were stable even for years.[56] Magnetic resonance imaging (MRI) is a powerful method in medical applications. MRI contrast agents are used to improve the visibility of the inner body structures. There are two commercial types of MRI contrast agents: T_1 MRI contrast agent (a positive contrast agent, which provides brighter images) and T_2 contrast agent (a negative contrast agent, which provides darker images).[57] Hou's group developed a rapid ligand exchange method by using protocatechuic acid as ligand to transfer Fe_3O_4 nanoparticles into water. After ligand exchange, the NPs were stable in water and exhibited excellent biocompatibility. MRI experiments demonstrated that these NPs were excellent T_1 and T_2 contrast agents and magnetic heating agents under magnetic fields. Moreover, magnetic hyperthermia and multimodality imaging showed that the Fe_3O_4 NPs are promising for cancer diagnosis and therapy.[58]

The most common way to stabilize nanoparticles against aggregation is coating a polymer bush on the surface via ligand exchange, which is the so-called "grafting-to" strategy. Förster reported a ligand

exchange procedure to control the stabilization of nanoparticles.[59] By careful design of the coordinating groups for polymer ligand exchange, a high grafting density was reached. By changing the molecular weight of the polymers, the inter-particles distance can be tuned. The use of commercially available polymers for ligand exchange can broaden the application of the method.[59] Yin developed a general ligand exchange approach for transferring hydrophobic nanoparticles into water (Figure 2.10B). Polyelectrolytes like poly(allylamine) and poly(acrylic acid), providing strong binding groups and multiple anchoring points, ensure an effective ligand exchange process, which enabled the nanocrystals to be stable for months without aggregation.[60] Poly(ethylene glycol), a well-known biocompatible polymer, has been widely studied.[61] PEG-based ligands have been used for ligand exchange with iron oxide and FePt nanocrystals.[51,62,63]

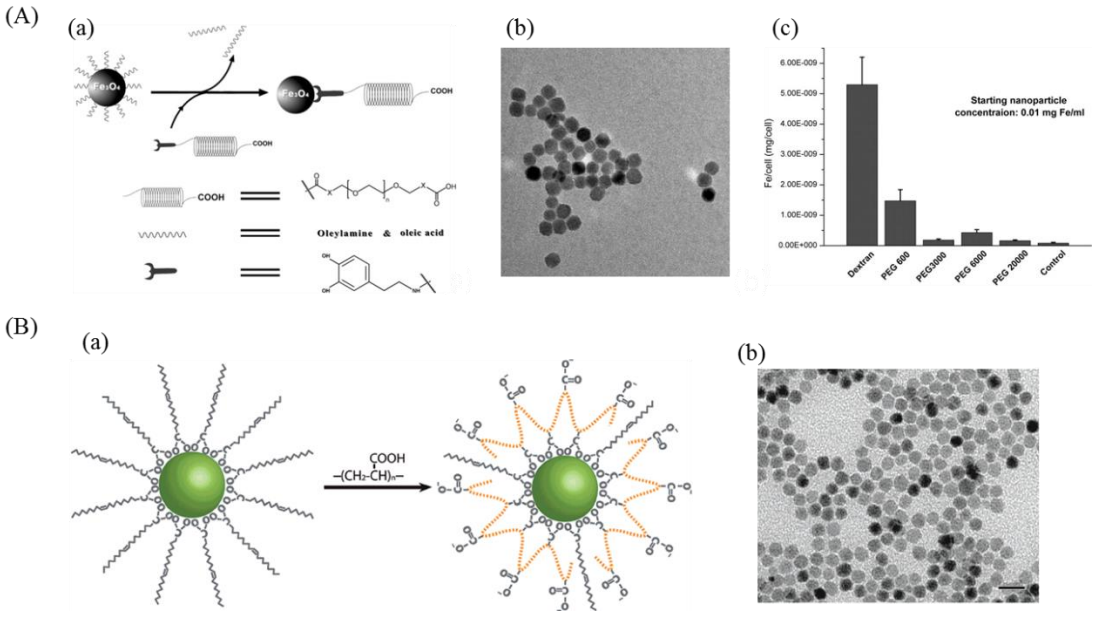

Figure 2.10 (A) (a) Illustration of surface modification of Fe_3O_4 nanoparticles; (b) TEM images of the Fe_3O_4 nanoparticles after ligand exchange with DPA-PEG6000; (c) the study of uptake of DPA-PEG coated Fe_3O_4 nanoparticles in macrophage, the Fe concentration shown here is 0.01 mg Fe/mL. Reprinted from reference.[50] (B) (a) Illustration of ligand exchange process by using poly(acrylic acid) as ligand; (b) TEM image of γ-Fe_2O_3 nanocrystals in aqueous dispersion. Scale bar is 20 nm. Reprinted from reference.[60]

Most ligand exchange processes are irreversible, only a few surface modification strategies are reversible.[64] Dong *et al*. used nitrosonium tetrafluoroborate ($NOBF_4$) to replace the original hydrophobic ligands, rendering various nanocrystals (metals, metal oxide and semiconductors) hydrophilic with no change in size and shape (as shown in Figure 2.11). This procedure can be conducted both in one phase or two phase transfer. More importantly, the ligand exchange process was reversible, the hydrophilic nanocrystals can be further modified with original or other functional molecules via a secondary ligand exchange process (Figure 2.11).[65]

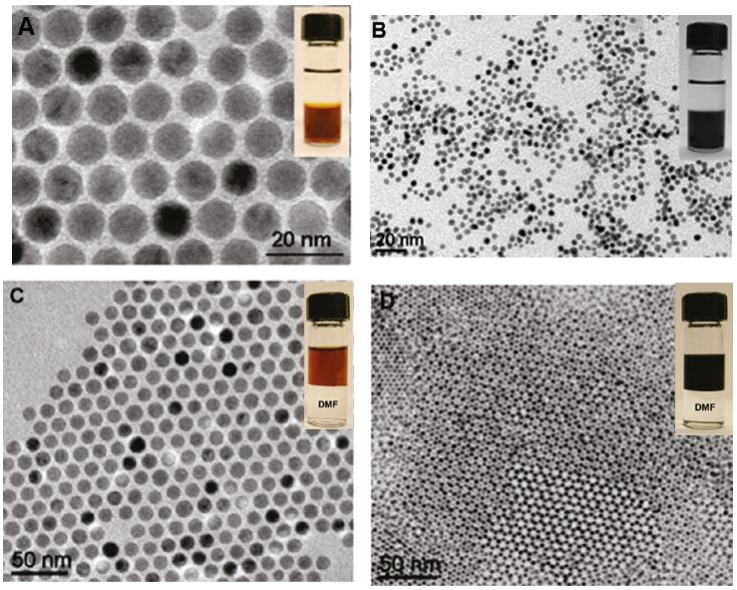

Figure 2.11 (A-B) TEM images of nanocrystals after the modification by BF_4^- in DMF: Fe_3O_4 nanoparticles (A) and FePt nanoparticles (B); (C-D) TEM images of the secondary ligand exchange process of BF_4^- modified nanocrystals: Fe_3O_4 (C) and FePt (D). The insets are photographs of the nanocrystals after first and secondary modification with hexane as the upper layer and DMF as lower layer. Reprinted from reference.[65]

In order to quantify a ligand exchange process, recently, Mefford *et al*. utilized a radiotracer technique to track the exchange process. ^{14}C-oleic acid was radiolabeled for the synthesis of hydrophobic iron oxide nanoparticles. Hydrophilic ligands with functional groups including catechols, carboxylic acids, thiols, sulfonates, phosphonates, and silanes were used to exchange the radiolabeled ^{14}C-oleic acid. The results showed that the ligand exchange process cannot go completion even with strongly binding anchor groups like catechols. Residual oleic acid remained on the surface of the nanoparticles. The study also showed that multi-dentate ligands binding more tightly than mono-dentate ligands, which provided information for designing suitable ligands for the ligand exchange technique.[66,67]

2.6 Assembly of Magnetic Nanoparticles

Magnetic nanomaterials, due to their interesting fundamental magnetic properties, have many potential applications.[68–72] High-density information storage is one of the most promising applications for magnetic nanoparticles. Magnetic devices made from these nanoparticles would have a data storage density of several terabits cm^{-2}, which is even higher than the hard drives in the most advanced computer (about 35 gigabits cm^{-2}). This requires a stable magnetization of highly ordered superstructures.[73,74] In this case, a deep understanding of the assembly of magnetic nanoparticles into well-ordered one-, two- and three-dimensional sturctures is essential. The assembly of magnetic nanocrystals has been widely studied; some general methods include drying of the NPs dispersions on substrates either by drop-casting or spin-coating, assembly at liquid-air interface (e.g. Langmuir-Schaefer or Langmuir-Blodgett), as well as magnetic-field-induced assembly.

2.6.1 Drying on substrates

For the drop-casting method, NPs are dispersed in a solvent, which is also called carrier solvent, and dropped on a substrate (e.g., silicon wafer, TEM grid, or highly oriented pyrolytic graphite (HOPG)) with subsequent evaporation of the solvent. During this process, the slow evaporation of the solvent is a very important factor for the self-assembly into well-ordered structures. Thus, the use of a carrier solvent with high boiling-point (e.g. dichlorobenzene, *n*-octane, toluene) or evaporation under a relatively high degree of solvent saturation atmosphere is needed. Sun *et al.* synthesized monodisperse iron-platinum (FePt) nanoparticles based on the reduction of platinum acetylacetonate and decomposition of iron pentacarbonyl by using oleic acid and oleylamine as stabilizers. These nanoparticles self-assembled into three-dimensional superlattices by dropping a FePt suspension (hexane/octane, v/v 1/1) onto a SiO-coated copper grid, followed by slow evaporation of the solvent. Thermal annealing converted the nanoparticles structure from face-centered cubic (fcc) phase to long-range ordered face-centered tetragonal phase, and transferred from superparamagnetic superlattices into ferromagnetic nanocrystal assemblies, which showed a potential in future magnetic recording.[74] Weller's group produced monodisperse and highly crystalline $CoPt_3$ nanoparticles by reduction of platinum actylacetonate and thermolysis of cobalt carbonyl with 1-adamantanecarboxylic acid as surfactant. The as-prepared nearly spherical $CoPt_3$ nanocrystals were able to assemble into two- and three-dimensional structures (Figure 2.12A). An AB_5-type superlattice was obtained by mixing nanoparticles of two different sizes by slow evaporation of the carrier solvent (Figure 2.12B).[75]

Pileni's group reported the formation of cobalt nanoparticles with narrow size distribution and self-assembly into face-centered-cubic supercrystals.[76–78] The structural ordering can be controlled by changing the temperature of the substrate during the solvent evaporation process. A continuous amorphous film was formed at lower substrate temperature ($5 < T < 12$ °C) and a film with cracks was obtained at higher substrate temperature ($18 < T < 45$ °C). By lowering the evaporation rate of the solvent at higher vapor saturation, it was possible to obtain crack-free and homogeneous films. A slight change of the magnetic properties for the highly ordered nanocrystals was determined due to dipole-dipole interactions compared with disordered assemblies.[76]

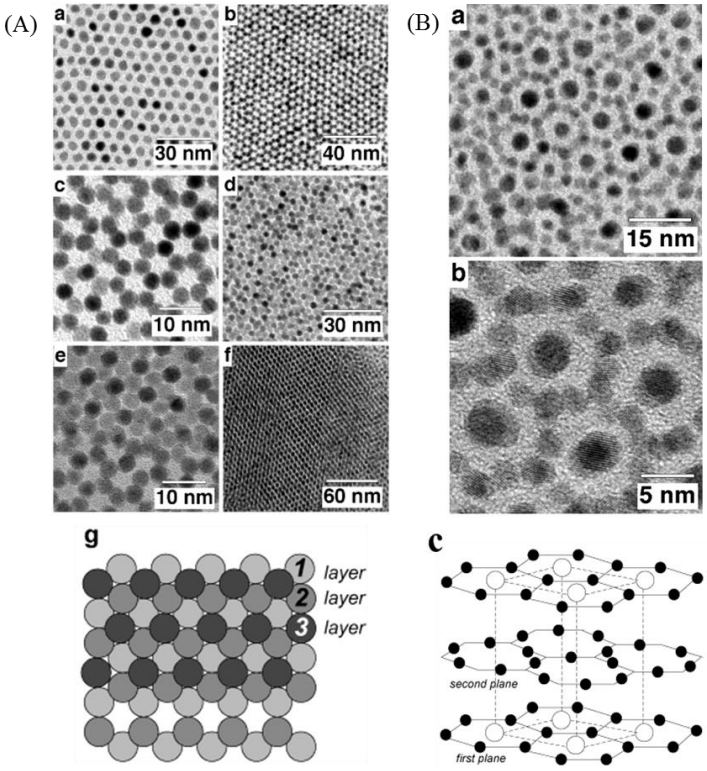

Figure 2.12 (A) TEM images of (a) monolayer of 4.8 nm $CoPt_3$ nanocrystals, (b and c) two layers of 3.6 nm and 4 nm $CoPt_3$ nanocrystals, (d) three layers of 3.6 nm $CoPt_3$ nanocrystals, (e) three layer of 4.0 nm $CoPt_3$ nanocrystals, (f) more than five layer of 4.5 nm $CoPt_3$ nanocrystals, (g) illustration of three layers of $CoPt_3$ nanocrystals; (B): (a)TEM and (b) HRTEM images of 3-D superlattices of AB_5-type of $CoPt_3$ nanocrystals formed from a mixture of 4.5 nm and 2.6 nm $CoPt_3$ nanocrystals, (c) illustration of AB_5 structure. Reprinted from reference.[75]

The drop-casting method for the self-assembly is suitable to obtain local ordered areas of nanoparticle films, but is not able to produce a large scale ordered film (> 1 cm^2). Furthermore, the process is difficult to control, which results in inhomogeneous films with cracks. These drawbacks limit the ultrahigh-density magnetic storage.

For the spin-coating technique, magnetic NPs dispersion is dropped on a substrate, and spun to spread NPs on the substrate and remove the carrier solvent rapidly. By varying the concentration of magnetic NPs, the density of NPs in the layer can be tuned at a certain speed.[79] However, the drawback of this method is that it can only be operated on a planar surface.

2.6.2 Assembly at liquid-air interface

The Langmuir-Blodgett (LB) technique is widely used to assemble films of amphiphilic materials including polymers, colloids and nanoparticles, at liquid-air interface and tranfer the films onto solid substrates.[80] Nanoparticles coated by hydrophobic molecules can also be used for LB films, therefore, a dispersion of magnetic nanoparticles can be dropped onto a liquid phase (water or less polar solvents like glycols) to form a monolayer of the nanoparticles at the liquid-air interface. Then, the monolayer can be transferred onto various substrates (e.g. TEM grid, silica wafer, HOPG, etc.). A multilayer can be formed on the substrate by multiple dipping of the substrate. When the dipping direction is vertical, it is called

Langmuir-Blodgett technique, and if the dipping is in a horizontal direction, it is called Langmuir-Schaefer technique.[81–89]

Vorobiev *et al.* combined the characterization techniques of *in-situ* X-ray reflectivity (XRR), grazing incidence small-angle X-ray scattering (GISAXS), brewster angle microscopy (BAM) and scanning electron microscopy (SEM) to investigate the self-assembly of magnetic iron oxide nanoparticles in Langmuir films formed on water surface. For this purpose, iron oxide nanoparticles with different sizes coated with oleic acid were synthesized. The results showed that 10 nm nanoparticles can form a large area of a high-ordered monolayer and in a reproducible manner, while 20 nm particles only formed three-dimensional clusters, and 15 nm particles did not form a stable film. One possible reason could be that the magnetic moment differed with the size of magnetic nanoparticles. In their study, nanoparticles with the size of 10 nm were superparamagnetic and 20 nm particles were ferromagnetic, while NPs with the size of 15 nm were a crossover between the two properties.[90] Weller's group used for the first time diethylene glycol as subphase to assemble and tranfer a large area monolayer of cobalt platinum (CoPt) nanoparticles through the Langmuir-Blodgett technique. The investigation showed that the dipping angle (around 105°), removal of the free surfactants on nanoparticles surface, and the use of diethylene glycol as the subphase are important factors to obtain a high-quality film. Characterization by scanning electron microscopy, grazing incidence X-ray scattering showed highly ordered deposited films.[91] Furthermore, direct current (DC) measurement was used to investigate the electrical properties of the deposited films. As shown in Figure 2.13b, a silicon oxide layer of 300 nm thickness was thermally grown on a silicon wafer, and was structured with two gold electrodes of 30 nm thickness by e-beam lithography. CoPt nanoparticles were then deposited on the surface of the structure. The DC measurement showed that the charge transport mechanism of the simple thermally activated transport fits the experimental data better than that of the variable range hopping method from the randomly shaped metal model.[91] Pohjalainen *et al.* and Sachan *et al.* assembled cobalt nanoparticles via Langmuir-Schaefer technique by using ethylene glycol as the subphase.[81,92] Because of the better spreading of tridodecylamine (TDA)-stabilized cobalt nanoparticles on ethylene glycol subphase than on water, Pohjalainen *et al.* investigated the formation of Langmuir layers on the ethylene glycol surface by varying the experimental conditions, including the solvent of the nanoparticles dispersion, the presence of excess TDA, and the addition of poly(styrene-*b*-ethylene oxide) (PS-*b*-PEO) in the nanoparticle dispersion.[81] The results showed that the removal of excess TDA ligand and the addition of PS-*b*-PEO are essential to obtain a homogeneous film with high coverage of nanoparticles. Magnetic measurements showed that the as-prepared films exhibited superparamagnetic properties and the saturation magnetization of the films was around 100 emu/$g_{(Co)}$, which indicated that TDA-coated cobalt nanoparticles were stable against oxidation.

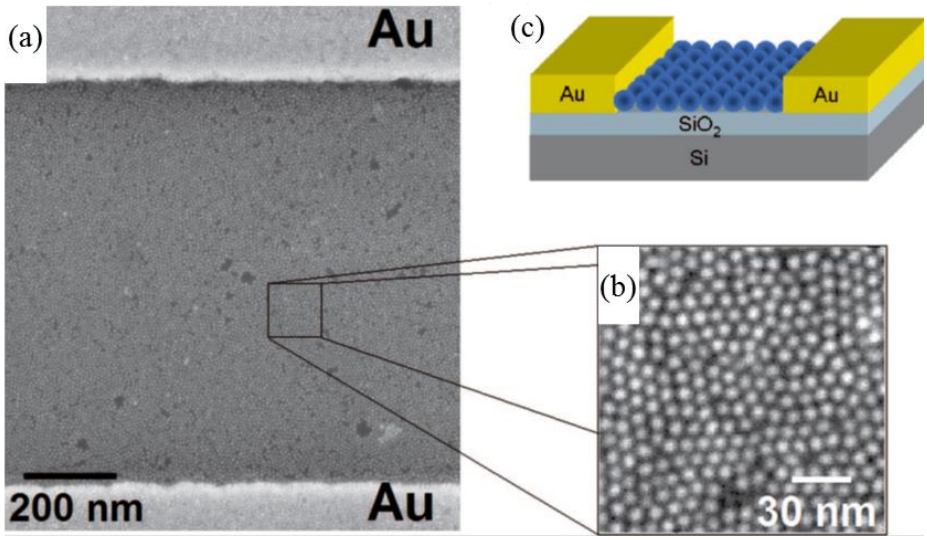

Figure 2.13 (a) Scanning electron microscopy (SEM) image of CoPt Langmuir film deposited on an electron-beam lithographically patterned gold electrodes; (b) magnified view of CoPt nanoparticles film; (c) Illustration of the device for DC measurement. Reprinted from reference.[91]

Apart from water and glycol, dimethyl sulfoxide (DMSO) and actonitrile were also used as subphases for the assembly of hydrophobic magnetic nanoparticles,[93,94] which indicates that the assembly of hydrophobic magnetic nanoparticles at liquid-air interface is a convenient and flexible technique.

2.6.3 Magnetic-field-induced assembly

Apart from the unassisted self-assembly of magnetic nanoparticles, numerous studies have been reported for the magnetic-field-induced assembly of magnetic NPs into 1-D superstructures.[95–100] The assembly of magnetic nanoparticles induced by magnetic field has the big advantage that the magnetic field can be controlled remotely and the response of the magnetic NPs to the applied magntic field is fast.[101,102] The magnetic nanoparticles tend to align in the direction of an external magnetic field, which can be applied either parallel or perpendicularly to the substrate.[103,104] The alignment is influenced by the strength of the applied magnetic field.[105,106] The magnetic-field-induced assembly can be conducted by deposition of magnetic nanoparticles dispersion on substrates or at the liquid-air interface. That the assembly behavior of magnetic nanoparticles is strongly influenced by the strength of the applied magnetic field, has been proved by Pileni's group, who immersed a highly oriented pyrolytic graphite substrate into a suspension of 8 nm cobalt nanoparticles under an external magnetic field.[105,107] Parameters including the strength of the magnetic field and the evaporation time, which influenced the assembly of cobalt nanoparticles, were investigated. A homogeneous film was obtained by increasing the evaporation time under hexane vapor instead of air. Longer stripes with narrower distance at mesoscopic scale along the applied field direction were observed at higher magnetic field, as shown in Figure 2.14A. By applying a magnetic field perpendicularly to the substrate, 3D superlattices of cobalt NPs were formed. By changing the strength of the applied magnetic field, the morphology of nanocrystal varied, as shown in Figure 2.14B. At low magnetic field of 0.27 T, well-defined cobalt nanoparticle dots assembled into homogenous hexagonal

networks. A slightly higher magnetic field (0.45 T) resulted in smaller dots and shorter distance between dots, and a phase transition from dots to worm-like structures was observed when the magnetic field was further increased up to 0.78 T.

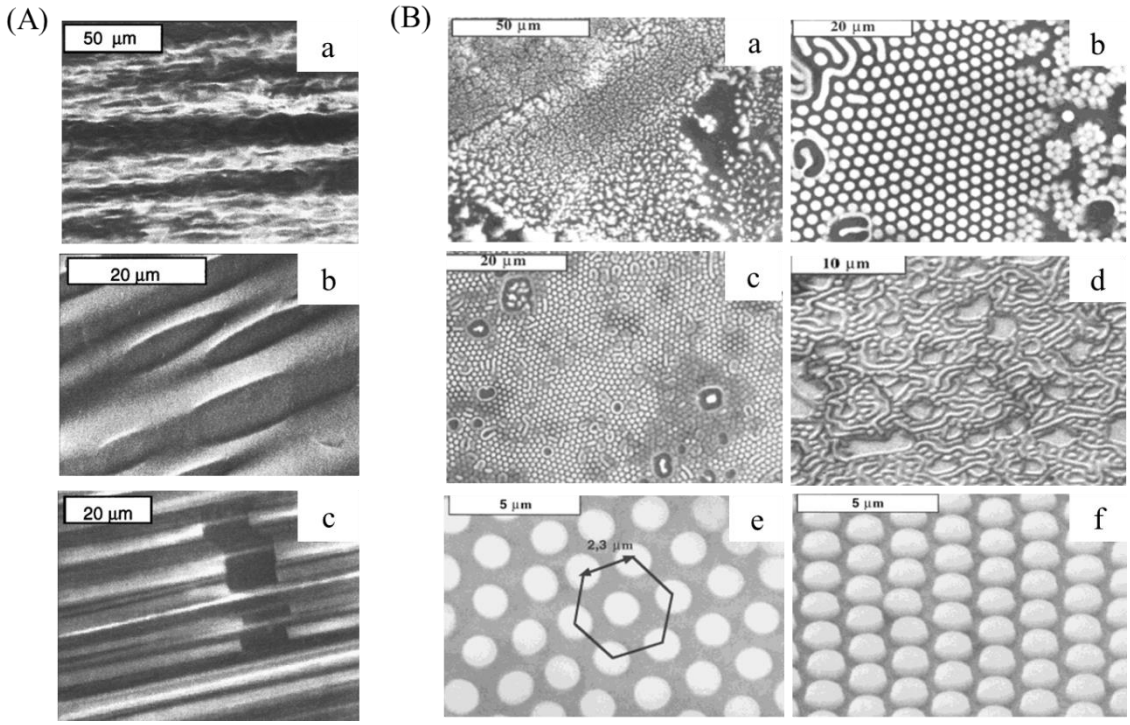

Figure 2.14 (A) SEM images of magnetic cobalt nanocrystals at various magnetic field strength: (a) 0.27 T, (b) 0.45 T, (c) 0.56 T. Reprinted from reference.[105] (B) SEM images of Co NPs assembly on HOPG substrates under an external magnetic field perpendicular to the substrates: (a) 0 T (b) 0.27 T, (c) 0.45 T, (d) 0.78 T, (e) higher magnification of the hexagonal network under 0.27 T magnetic field, (f) tilted SEM image of (e). Reprinted from reference.[107]

Park *et al.* reported that both the strength of magnetic field and the concentration of nanoparticle dispersion can affect the assembly behavior of magnetic nanoparticles. The magnetic-field-induced assembly of monodisperse 10 nm spherical cobalt nanoparticles on a Si substrate was conducted, and the magnetic field was applied either perpendicularly or parallel to the substrate.[108] Well-ordered supercrystal rods with fcc-structure were obtained when the magnetic field was applied perpendicularly to the substrate, while elongated wire-shaped superstructures with diameter of 300 nm were obtained with the field parallel to the substrate (Figure 2.15A). By changing the distance of the two magnets and the concentration of the cobalt NPs dispersion, various sizes and shapes of the superstructures were obtained. The anisotropic magnetic supercrystals have a great potential for application in high-density magnetic storage.[108]

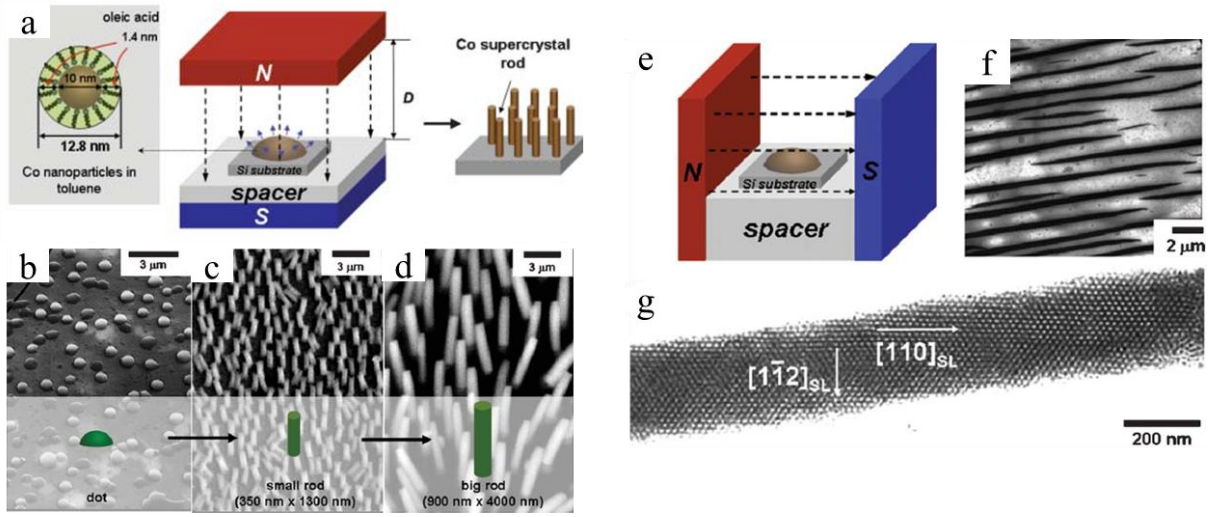

Figure 2.15 (a) Schematic illustration of the formation of supercrystal rods formation by applying a magnetic field perpendicularly to the substrate; (b) cobalt nanocrystal assembly in the absence of external magnetic field, (c) and (d) supercrystal rods obtained in the presence of magnetic field perpendicularly to the substrates by evaporation of cobalt nanocrystal suspensions of 10 mM (c) and 100 mM (d); (e–g) supercrystal wires formed by applying the magnetic field parallel to the substrate: schematic illustration of experiments (e), TEM image at low magnification (f) and TEM image high magnification (g). Reprinted from reference.[108]

2.7 Thermo-Responsive Magnetic Nanoparticles

2.7.1 Smart polymers

Stimuli-responsive polymers or smart/intelligent polymers refer to the polymers which are responsive to one or several stimuli, such as temperature, pH, light and electric/magnetic field.[109–114] Such smart polymers have been applied in many fields, including medicine and biology.[115,116] Among the above mentioned smart polymers, temperature-responsive polymers are the most studied. Some of the thermo-responsive polymers have a lower critical solution temperature (LCST), below which the polymer is homogeneously dissolved in aqueous medium, and above it, the polymer exhibits a phase separation with the solvent (Figure 2.16).[117–119] Poly(*N*-isopropylacrylamide) (PNIPAM) is one of the most widely researched polymers. Its lower critical solution temperature is around 32 °C, with a reversible change in the conformation structure between hydrophobic and hydrophilic.[113,120,121] The LCST of the polymer can shift to higher or lower temperatures by copolymerization of NIPAM with hydrophilic and hydrophobic monomer, respectively.[120,122] Other polymers which exhibit LCST behavior were also studied, including poly(*N,N*-diethylaminoethyl methacrylate) (PDEAEMA),[123] poly(*N,N*-dimethylaminoethyl methacrylate) (PDMAEMA),[124,125] poly[*N*-[2-(diethylamino)ethyl acrylamide] (PDEAEAM),[126] poly(*N,N*-diethylacrylamide) (PDEAAM),[127,128] and poly[oligo(ethylene glycol)methacrylate].[129,130]

.

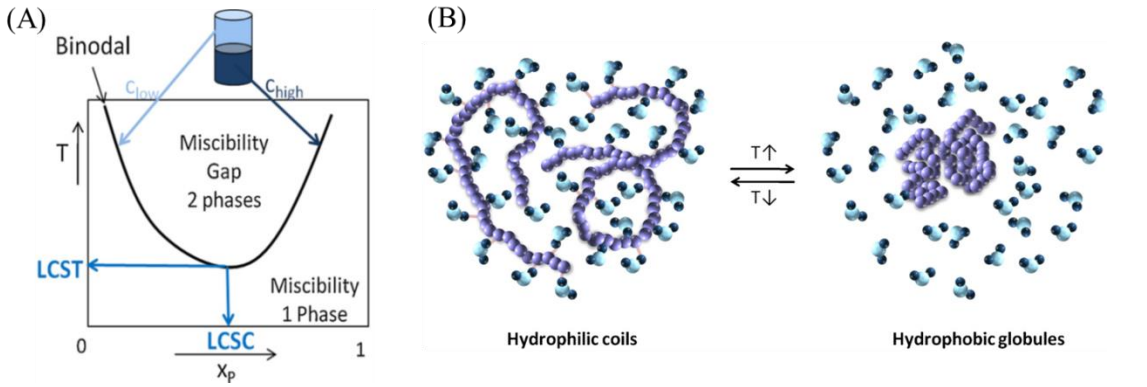

Figure 2.16 (A) Phase diagram of LCST behavior for binary polymer-solvent mixture; (B) illustration of reversible coil-to-globule transition of a thermo-responsive polymer in water. Reprinted from reference.[118]

2.7.2 Surface-initiated controlled radical polymerization (CRP)

Because thermo-responsive polymers have potential applications in many fields, it is expected that incorporation of magnetic nanoparticles into these smart polymers would endow magnetic nanoparticles with thermo-responsive property. One of the most promising techniques for their synthesis is called controlled radical polymerization (CRP), which is also known as living free radical polymerization.[131] This technique has been widely researched since the development of atom transfer radical polymerization (ATRP),[132] reversible addition-fragmentation chain transfer (RAFT) polymerization,[133] and nitroxide-mediated polymerization (NMP).[134] These polymerization techniques can be performed not only in solution but also from solid surfaces (e.g., the surfaces of nanoparticles). Figure 2.17 shows the general mechanisms of surface-initiated ATRP, surface-initiated RAFT and surface-initiated NMP.[135] Among these three surface-initiated CRP techniques, surface-initiated ATRP and surface-initiated RAFT are most commonly used, which have been widely applied to graft thermo-responsive polymers from magnetic nanoparticle surfaces with a rather high grafting density.

Schmidt's group grafted a thermo-responsive copolymer from the surface of magnetic (γ-Fe_2O_3) nanoparticles by surface-initiated ATRP (Figure 2.18). The shell consists of a copolymer of oligo(ethyleneglycol)methylethermethacrylate (OEGMA) and methoxyethylmethacrylate (MEMA), which enabled the magnetic nanoparticles to be dispersible in water. The hybrid structures showed a reversible thermoflocculation and their cloud point temperature (T_C) depended linearly on the composition of the polymer shell, thus the prediction and adjustment of the phase transfer can be achieved. Due to the intrinsic heating properties of superparamagnetic nanoparticles under the external alternating current (AC) magnetic field, the enthalpy of these nanohybrids during the phase transition process can be recorded by magnetic thermograms, indicating that these nanoparticles are promising in biological applications by tuning the cloud point temperature close to the body temperature.[136]

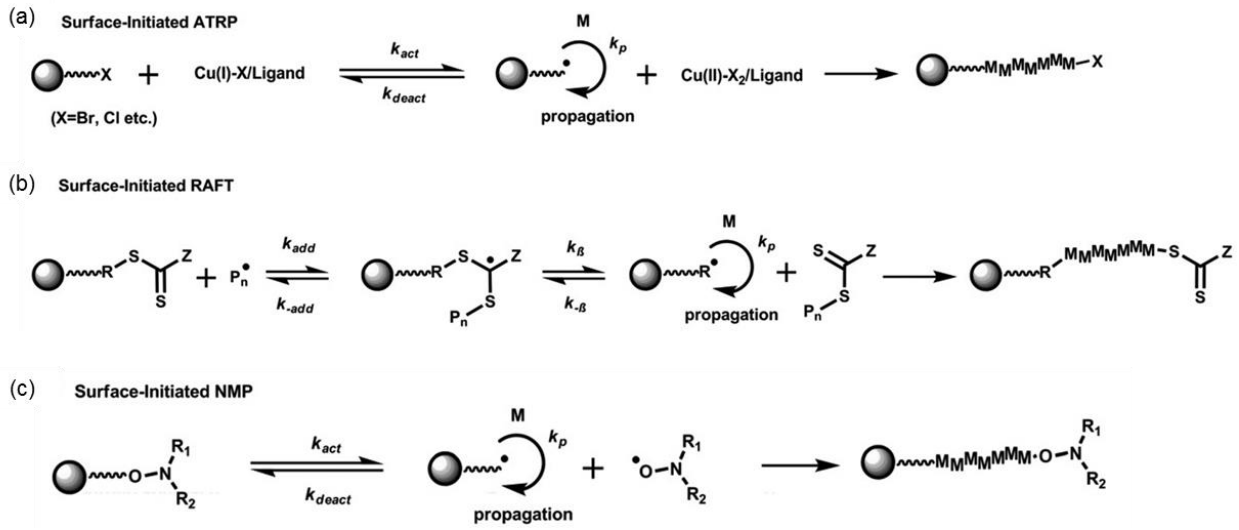

Figure 2.17 Schematic illustration of the mechanism of surface initiated CRP techniques: (a) surface-initiated ATRP; (b) surface-initiated RAFT; (c) surface-initiated NMP. Reprinted from reference.[135]

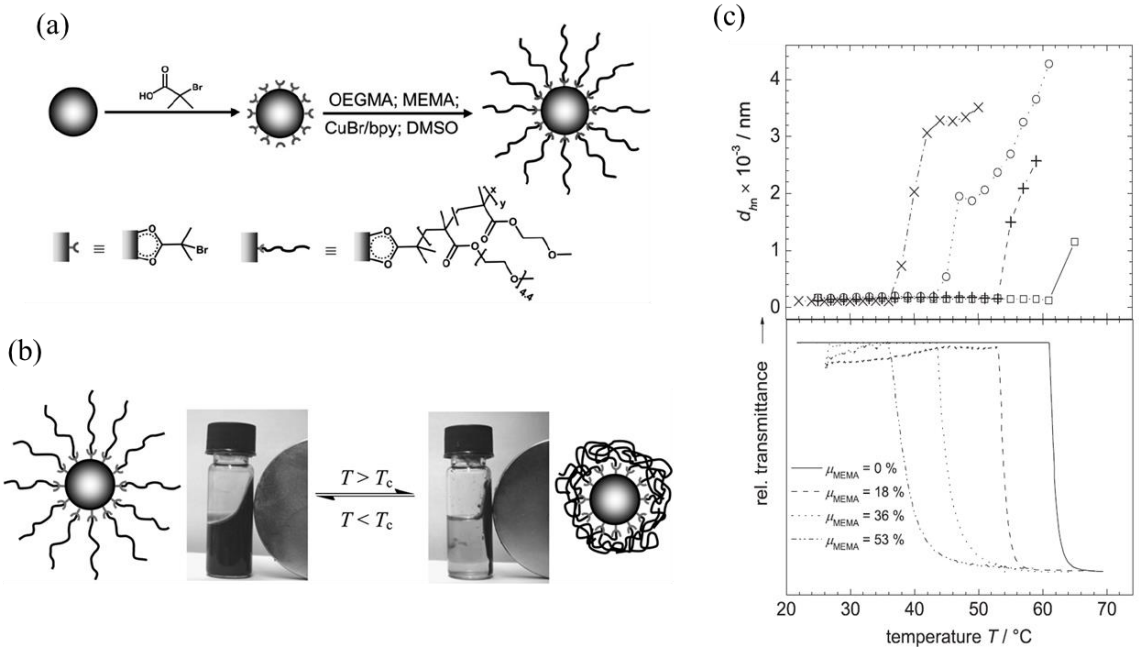

Figure 2.18 Schematic illustration of the synthesis of core /shell hybrids FeO_x@P(OEGMA-co-MEMA) through surface-initiated ATRP; (b) illustration of thermoflocculation of magnetic core-shell hybrids in water; (c) thermo-responsive behavior of core-shell hybrids with different composition: number average hydrodynamic diameter d_{hn} vs temperature T (upper graph); relative transmittance vs temperature T (lower graph). Reprinted from reference.[136]

Alem's group also grafted a copolymer of poly(co-2-(2-methoxyethoxy)ethyl methacrylate)$_x$–hydroxyl-terminated oligo(ethylene glycol) methacrylate)$_y$ (P(MOE_2MA_x–$OEGMA_y$)) from the surface of superparamagnetic Fe_3O_4 nanoparticles via surface-initiated ATRP. The LCST shifted towards higher temperature with increasing the amount of OEGMA, which contains a high hydration capacity through the ethylene oxide groups. They also showed that the composition of the polymer shell had influence on the saturation magnetization but no influence on the superparamagnetic properties of Fe_3O_4 nanoparticles.[137]

Poly(*N*-isopropylacrylamide), one of a most widely used thermo-responsive polymer, has been applied in many fields, such as drug delivery, sensors and self-healing.[138–140] Many researchers have grafted PNIPAM from the surface of magnetic nanoparticles via surface-initiated ATRP.[141–144] Reimhult's group grafted PNIPAM from the surface of superparamagnetic iron oxide nanoparticles. The core-shell hybrids showed excellent stability and reversible thermo-responsivity in water. For comparison, the grafting-to approach was also conducted, and the results from TGA measurements showed that the grafting density of surface-initiated ATRP is much higher than that of the grafting-to approach. The combination of magnetic and thermo-responsive properties can be used in integrated devices for molecular extraction and separation.[144]

Several examples have been reported for the surface-initiated RAFT technique to graft thermo-responsive polymers from the surface of magnetic nanoparticles as well. Xiao *et al.* first conducted a ligand exchange process by using a carboxyl group end-functionalized RAFT agent to replace the original oleic acid ligand on the surface of magnetic Fe_3O_4 nanoparticles, followed by the copolymerization of NIPAM and acrolein via surface-initiated RAFT method (Figure 2.19). The analysis of the grafted polymer showed that the molecular weight linearly increased with the conversion, indicating a high control over the grafted polymer via this technique. The well-defined hybrid nanoparticles exhibited temperature-triggered magnetic separation and were used for immobilization of the model protein BSA.[145]

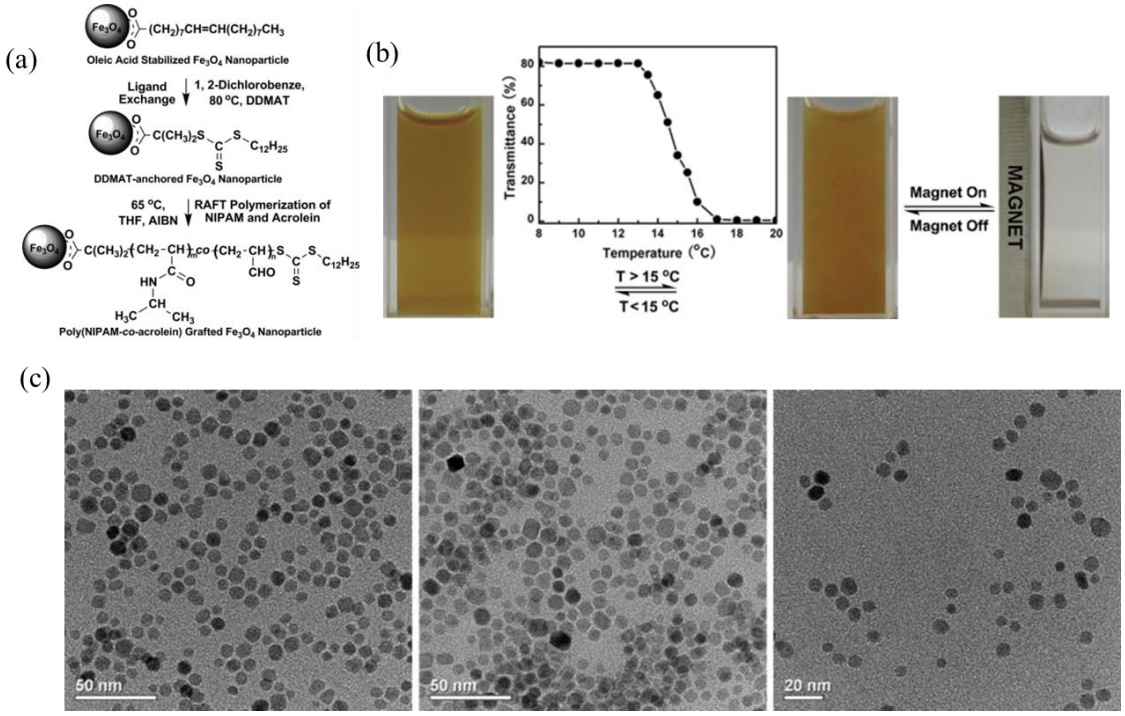

Figure 2.19 Schematic illustration of ligand exchange process and copolymerization of NIPAM and acrolein through surface-initiated RAFT on Fe_3O_4 NPs; (b) photograph of temperature and magnetic responsive behavior of poly(NIPAM-co-acrolein)-coated Fe_3O_4 nanoparticles in aqueous medium, inset shows the optical transmittance vs temperature at 800 nm at 1 wt% concentration; (c) TEM images of oleic acid-capped Fe_3O_4 nanoparticles (left), RAFT agent DDMAT capped Fe_3O_4 nanoparticles (middle) and poly(NIPAM-co-acrolein)-coated Fe_3O_4 nanoparticles (right). Reprinted from literature.[145]

Li *et al.* synthesized multi-stimuli-responsive nanohybrids Fe_3O_4@SiO_2-PNIPAM via surface-initiated RAFT polymerization. The as-prepared hybrids were easily dispersed into water and exhibited a thermo-responsive behavior. The magnetic resonance imaging (MRI) experiments showed that the combination of a magnetic core and a fluorescent-labeled shell can be used as an effective imaging agent in MRI.[146]

2.8 Synthesis of Magnetic Nanoparticles with Polymer Surfactants

The preparation of magnetic nanoparticles and polymer organic/inorganic hybrids has attracted great attention in many fields, such as drug delivery, data storage and medical applications.[73,147,148] Both small molecules and polymers have been used as surfactants to synthesize magnetic nanoparticles. However, the polymeric surfactants provide advantages over small molecules due to the stronger repulsive force to stabilize magnetic nanoparticles. Besides, the composition of the polymer can be tuned through copolymerization or post-functionalization. The development of controlled/living free radical polymerization enabled the synthesis of a wide range of polymers with precise control over the molecular weight and composition, which exhibits prominent advantage for the synthesis of magnetic nanoparticles with polymer surfactants. It is of great interest that the size, morphology and properties of magnetic nanoparticles can be tuned by variation of polymer molecular weight and composition.[149,150] In general, the approaches for the synthesis of magnetic nanoparticles with polymer surfactants are reduction of metal salts and thermolysis of metal carbonyl complexes.[151]

Thanh's group reported the synthesis of magnetic cobalt nanoparticles by reduction of cobalt chloride in the presence of alkyl thioether end-functionalized poly(methacrylic acid) (PMAADDT) in water. By varying the concentration of the polymer, the shape and size of nanoparticles could be tuned from spherical particles of 2–7.5 nm to rod-shaped structures (15×36 nm). Even larger spherical nanoparticles of 80 nm were obtained by changing the addition order of the precursor $CoCl_2$ and the reduction agent $NaBH_4$.[152] This example illustrates that the size and morphology of magnetic nanoparticles can be tuned by changing the polymer surfactant and reaction conditions. Liu *et al.* synthesized cobalt nanoparticles by using the block copolymer poly(acrylic acid)-*block*-polystyrene or PAA-PS and trioctyl phosphine as surfactants via high temperature reduction of cobalt acetate tetrahydrate. The size of the nanoparticles can be tuned by many parameters, such as the reaction time and concentration of TOP.[153]

Polymer-coated magnetic nanoparticles can also be prepared by the thermolysis of metal carbonyl complexes like $Co_2(CO)_5$ and $Fe(CO)_5$ in the presence of polymer surfactants. The size of the nanoparticles can be tuned by changing the experimental conditions, such as polymer composition, solvent and temperature. Thomas reported the preparation of magnetic cobalt nanoparticles by using (methyl methacrylate-*random*-ethyl acrylate-*random*-*N*-vinyl-pyrrolidone) (P(MMA-*r*-EA-*r*-VPy) terpolymer as surfactant in the thermolysis of $Co_2(CO)_5$ by refluxing in toluene. The prepared cobalt nanoparticles were uniform with a size around 20 nm. By changing the concentration and composition of the polymer, as well as the reaction temperature, the size could be tuned from 20 nm to 30 nm. An important finding was that

these ferromagnetic cobalt nanoparticles could be organized into 1-D chains due to dipole-dipole interaction (Figure 2.20A).[154]

An early study about the synthesis of magnetic iron nanoparticles was reported by Smith's group, who used functional vinyl polymers as surfactants through the thermal decomposition of $Fe(CO)_5$ at 150 °C. Particles with a size in the range of 5–20 nm were obtained by varying the polymer composition, solvent and ratio of polymer/Fe. Magnetic measurements showed that nanoparticles with size less than 10 nm were superparamagnetic, while NPs larger than 10 nm exhibited a hysteresis and formed 1-D assemblies at room temperature. The oxide layer on the surface of iron nanoparticles after exposure to air for 210 h was investigated by TEM and magnetometer. The results revealed that the magnetic moments were largely decreased by oxidation (Figure 2.20B).[155]

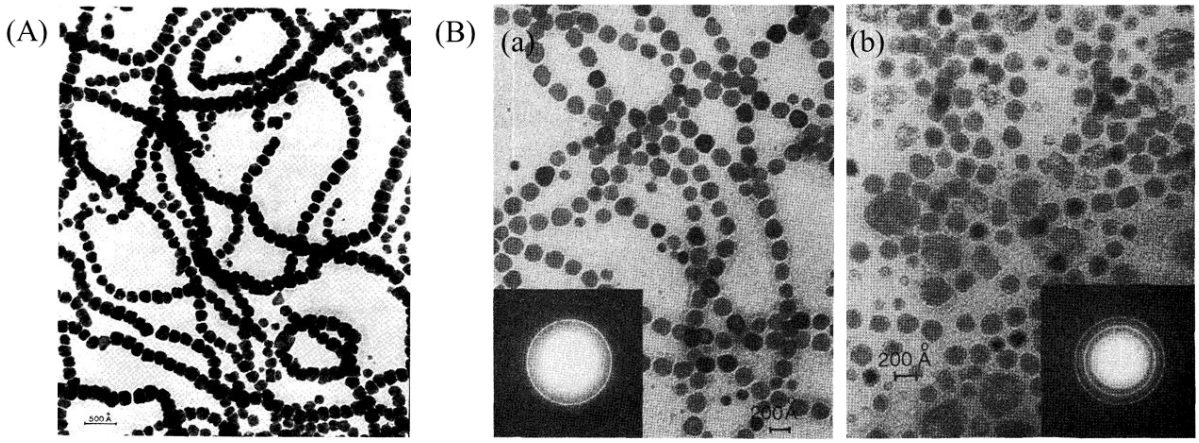

Figure 2.20 (A) TEM image of 20 nm cobalt nanoparticles. Reprinted from reference.[154] (B) TEM images of magnetic iron nanoparticles prepared in the presence of poly(4-vinylpyridine-styrene) in dichlorobenzene: (a) after preparation; (b) after exposure to air for 210 h, which caused oxidation and aggregation. Reprinted from reference.[155]

Stöver's group synthesized iron nanoparticles with ammonia and several polymers by thermolysis of iron pentacarbonyl.[156] A series of polymer surfactants with different molecular weight and composition were synthesized by ATRP. The polymer bound strongly to the iron nanoparticles to form a shell which was readily observed by TEM. The prepared iron nanoparticles exhibited different magnetic properties, from superparamagnetic to ferromagnetic at room temperature, and the saturation magnetization was dependent on the size of the particles' core.[156]

In view of the synthesis of well-defined magnetic nanoparticles by using small molecules like oleic acid, trioctylphosphine oxide, and aliphatic amines by thermal decomposition of metal precursors, Pyun's group expanded this concept by using polymers with end groups like amine, carboxylic acid, or phosphine oxide as surfactants to synthesize ferromagnetic cobalt nanoparticles.[157–159] For example, ferromagnetic cobalt nanoparticles were synthesized by using one or two of these polystyrenes with end groups including amine, phosphine oxide or carboxylic acid. These polymers were prepared by controlled radical polymerization techniques, namely, ATRP and NMP, which enabled the precise control over the molecular weight and a rather narrow molecular weight distribution. TEM results showed that cobalt nanoparticles prepared by using either amine- or phosphine oxide end-functionalized polystyrene or

combinations thereof formed well-defined 1-D chain structures, while amorphous and ill-defined nanoparticles were obtained by only using carboxylic acid end-functionalized polystyrene (Figure 2.21A). In addition, the dual stage thermolysis of $Co_2(CO)_8$ was able to obtain 1g-scale per batch.[158] The size and morphology can also be tuned by changing the reaction conditions, such as temperature and polymer molecular weight. Experiments showed that the end-functional polystyrene with molecular weight of 5000 g/mol led to uniform NPs with high stability for a long time.[157] The effect of temperature on the size of ferromagnetic cobalt nanoparticles was investigated by using carboxylic acid end-functionalized polystyrene as surfactant via a thermal decomposition of $Co_2(CO)_8$ in 1,2-dichlorobenzene. By changing the reaction temperature from 120 °C–170 °C, the size of ferromagnetic cobalt nanoparticles could be tuned in the range of 43–18 nm (Figure 2.21B and C).[159]

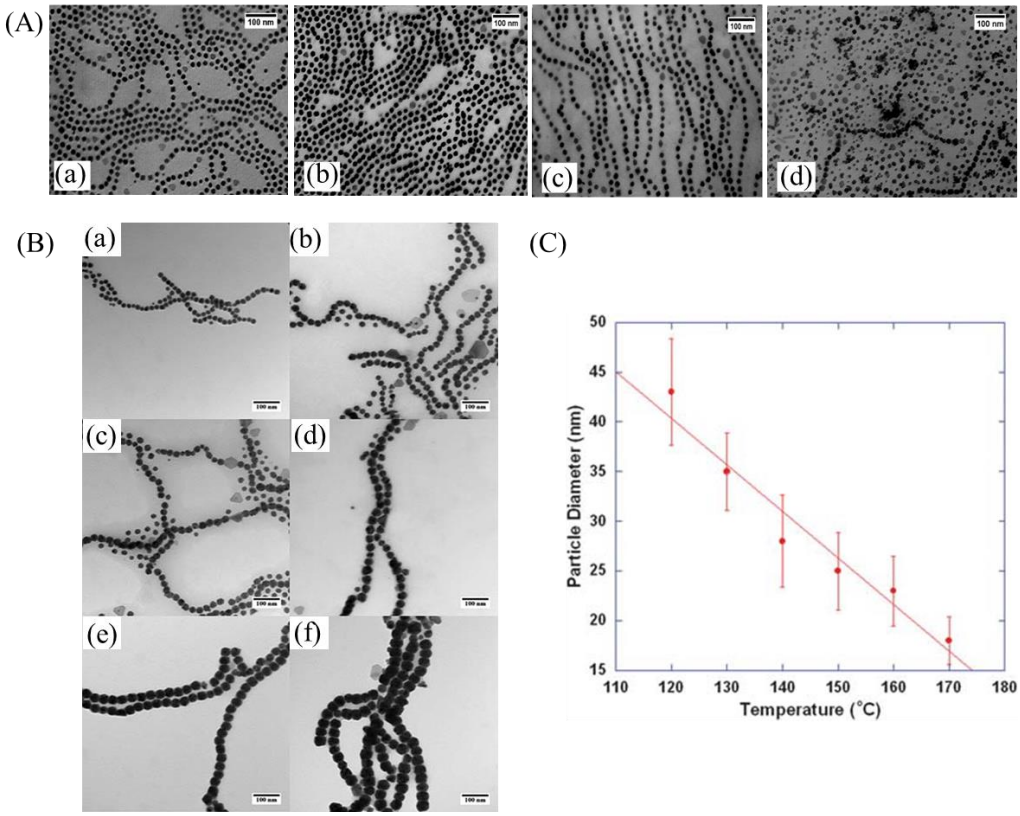

Figure 2.21 (A) TEM images of different end-functional polystyrene-coated cobalt nanoparticles obtained from the thermolysis of $Co_2(CO)_8$: (a) combination of PS-NH_2 and PS-DOPO; (b) combination of PS-NH_2 and PS-COOH; (c) only PS-NH_2; (d) only PS-COOH. Reprinted from reference.[158] (B) TEM images of polystyrene-coated cobalt nanoparticles synthesized at different temperatures: (a) 170 °C, D ~ 18 nm; (b) 160 °C, D ~ 23 nm; (c) 150 °C, D ~ 25 nm; (d) 140 °C, D ~ 28 nm; (e) 130 °C, D ~ 35 nm; (f) 120 °C, D ~ 43 nm; (C) a plot of the average size of polystyrene-coated cobalt nanoparticles versus the reaction temperature. Reprinted from reference.[159]

2.9 Cobalt Nanoparticles

Cobalt nanoparticles, one of the most promising type of metallic nanoparticles, have attracted a large interest due to their excellent magnetic, catalytic and electric properties, which have great potential in various fields, such as ferrofluids, catalysis, and magnetic resonance imaging (MRI).[160–163] Cobalt bulk material has a high saturation magnetization (≈160 emu/g) and coercivity value (≈ 800 A/m) at room

temperature.[164,165] This makes Co NPs a good choice for high-density information storage and potential application as electromagnetic wave absorber.[73,166,167]

Different crystalline structures have been synthesized: hexagonal closed-packed (hcp), face-centered cubic (fcc), and epsilon (ε).[18,32,168,169] Fcc structure is thermodynamic stable above 450 °C, while hcp structure is stable at lower temperature.[167] The epsilon structure can be transferred to fcc at high temperature annealing.[169] Puntes' group observed that Co rods of hcp structure were obtained after injection of metallic precursor in a binary surfactants mixture, and they transformed to ε-Co in the later stage of the synthesis.[32]

The synthesis of monodisperse cobalt nanoparticles is mainly conducted through the thermolysis of metallic precursor in organic solvent in the presence of surfactants.[15,16,25–28,17–24] These surfactants provide steric repulsion to protect nanoparticles from agglomeration and control the growth of nanoparticles.[18,170] Hydrophobic molecules such as oleic acid, oleylamine and trioctylphosphine oxide are often used as surfactants.[15–23] For the biological application, it is critical that magnetic nanoparticles are biocompatible, thus surface modification is often required. On the other hand, various smart polymers which are responsive to a variety of stimuli, such as temperature, pH, light and electric/magnetic field can be used.[109–114] Such smart polymers have been applied into many fields, including medicine and biology.[115,116] The combination of unique properties of cobalt nanoparticles and stimuli-responsive polymers is of great significance in future research.

2.10 References

1. de Dios, A. S. & Díaz-García, M. E. Multifunctional nanoparticles: analytical prospects. *Anal. Chim. Acta* **666,** 1–22 (2010).
2. Frey, N. A., Peng, S., Cheng, K. & Sun, S. Magnetic nanoparticles: synthesis, functionalization, and applications in bioimaging and magnetic energy storage. *Chem. Soc. Rev.* **38,** 2532 (2009).
3. Corot, C., Robert, P., Idée, J. M. & Port, M. Recent advances in iron oxide nanocrystal technology for medical imaging. *Adv. Drug Deliv. Rev.* **58,** 1471–1504 (2006).
4. Mornet, S., Vasseur, S., Grasset, F. & Duguet, E. Magnetic nanoparticle design for medical diagnosis and therapy. *Forunal Mater. Chem.* **14,** 2161–2175 (2004).
5. Jeong, U., Teng, X., Wang, Y., Yang, H. & Xia, Y. Superparamagnetic colloids: controlled synthesis and niche applications. *Adv. Mater.* **19,** 33–60 (2007).
6. Kolhatkar, A. G., Jamison, A. C., Litvinov, D., Willson, R. C. & Lee, T. R. Tuning the magnetic properties of nanoparticles. *Int. J. Mol. Sci.* **14,** 15977–16009 (2013).
7. Arruebo, M., Fernández-pacheco, R., Ibarra, M. R. & Santamaría, J. Magnetic nanoparticles for drugs delievery. *Nanotoday* **2,** 25–32 (2007).
8. Krishnan, K. M. Biomedical nanomagnetics: a spin through possibilities in imaging, diagnostics, and therapy. *IEEE Trans. Magn.* **46,** 2523–2558 (2010).
9. Alagiri, M., Muthamizhchelvan, C. & Ponnusamy, S. Structural and magnetic properties of iron, cobalt and nickel nanoparticles. *Synth. Met.* **161,** 1776–1780 (2011).

10. Chesnel, K. *et al.* Particle size effects on the magnetic behaviour of 5 to 11 nm Fe_3O_4 nanoparticles coated with oleic acid. *J. Phys. Conf. Ser.* **521,** 4–7 (2014).
11. Liu, C. & Zhang, Z. J. Size-dependent superparamagnetic properties of Mn spinel ferrite nanoparticles synthesized from reverse micelles. *Chem. Mater.* **13,** 2092–2096 (2001).
12. Ersoy, H. & Rybicki, F. J. Biochemical safety profiles of gadolinium-based extracellular contrast agents and nephrogenic systemic fibrosis. *J. Magn. Reson. Imaging* **26,** 1190–1197 (2007).
13. K Thanh, N. T., Robinson, I., Tung, L. D. & Thanh Ian Robinson, N. T. Magnetic nanoparticles for biomedical applications: synthesis, characterization and uses. *Dekker Encycl. Nanosci. Nanotechnol.* **1,** 1–10 (2007).
14. Akbarzadeh, A., Samiei, M. & Davaran, S. Magnetic nanoparticles : preparation , physical properties , and applications in biomedicine. *Nanoscale Res. Lett.* **7,** 144 (2012).
15. Tripp, S. L., Pusztay, S. V., Ribbe, A. E. & Wei, A. Self-assembly of cobalt nanoparticle rings. *J. Am. Chem. Soc.* **124,** 7914–7915 (2002).
16. Puntes, V. F., Zanchet, D., Erdonmez, C. K. & Alivisatos, A. P. Synthesis of hcp-Co nanodisks. *J. Am. Chem. Soc.* **124,** 12874–12880 (2002).
17. Dinega, D. P. & Bawendi, M. G. A solution-phase chemical approach to a new crystal structure of cobalt. *Angew. Chemie - Int. Ed.* **38,** 1788–1791 (1999).
18. Bao, Y., Beerman, M., Pakhomov, A. B. & Krishnan, K. M. Controlled crystalline structure and surface stability of cobalt nanocrystals. *J. Phys. Chem.* **109,** 7220–7222 (2005).
19. Bao, Y., An, W., Heath Turner, C. & Krishnan, K. M. The critical role of surfactants in the growth of cobalt nanoparticles. *Langmuir* **26,** 478–483 (2010).
20. Iablokov, V. *et al.* Size-controlled model Co nanoparticle catalysts for CO_2 hydrogenation: synthesis, characterization, and catalytic reactions. *Nano Lett.* **12,** 3091–6 (2012).
21. Ribeiro, R. U., Liberatori, J. W. C., Winnishofer, H., Bueno, J. M. C. & Zanchet, D. Colloidal Co nanoparticles supported on SiO_2:synthesis, characterization and catalytic properties for steam reforming of ethanol. *Appl. Catal. B Environ.* **91,** 670–678 (2009).
22. Puntes, V. F., Krishnan, K. & Alivisatos, A. Synthesis of colloidal cobalt nanoparticles with controlled size and shapes. *Top. Catal.* **19,** 145–148 (2002).
23. Puntes, V. F., Krishnan, K. M. & Alivisatos, P. Synthesis, self-assembly, and magnetic behavior of a two-dimensional superlattice of single-crystal ε-Co nanoparticles. *Appl. Phys. Lett.* **78,** 2187–2189 (2001).
24. Kobayashi, Y., Horie, M., Konno, M., Rodríguez-González, B. & Liz-Marzán, L. M. Preparation and properties of silica-coated cobalt nanoparticles. *J. Phys. Chem. B* **107,** 7420–7425 (2003).
25. Su, Y. K. *et al.* The dependence of Co nanoparticle sizes on the ratio of surfactants and the influence of different crystal sizes on magnetic properties. *Appl. Phys. A Mater. Sci. Process.* **81,** 569–572 (2005).
26. Zhao, Y. W., Zheng, R. K., Zhang, X. X. & Xiao, J. Q. A simple method to prepare uniform Co nanoparticles. *IEEE Trans. Magn.* **39,** 2764–2766 (2003).

27. Sun, S. & Murray, C. B. Synthesis of monodisperse cobalt nanocrystals and their assembly into magnetic superlattices (invited). *J. Appl. Phys.* **85,** 4325–4330 (1999).
28. Wu, N. *et al.* Interaction of fatty acid monolayers with cobalt nanoparticles. *Nano Lett.* **4,** 383–386 (2004).
29. Murray, C. B., Kagan, C. R. & Bawendi, M. G. Synthesis and characterization of monodisperse nanocrystals and close-packed nanocrystal assemblies. *Annu. Rev. Mater. Sci.* **30,** 545–610 (2000).
30. Baldan, A. Progress in Ostwald ripening theories and their applications in nickel-base super alloys. *J. Mater. Sci.* **37,** 2379–2405 (2002).
31. Peng, X. *et al.* Shape control of CdSe nanocrystals. *Nature* **404,** 59–61 (2000).
32. Victor F. Puntes, Kannan M. Krishanan, A. P. A. Colloidal nanocrystal shape and size control. *Science.* **291,** 2115–2117 (2001).
33. Park, S. J. *et al.* Synthesis and magnetic studies of uniform iron nanorods and nanospheres. *J. Am. Chem. Soc.* **122,** 8581–8582 (2000).
34. Kang, Y. & Murray, C. B. Synthesis and electrocatalytic properties of cubic Mn-Pt nanocrystals (nanocubes).*J. Am. Chem. Soc.* **132,** 7568–7569 (2010).
35. Park, J., Joo, J., Soon, G. K., Jang, Y. & Hyeon, T. Synthesis of monodisperse spherical nanocrystals. *Angew. Chemie - Int. Ed.* **46,** 4630–4660 (2007).
36. Bruchez Jr., M. Semiconductor nanocrystals as fluorescent biological labels. *Science.* **281,** 2013–2016 (1998).
37. Medintz, I. L., Uyeda, H. T., Goldman, E. R. & Mattoussi, H. Quantum dot bioconjugates for imaging, labelling and sensing. *Nat. Mater.* **4,** 435–446 (2005).
38. Sperling, R. A. & Parak, W. J. Surface modification, functionalization and bioconjugation of colloidal inorganic nanoparticles. *Philos. Trans. R. Soc. A Math. Phys. Eng. Sci.* **368,** 1333–1383 (2010).
39. Wang, Y., Wong, J. F., Teng, X., Lin, X. Z. & Yang, H. 'Pulling' nanoparticles into water: phase transfer of oleic acid stabilized monodisperse nanoparticles into aqueous solutions of α-cyclodextrin. *Nano Lett.* **3,** 1555–1559 (2003).
40. Herranz, F., Morales, M. P., Roca, A. G., Desco, M. & Ruiz-Cabello, J. A new method for the rapid synthesis of water stable superparamagnetic nanoparticles. *Chem. Eur. J.* **14,** 9126–9130 (2008).
41. Cai, J. *et al.* Large-scale, facile transfer of oleic acid-stabilized iron oxide nanoparticles to the aqueous phase for biological applications. *Langmuir* **33,** 1662–1669 (2017).
42. Wang, M., Peng, M.-L., Cheng, W., Cui, Y.-L. & Chen, C. A novel approach for transferring oleic acid capped iron oxide nanoparticles to water phase. *J. Nanosci. Nanotechnol.* **11,** 3688–3691 (2011).
43. Pellegrino, T. *et al.* Hydrophobic nanocrystals coated with an amphiphilic polymer shell: a general route to water soluble nanocrystals. *Nano Lett.* **4,** 703–707 (2004).
44. Dung, N. T. *et al.* High magnetisation, monodisperse and water-dispersible CoFe@Pt core/shell

nanoparticles. *Nanoscale* **9,** 8952–8961 (2017).

45. Di Corato, R. *et al.* Water solubilization of hydrophobic nanocrystals by means of poly(maleic anhydride-*alt*-1-octadecene). *J. Mater. Chem.* **18,** 1991 (2008).
46. Lin, C. A. J. *et al.* Design of an amphiphilic polymer for nanoparticle coating and functionalization. *Small* **4,** 334–341 (2008).
47. Deng, M., Tu, N., Bai, F. & Wang, L. Surface functionalization of hydrophobic nanocrystals with one particle per micelle for bioapplications. *Chem. Mater.* **24,** 2592–2597 (2012).
48. Chen, K. *et al.* Triblock copolymer coated iron oxide nanoparticle conjugate for tumor integrin targeting. *Biomaterials* **30,** 6912–6919 (2009).
49. Yu, W. W., Chang, E., Sayes, C. M., Drezek, R. & Colvin, V. L. Aqueous dispersion of monodisperse magnetic iron oxide nanocrystals through phase transfer. *Nanotechnology* **17,** 4483–4487 (2006).
50. Xie, J., Xu, C., Kohler, N., Hou, Y. & Sun, S. Controlled PEGylation of monodisperse Fe_3O_4 nanoparticles for reduced non-specific uptake by macrophage cells. *Adv. Mater.* **19,** 3163–3166 (2007).
51. Xie, J. *et al.* Linking hydrophilic macromolecules to monodisperse magnetite (Fe_3O_4) nanoparticles via trichloro-*s*-triazine. *Chem. Mater.* **18,** 5401–5403 (2006).
52. Folkers, J. P. *et al.* Self-assembled monolayers of long-chain hydroxamic acids on the native oxides of metals. *Langmuir* **11,** 813–824 (1995).
53. Kim, M., Chen, Y., Liu, Y. & Peng, X. Super-stable, high-quality Fe_3O_4 dendron-nanocrystals dispersible in both organic and aqueous solutions. *Adv. Mater.* **17,** 1429–1432 (2005).
54. De Palma, R. *et al.* Silane ligand exchange to make hydrophobic superparamagnetic nanoparticles water-dispersible. *Chem. Mater.* **19,** 1821–1831 (2007).
55. Salgueiriño-Maceira, V., Liz-Marzán, L. M. & Farle, M. Water-based ferrofluids from Fe_xPt_{1-x} nanoparticles synthesized in organic media. *Langmuir* **20,** 6946–6950 (2004).
56. Wang, X., Tilley, R. D. & Watkins, J. J. Simple ligand exchange reactions enabling excellent dispersibility and stability of magnetic nanoparticles in polar organic, aromatic, and protic solvents. *Langmuir* **30,** 1514–1521 (2014).
57. Xu, W. *et al.* Paramagnetic nanoparticle T1 and T2 MRI contrast agents. *Phys. Chem. Chem. Phys.* **14,** 12687 (2012).
58. Hao, R. *et al.* Developing Fe_3O_4 nanoparticles into an efficient multimodality imaging and therapeutic probe. *Nanoscale* **5,** 11954 (2013).
59. Ehlert, S. Taheri, S. M. Pirner, D. Drechsler, M. Schmidt, H. W. Foerster, S. Polymer ligand exchange to control stabilization and compatibilization of nanocrystals. *ACS Nano* **8,** 6114–6122 (2014).
60. Zhang, T., Ge, J., Hu, Y. & Yin, Y. A general approach for transferring hydrophobic nanocrystals into water. *Nano Lett.* **7,** 3203–3207 (2007).
61. Zalipsky, J. M. H. and S. Poly(ethylene glycol) chemistry and biological applications. *ACS Symp.*

Ser. **680,** 1–13 (1997).

62. Kohler, N., Fryxell, G. E. & Zhang, M. A bifunctional poly(ethylene glycol) silane immobilized on metallic oxide-based nanoparticles for conjugation with cell targeting agents. *J. Am. Chem. Soc.* **126,** 7206–7211 (2004).
63. Hong, R., Fischer, N. O., Emrick, T. & Rotello, V. M. Surface PEGylation and ligand exchange chemistry of FePt nanoparticles for biological applications. *Chem. Mater.* **17,** 4617–4621 (2005).
64. Wei, Y., Yang, J. & Ying, J. Y. Reversible phase transfer of quantum dots and metal nanoparticles. *Chem. Commun.* **46,** 3179 (2010).
65. Dong, A. *et al.* A generalized ligand-exchange strategy enabling sequential surface functionalization of colloidal nanocrystals. *J. Am. Chem. Soc.* **133,** 998–1006 (2011).
66. Davis, K. *et al.* Quantitative measurement of ligand exchange on iron oxides via radiolabeled oleic acid. *Langmuir* **30,** 10918–10925 (2014).
67. Davis, K., Cole, B., Ghelardini, M., Powell, B. A. & Mefford, O. T. Quantitative measurement of ligand exchange with small-molecule ligands on iron oxide nanoparticles via radioanalytical techniques. *Langmuir* **32,** 13716–13727 (2016).
68. Sellmyer, D. & Skomski, R. *Advanced Magnetic Nanostructures*. (Springer, 2006).
69. Dresselhaus, M.S.; Thomas, I. Alternative energy technologies. *Nature* **414,** 332–337 (2001).
70. Tseng, R. J. *et al.* Digital memory device based on tobacco mosaic virus conjugated with nanoparticles. *Nat. Nanotechnol.* **1,** 72–77 (2006).
71. Affronte, M. Molecular nanomagnets for information technologies. *J. Mater. Chem.* **19,** 1731–1737 (2009).
72. Bertero, G. A. & Sinclair, R. Structure-property correlations in Pt/Co for magneto-optic recording. *J. Magn. Magn. Mater.* **134,** 173–184 (1994).
73. Reiss, G. & Hütten, A. Magnetic nanoparticles: applications beyond data storage. *Nat. Mater.* **4,** 725–726 (2005).
74. Sun, S., Murray, C. B., Weller, D., Folks, L. & Moser, A. Monodisperse FePt nanoparticles and ferromagnetic FePt nanocrystal superlattices. *Science.* **287,** 1989–1992 (2000).
75. Shevchenko, E. V *et al.* Colloidal synthesis and self-assembly of $CoPt_3$ nanocrystals. *J. Am. Chem. Soc.* **124,** 11480–11485 (2002).
76. Lisiecki, I., Albouy, P. A. & Pileni, M. P. 'Supra' crystal: control of the ordering of self-organization of cobalt nanocrystals at the mesoscopic scale. *J. Phys. Chem. B* **108,** 20050–20055 (2004).
77. Petit, C. & Pileni, M. P. Cobalt nanosized particles organized in a 2D superlattice:synthesis, characterization, and magnetic properties. *J. Phys. Chem. B* **103,** 1805–1810 (1999).
78. Petit, C., Taleb, A. & Pileni, M. P. Self-organization of magnetic nanosized cobalt particles. *Chem. Eng. Technol.* **21,** 679–681 (1998).
79. Hong, Y. K. *et al.* Controlled two-dimensional distribution of nanoparticles by spin-coating method. *Appl. Phys. Lett.* **80,** 844–846 (2002).

80. Park, J. Y. & Advincula, R. C. Nanostructuring polymers, colloids, and nanomaterials at the air–water interface through Langmuir and Langmuir–Blodgett techniques. *Soft Matter* **7,** 9829 (2011).
81. Pohjalainen, E. *et al.* Cobalt nanoparticle langmuir-schaefer films on ethylene glycol subphase. *Langmuir* **26,** 13937–13943 (2010).
82. Guo, Q., Teng, X. & Yang, H. Fabrication of magnetic FePt patterns from Langmuir-Blodgett films of platinum-iron oxide core-shell nanoparticles. *Adv. Mater.* **16,** 1337–1341 (2004).
83. Lefebure, S. *et al.* Langmuir monolayers of monodispersed magnetic nanoparticles coated with a surfactant. *J. Phys. Chem. B* **102,** 2733–2738 (1998).
84. Chokprasombat, K., Sirisathitkul, C. & Ratphonsan, P. Liquid-air interface self-assembly: a facile method to fabricate long-range nanoparticle monolayers. *Surf. Sci.* **621,** 162–167 (2014).
85. Iakovenko, B. S. A. *et al.* One- and two-dimensional arrays of magnetic nanoparticles by the Langmuir-Blodgett Technique. *Adv. Mater.* **138,** 388–392 (1999).
86. Fried, T., Shemer, G. & Markovich, G. Ordered two-dimensional arrays of ferrite nanoparticles. *Adv. Mater.* **13,** 1158–1161 (2001).
87. Meldrum, F. C., Kotov, N. A. & Pendler, J. H. Preparation of particulate mono- and multilayers from surfactant-stabilized, nanosized magnetite crystallites. *J. Phys. Chem.* **98,** 4506–4510 (1994).
88. Bellido, E. Domingo, N. Ojea-Jiménez, I. & Ruiz-Molina, D. Structuration and integration of magnetic nanoparticles on surfaces and devices. *Small* **8,** 1465–1491 (2012).
89. Lee, D. K., Kim, Y. H., Kim, C. W., Cha, H. G. & Kang, Y. S. Vast magnetic monolayer film with surfactant-stabilized Fe_3O_4 nanoparticles using Langmuir-Blodgett technique. *J. Phys. Chem. B* **111,** 9288–9293 (2007).
90. Vorobiev, A. Khassanov, A. Ukleev, V. Snigireva, I. & Konovalov, O. Substantial difference in ordering of 10, 15, and 20 nm iron oxide nanoparticles on a water surface: *in situ* characterization by the grazing incidence X-ray scattering. *Langmuir* **31,** 11639-11648 (2015).
91. Aleksandrovic, V. *et al.* Preparation and electrical properties of cobalt-platinum nanoparticle monolayers deposited by the Langmuir-Blodgett technique. *ACS Nano* **2,** 1123–1130 (2008).
92. Sachan, M. Walrath, N. D. Majetich, S. A. Krycka, K. & Kao, C. C. Interaction effects within Langmuir layers and three-dimensional arrays of ε-Co nanoparticles. *J. Appl. Phys.* **99,** 8–11 (2006).
93. Dong, A. *et al.* Multiscale periodic assembly of striped nanocrystal superlattice. *Nano Lett.* **11,** 841–846 (2011).
94. Zhang, D. Hu, J. Kennedy, K. M. & Herman, I. P. Forming nanoparticle monolayers at liquid-air interfaces by using miscible liquids. *Langmuir* **32,** 8467–8472 (2016).
95. Ngo, A. T. & Pileni, M. P. Assemblies of ferrite nanocrystals:partial orientation of the easy magnetic axes. *J. Phys. Chem. B* 53–58 (2001).
96. Ngo, A. T. & Pileni, M. P. Cigar-shaped ferrite nanocrystals:orientation of the easy magnetic axes. *J. Appl. Phys.* **92,** 4649–4652 (2002).
97. Pileni, M. P. Nanocrystal self-assemblies:fabrication and collective properties. *J. Phys. Chem. B*

105, 3358–3371 (2001).

98. Sahoo, Y. *et al.* Field-directed self-assembly of magnetic nanoparticles. *J. Phys. Chem. B* 3380–3383 (2004).
99. Singamaneni, S. Bliznyuk, V. N. Binek, C. & Tsymbal, E. Y. Magnetic nanoparticles: recent advances in synthesis, self-assembly and applications. *J. Mater. Chem.* **21,** 16819 (2011).
100. Wiedwald, U. Spasova, M. Farle, M. Hilgendorff, M. & Giersig, M. Ferromagnetic resonance of monodisperse Co particles. *J. Vac. Sci. Technol. A Vacuum, Surfaces, Film.* **19,** 1773–1776 (2001).
101. Cho, M. H. *et al.* A magnetic switch for the control of cell death signalling in in vitro and in vivo systems. *Nat. Mater.* **11,** 1038–1043 (2012).
102. Timonen, J. V. I. Latikka, M. Leibler, L., Ras, R. H. A. & Ikkala, O. Switchable static and dynamic self-assembly of magnetic droplets on superhydrophobic surfaces. *Science.* **341,** 253–257 (2013).
103. Leo, G. *et al.* Ordering of free-standing Co nanoparticles. *Mater. Sci. Eng. C* **23,** 949–952 (2003).
104. Motte, L. Courty, A. Ngo, A. T. Lisiecki, I. & Pileni, M. P. *Self-organization of inorganic nanocrystals. Nanocrystals forming mesoscopic structures* (2006).
105. Petit, C. Legrand, J. Russier, V. & Pileni, M. P. Three dimensional arrays of cobalt nanocrystals: fabrication and magnetic properties. *J. Appl. Phys.* **91,** 1502–1508 (2002).
106. Lalatonne, Y. Richardi, J. & Pileni, M. P. Van der Waals versus dipolar forces controlling mesoscopic organizations of magnetic nanocrystals. *Nat. Mater.* **3,** 121–125 (2004).
107. Legrand, J., Ngo, A.T.,.Petit, C., & Pileni, M. P. Domain shapes and superlattices made of cobalt nanocrystals. *Adv. Mater.* **13,** 58–62 (2001).
108. Park, J.-I. Jun, Y.-W. Choi, J.-S. & Cheon, J. Highly crystalline anisotropic superstructures via magnetic field induced nanoparticle assembly. *Chem. Commun.* **1,** 5001–5003 (2007).
109. Tanaka, T. Nishio, I. Sun, S.-T. & Ueno-Nishio, S. Collapse of gels in an electric field. *Science.* **218,** 467–469 (1982).
110. Thévenot, J. Oliveira, H. Sandre, O. & Lecommandoux, S. Magnetic responsive polymer composite materials. *Chem. Soc. Rev.* **42,** 7099 (2013).
111. Shum, P. Kim, J. M. & Thompson, D. H. Phototriggering of liposomal drug delivery systems. *Adv. Drug Deliv. Rev.* **53,** 273–284 (2001).
112. Dai, S. Ravi, P. & Tam, K. C. pH-Responsive polymers: synthesis, properties and applications. *Soft Matter* **4,** 435 (2008).
113. Heskins, M. & Guillet, J. E. Solution properties of poly(*N*-isopropylacrylamide). *J. Macromol. Sci. Part A - Chem.* **2,** 1441–1455 (1968).
114. Wei, M. Gao, Y. Li, X. & Serpe, M. J. Stimuli-responsive polymers and their applications. *Polym. Chem.* **8,** 127–143 (2017).
115. Hu, J. & Liu, S. Responsive polymers for detection and sensing applications:current status and future developments. *Macromolecules* **43,** 8315–8330 (2010).
116. Pattanashetti, N. A. Heggannavar, G. B. & Kariduraganavar, M. Y. Smart biopolymers and their biomedical applications. *Procedia Manuf.* **12,** 263–279 (2017).

117. Gandhi, A. Paul, A. Sen, S. O. & Sen, K. K. Studies on thermoresponsive polymers:phase behaviour, drug delivery and biomedical applications. *Asian J. Pharm. Sci.* **10,** 99–107 (2015).
118. Weber, C. Hoogenboom, R. & Schubert, U. S. Temperature responsive bio-compatible polymers based on poly(ethylene oxide) and poly(2-oxazoline)s. *Prog. Polym. Sci.* **37,** 686–714 (2012).
119. Zhang, Q. Weber, C. Schubert, U. S. & Hoogenboom, R. Thermoresponsive polymers with lower critical solution temperature: from fundamental aspects and measuring techniques to recommended turbidimetry conditions. *Mater. Horiz.* **4,** 109–116 (2017).
120. Qin, Y. Alginate fibers: an overwiew of the production processes and applications in wound management. *Polym. Int.* **57,** 171–180 (2008).
121. Schild, H. G. Poly(*N*-isopropylacrylamine): experiment, theory and application.. *Prog. Polym. Sci.* **17,** 163–249 (1992).
122. Liu, R., Fraylich, M. & Saunders, B. R. Thermoresponsive copolymers:from fundamental studies to applications. *Colloid Polym. Sci.* **287,** 627–643 (2009).
123. Bütün, V., Armes, S. P. & Billingham, N. C. Synthesis and aqueous solution properties of near-monodisperse tertiary amine methacrylate homopolymers and diblock copolymers. *Polymer.* **42,** 5993–6008 (2001).
124. Plamper, F. A., Schmalz, A., Ballauff, M. & Müller, A. H. E. Tuning the thermoresponsiveness of weak polyelectrolytes by pH and light:lower and upper critical-solution temperature of poly(*N,N*-dimethylaminoethyl methacrylate). *J. Am. Chem. Soc.* **129,** 14538–14539 (2007).
125. Karjalainen, E. Aseyev, V. & Tenhu, H. Influence of hydrophobic anion on solution properties of PDMAEMA. *Macromolecules* **47,** 2103–2111 (2014).
126. Song, Z., Wang, K., Gao, C., Wang, S. & Zhang, W. A new thermo-, pH-, and CO_2-responsive homopolymer of poly[*N*-[2-(diethylamino)ethyl]acrylamide]:is the diethylamino group underestimated? *Macromolecules* **49,** 162–171 (2016).
127. Cao, Y. Zhu, X. X. Luo, J. & Liu, H. Effects of substitution groups on the RAFT polymerization of *N*-alkylacrylamides in the preparation of thermosensitive block copolymers. *Macromolecules* **40,** 6481–6488 (2007).
128. Idziak, I. Avoce, D. Lessard, D. Gravel, D. & Zhu, X. X. Thermosensitivity of aqueous solutions of poly(*N,N* -diethylacrylamide). *Macromolecules* **32,** 1260–1263 (1999).
129. Roth, P. J. Jochum, F. D. Forst, F. R. Zentel, R. & Theato, P. Influence of end groups on the stimulus-responsive behavior of poly[oligo(ethylene glycol) methacrylate] in water. *Macromolecules* **43,** 4638–4645 (2010).
130. Lutz, J. F. Akdemir, Ö. & Hoth, A. Point by point comparison of two thermosensitive polymers exhibiting a similar LCST: is the age of poly(NIPAM) over? *J. Am. Chem. Soc.* **128,** 13046–13047 (2006).
131. Matyjaszewski, K. & Spanswick, J. Controlled/living radical polymerization. *Mater. Today* **8,** 26–33 (2005).
132. Matyjaszewski, K. & Xia, J. Atom transfer radical polymerization. *Chem. Rev.* **101,** 2921–2990

(2001).

133. Moad, G., Rizzardo, E. & Thang, S. H. Living radical polymerization by the RAFT process. *Aust. J. Chem.* **58,** 379–410 (2005).

134. Hawker, C. J. Bosman, A. W. & Harth, E. New polymer synthesis by nitroxide mediated living radical polymerizations. *Chem. Rev.* **101,** 3661–3688 (2001).

135. Wu, L., Glebe, U. & Böker, A. Surface-initiated controlled radical polymerizations from silica nanoparticles, gold nanocrystals, and bionanoparticles. *Polym. Chem.* **6,** 5143–5184 (2015).

136. Gelbrich, T., Marten, G. U. & Schmidt, A. M. Reversible thermoflocculation of magnetic core-shell particles induced by remote magnetic heating. *Polymer* **51,** 2818–2824 (2010).

137. Dine, E. J. Al *et al.* Efficient synthetic access to thermo-responsive core/shell nanoparticles. *Nanotechnology* **28,** 1–8 (2017).

138. Motornov, M., Roiter, Y., Tokarev, I. & Minko, S. Stimuli-responsive nanoparticles, nanogels and capsules for integrated multifunctional intelligent systems. *Prog. Polym. Sci.* **35,** 174–211 (2010).

139. Rubio-Retama, J. *et al.* Synthesis and characterization of thermosensitive PNIPAM microgels covered with superparamagnetic γ-Fe_2O_3 nanoparticles. *Langmuir* **23,** 10280–10285 (2007).

140. Wu, X. *et al.* Water-soluble dendritic-linear triblock copolymer-modified magnetic nanoparticles: preparation, characterization and drug release properties. *J. Mater. Chem.* **21,** 13611 (2011).

141. Herrera, A. P., Barrera, C., Zayas, Y. & Rinaldi, C. Monitoring colloidal stability of polymer-coated magnetic nanoparticles using AC susceptibility measurements. *J. Colloid Interface Sci.* **342,** 540–549 (2010).

142. Chen, R., Maclaughlin, S., Botton, G. & Zhu, S. Preparation of Ni-g-polymer core-shell nanoparticles by surface-initiated atom transfer radical polymerization. *Polymer.* **50,** 4293–4298 (2009).

143. Vasquez, E. S., Nicholson, W. B., Walters, K. B. & Circle, P. Surface modification of iron oxide (Fe_3O_4) micro- and nano-particles with stimuli responsive polymers. *Nano Sci. Technol. Inst. Nanotech* **1,** 612–615 (2011).

144. Kurzhals, S., Zirbs, R. & Reimhult, E. Synthesis and magneto-thermal actuation of iron oxide core-PNIPAM shell nanoparticles. *ACS Appl. Mater. Interfaces* **7,** 19342–19352 (2015).

145. Xiao, Z. P., Yang, K. M., Liang, H. & Lu, J. Synthesis of magnetic, reactive, and thermoresponsive Fe_3O_4 nanoparticles via surface-initiated RAFT copolymerization of *N*-isopropylacrylamide and acrolein. *J. Polym. Sci. Part A Polym. Chem.* **48,** 542–550 (2010).

146. Li, Q. *et al.* Multistimuli-responsive hybrid nanoparticles with magnetic core and thermoresponsive fluorescence-labeled shell via surface-initiated RAFT polymerization. *Soft Matter* **7,** 6958 (2011).

147. Dobson, J. Magnetic micro- and nano-particle-based targeting for drug and gene delivery. *Nanomedicine* **1,** 31–37 (2006).

148. Mornet, S. *et al.* Magnetic nanoparticle design for medical applications. *Prog. Solid State Chem.* **34,** 237–247 (2006).

149. Pyun, J. Nanocomposite materials from functional polymers and magnetic colloids. *Polym. Rev.* **47,** 231–263 (2007).
150. Korth, B. D. *et al.* Synthesis, assembly, and functionalization of polymer-coated ferromagnetic nanoparticles. in *ACS Symp. Ser.* **996,** 272–285 (2008).
151. Cushing, B. L., Kolesnichenko, V. L. & O'Connor, C. J. Recent advances in the liquid-phase syntheses of inorganic nanoparticles. *Chem. Rev.* **104,** 3893–3946 (2004).
152. Lu, L. T. *et al.* Size and shape control for water-soluble magnetic cobalt nanoparticles using polymer ligands. *J. Mater. Chem.* **18,** 2453 (2008).
153. Liu, G., Yan, X., Lu, Z., Curda, S. A. & Lal, J. One-pot synthesis of block copolymer coated cobalt nanocrystals. *Chem. Mater.* **17,** 4985–4991 (2005).
154. Thomas, J. R. Preparation and magnetic properties of colloidal cobalt particles. *J. Appl. Phys.* **37,** 2914–2915 (1966).
155. Griffiths, C. H., O'Horo, M. P. & Smith, T. W. The structure, magnetic characterization, and oxidation of colloidal iron dispersions. *J. Appl. Phys.* **50,** 7108–7115 (1979).
156. Burke, N. A. D., Stöver, H. D. H. & Dawson, F. P. Magnetic nanocomposites: Preparation and characterization of polymer-coated iron nanoparticles. *Chem. Mater.* **14,** 4752–4761 (2002).
157. Korth, B. D. *et al.* Polymer-coated ferromagnetic colloids from well-defined macromolecular surfactants and assembly into nanoparticle chains. *J. Am. Chem. Soc.* **128,** 6562–6563 (2006).
158. Keng, P. Y., Shim, I., Korth, B. D., Douglas, J. F. & Pyun, J. Synthesis and self-assembly of polymer-coated ferromagnetic nanoparticles. *ACS Nano* **1,** 279–292 (2007).
159. Bull, M. M. *et al.* Synthesis of ferromagnetic polymer coated nanoparticles on multi-gram scale with tunable particle size. *J. Mater. Chem.* **20,** 6023 (2010).
160. Parkes, L. M. *et al.* Cobalt nanoparticles as a novel magnetic resonance contrast agent-relaxivities at 1.5 and 3 Tesla. *Contrast Media Mol. I.* **3,** 150–156 (2008).
161. Ansari, S. M. *et al.* Cobalt nanoparticles for biomedical applications:facile synthesis, physiochemical characterization, cytotoxicity behavior and biocompatibility. *Appl. Surf. Sci.* **414,** 171–187 (2017).
162. Shimizu, T. Fabrication of pulsatile cardiac tissue grafts using a novel 3-dimensional cell sheet manipulation technique and temperature-responsive cell culture surfaces. *Circ. Res.* **90,** e40–e48 (2002).
163. Michalek, F., Lagunas, A., Jimeno, C. & Pericàs, M. A. Synthesis of functional cobalt nanoparticles for catalytic applications. Use in asymmetric transfer hydrogenation of ketones. *J. Mater. Chem.* **18,** 4692 (2008).
164. Gubin, S. & Koksharov, Y. Preparation, structure, and properties of magnetic materials based on Co-containing nanoparticles. *Inorg. Mater.* **38,** 1287–1304 (2002).
165. Coey, J. M. . Magnetism in future. *J. Magn. Magn. Mater.* **226–230,** 2107–2112 (2001).
166. He, C. *et al.* Facile synthesis of hollow porous cobalt spheres and their enhanced electromagnetic properties. *J. Mater. Chem.* **22,** 22160 (2012).

167. Dumestre, F. *et al.* Shape control of thermodynamically stable cobalt nanorods through organometallic chemistry. *Angew. Chemie - Int. Ed.* **41,** 4286–4289 (2002).

168. De La Peña O'Shea, V. A., De la Piscina, P. R., Homs, N., Aromí, G. & Fierro, J. L. G. Development of hexagonal closed-packed cobalt nanoparticles stable at high temperature. *Chem. Mater.* **21,** 5637–5643 (2009).

169. Yang, H. T. Su, Y. K. Shen, C. M. Yang, T. Z. & Gao, H. J. Synthesis and magnetic properties ofε-cobalt nanoparticles. *Surf. Interface Anal.* **36,** 155–160 (2004).

170. Jovanović, S. Spreitzer, M. Tramšek, M. Trontelj, Z. & Suvorov, D. Effect of oleic acid concentration on the physicochemical properties of cobalt ferrite nanoparticles. *J. Phys. Chem. C* **118,** 13844–13856 (2014).

3 Synthesis of Thermo-Responsive Nanocomposites of Superparamagnetic Cobalt Nanoparticles/poly(*N*-isopropylacrylamide)

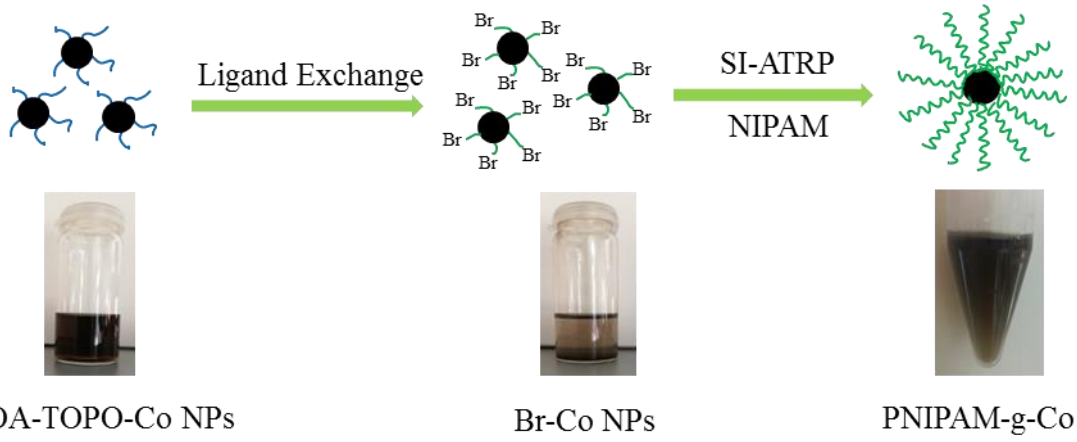

In this chapter, novel nanocomposites of superparamagnetic cobalt nanoparticles (Co NPs) and poly(*N*-isopropylacrylamide) (PNIPAM) were fabricated through surface-initiated atom-transfer radical polymerization (SI-ATRP). A functional ATRP initiator, containing an amine (as anchoring group) and a 2-bromopropionate group (SI-ATRP initiator), was synthesized at first. Oleic acid- and trioctylphosphine oxide-coated Co NPs were then modified with the initiator via ligand exchange. The process is facile and rapid for efficient surface functionalization and afterwards the Co NPs can be dispersed into polar solvent DMF without aggregation. Transmission electron microscopy, Fourier transform infrared spectroscopy, X-ray photoelectron spectroscopy, and dynamic light scattering measurements confirmed the success of ligand exchange. The following polymerization of NIPAM was conducted on the surface of Co NPs. The temperature-dependent dynamic light scattering study showed the responsive behavior of PNIPAM-coated Co NPs. The combination of superparamagnetic and thermo-responsive properties in these hybrid nanoparticles is promising for future applications e.g. in biomedicine.

3.1 Introduction

Magnetic nanoparticles (NPs) are playing increasingly important roles in biological imaging, therapeutic applications and magnetic energy storage.[1–4] The magnetic properties of ferromagnetic NPs are dominated by a hysteresis loop showing remanence and coercivity. When the size of such NPs is reduced below a critical diameter, the particles become superparamagnetic.[5] That means that in contrast to the hysteresis loop of ferromagnetic materials, the superparamagnetic nanoparticles have zero coercivity. Therefore, they are magnetized in an external magnetic field and reach their saturation magnetization rapidly. However, when the applied magnetic field is removed, they exhibit no residual magnetization. This makes superparamagnetic (SPM) NPs especially interesting for biological applications. On one hand, superparamagnetic NPs exhibit a strong and rapid response to an external magnetic field, and on the other

hand, they do not agglomerate in the body after removal of the applied magnetic field. Hence there is much less concern about blood blockage and thrombosis.[6]

Decomposition of metal precursors is one of the most important methods for preparing magnetic nanoparticles, as it results in a narrow size distribution, and provides tunability in size and shape. However, these magnetic nanoparticles are normally stabilized by hydrophobic ligands, like oleic acid (OA) and/or oleylamine, which renders the particles hydrophobic.[7,8] As a consequence, their biological applications, which require dispersion in hydrophilic or aqueous medium, are limited.[9,10] Thus, there is a great significance in the surface modification of hydrophobic nanoparticles. Ligand exchange is the most widely used method for surface modification by replacing the original ligands with designed molecules. So far, various ligand exchange reactions have been reported for Fe_3O_4 NPs, FePt NPs, QDs, Ag NPs, Au NPs, etc,.[11–21] Cobalt nanoparticles (Co NPs), due to their excellent magnetic and catalytic properties, have great potential application in various fields, such as ferrofluids, catalysis, and magnetic resonance imaging (MRI).[22–25] However, to the best of my knowledge, core/shell nanocomposites with Co NPs have been seldom studied. One reason could be their sensitivity to oxidation. Furthermore, unlike other nanoparticles that form covalent bonds with ligands (e.g. Au NPs with thiols;[26] Fe_3O_4 NPs with dopamine or silanes),[11,12] Co NPs interact with surfactants through coordinative bonds, which complicates the modification. Last but not least, Co NPs readily agglomerate both during the ligand exchange process and afterwards by excess washing steps due to the weak binding with surfactants. However, because of the promising applications, it is worth investigating the functionalization of Co NPs.

For the large majority of NP applications, they are usually surface-modified with polymers to form core/shell nanocomposites. Of various methods to synthesize NP/polymer core/shell hybrid nanoparticles, surface-initiated atom transfer radical polymerization (SI-ATRP) provides a suitable technique to synthesize a highly dense polymer brush.[27–29] SI-ATRP, as a controlled living radical polymerization, exhibits precise control over the chain lengths and thus the thickness of the grafted polymer layer.[30–37] Among the grafted polymers, stimuli-responsive polymers are especially important in many NP applications due to the variability of the nanoparticle surface properties through external stimuli.[30,31,35–37] Poly(*N*-isopropylacrylamide) (PNIPAM) is one of the most widely researched polymers. Its lower critical solution temperature (LCST) is around 32 °C, with a reversible change in the conformation structure between hydrophobic and hydrophilic.[38–40] This intrinsic thermo-responsive property can be widely used in biomedical applications, such as enzyme bioconjugates,[41,42] cell culture substrates,[43] controlled drug and gene delivery systems,[44,45] microfluidics[46] and tissue engineering for regenerative medicine.[47,48]

Herein, I investigated a ligand exchange process on Co NPs followed by SI-ATRP to prepare polymer-coated Co NPs. During this procedure, Co NPs, stabilized by oleic acid (OA) and trioxylphosphine oxide (TOPO), were synthesized via thermal decomposition method.[49] The ligand exchange process was quite rapid, typically reached in a few minutes, and a 2-bromopropionate group served as initiator for the subsequent polymerization. Consequently, NIPAM could be polymerized on the surface of Co NPs via SI-ATRP. The polymer-coated Co NPs could be easily dispersed in water and are responsive to temperature.

The presented surface modification process allows detailed future studies of Co NPs in hydrophilic medium.

3.2 Experimental Section

3.2.1 Materials

Toluene (99.5%), *n*-hexane (95%), ethanol (99.5%), and diethyl ether (99.8%) were purchased from Th. Geyer; *N,N*-dimethylformamide (DMF, 99%) was purchased from Acros Organics; tris[2-(dimethylamino)ethyl]amine (Me_6TREN), and magnesium sulfate (99.5%) were purchased from Alfa Aesar; ethyl α-bromoisobutyrate (99%), and anhydrous dichloromethane (DCM, 99.9%) were purchased from Merck KGaA; pyridine (99%), and di-*tert*-butyldicarbonate (98%) were purchased from Roth; anhydrous 1,2-dichlorobenzene (DCB, 99%), isopropanol (99.7%), di-cobalt octa-carbonyl $Co_2(CO)_8$ containing 1-5% *n*-hexane as a stabilizer, oleic acid (OA, 99%), trioctylphosphine oxide (TOPO, 90%), α-bromoisobutyryl bromide (BIBB, 98%), 2-(2-aminoethoxy)ethanol (98%), copper(I) chloride (97%), trifluoroactic acid (99%), sodium bicarbonate (99.7%), and aluminum oxide (activated, neutral, Brockmann Activity I) were purchased from Sigma Aldrich and used as received without further purification. NIPAM was obtained from Sigma Aldrich and was purified by recrystallization from a mixture of *n*-hexane and benzene (4:1 v:v). Copper(I) chloride was purified by stirring in glacial acetic acid overnight, washed with ethanol and dried under vacuum. $Co_2(CO)_8$ was kept in the fridge of a glovebox, and *n*-hexane evaporated in the glovebox before use.

3.2.2 Synthesis of OA- and TOPO-coated Co NPs

Superparamagnetic cobalt nanoparticles with an average diameter of ca. 9 nm were synthesized according to the literature.[49] In detail, 100 mg TOPO were degassed in a three-neck flask, 0.1 mL OA and 15 mL degassed anhydrous DCB were injected into the flask under N_2 flow. The mixture was heated to 182 °C and 540 mg $Co_2(CO)_8$ in 3 mL of DCB was rapidly injected at the reflux temperature. After 20 min, the temperature was reduced to room temperature. The nanoparticles suspension was collected and stored under N_2 atmosphere. To purify the nanoparticles, they were precipitated into ethanol and sedimentations were separated from solvent by using a magnet. The washing process was repeated twice and the black precipitate dried under vacuum for two days.

3.2.3 Synthesis of SI-ATRP initiator

Synthesis of (2-(*N*-Boc-2-aminoethoxy)ethanol) **1**: In a 250 mL round-bottom flask, 2-(2-aminoethoxy)ethanol (10.0 mL, 100 mmol) was dissolved in 100 mL anhydrous CH_2Cl_2 and cooled with an ice bath, then di-*tert*-butyl dicarbonate (21.8 g, 100 mmol) was added into the above solution. After addition, the ice bath was removed and the resulting mixture was stirred 6-8 h at room temperature. The mixture was washed three times with saturated aqueous NaCl solution. After drying over anhydrous $MgSO_4$ and filtration, the solvent was removed under vacuum, giving 2-(*N*-Boc-2-aminoethoxy)ethanol as

a colorless oil (15.2 g, 74 % yield). ^{1}H-NMR (500 MHz, $CDCl_3$): δ = 5.36 (s, 1H), 3.64 (t, *J* = 5.4 Hz, 2H), 3.48 (t, *J* = 4.6 Hz, 2H), 3.45 (t, *J* = 5.0 Hz, 2H), 3.37 (t, *J* = 5.9 Hz, 1H), 3.23 (m, 2H), 1.35 (s, 9H).

Synthesis of (2-(*N*-Boc-2-aminoethoxy)ethyl-2-bromoisobutyrate) **2**: 2-(*N*-Boc-2-aminoethoxy)ethanol (4.1 g, 20 mmol) was dissolved in 45 mL anhydrous CH_2Cl_2 and cooled with an ice bath. Pyridine (1.77 mL, 22 mmol) was added into the above solution. Then, 2-bromoisobutyryl bromide (2.72 mL, 22 mmol) was added dropwise while stirring. After addition, the ice bath was removed and the resulting mixture was stirred 40 min at room temperature. The precipitate was filtered off; the filtrate was then washed three times with saturated aqueous $NaHCO_3$ solution and three times with saturated aqueous NaCl solution. After drying over anhydrous $MgSO_4$ and filtration, the solvent was removed under vacuum. The resulting crude product was purified by column chromatography on silica gel (CH_2Cl_2 : ethanol = 100:1), giving 2-(*N*-Boc-2-aminoethoxy)ethyl-2-bromoisobutyrate as a colorless oil (6.0 g, 85 % yield). ^{1}H-NMR (500 MHz, $CDCl_3$): δ = 4.94 (s, 1H), 4.31 (m, 2H), 3.69 (m, 2H), 3.54 (t, *J* = 4.7 Hz, 2H), 3.30 (m, 2H), 1.93 (s, 6H), 1.42 (s, 9H).

Synthesis of (2-(2-aminoethoxy)ethyl-2-bromoisobutyrate trifluoroacetic acid) **3**: 2-(*N*-Boc-2-aminoethoxy)ethyl-2-bromoisobutyrate (2.1 g, 6.0 mmol) was dissolved in 8 mL anhydrous CH_2Cl_2 and cooled with an ice bath, then trifluoroacetic acid (4 mL, 52.3 mmol) was added while stirring. The ice bath was removed and the resulting mixture was allowed to stir 1.5 h at room temperature. The solvent was removed under vacuum and a light brown oil obtained (1.9 g, 86 % yield). ^{1}H-NMR (500 MHz, $CDCl_3$): δ = 7.39 (s, 3H), 4.36 (t, *J* = 4.6 Hz, 2H), 3.78 (m, 4H), 3.28 (m, 2H), 1.93 (s, 6H).

Synthesis of (2-(2-aminoethoxy)ethyl-2-bromoisobutyrate) **4**: The crude product **3** was stirred in a saturated aqueous $NaHCO_3$ solution while cooled with an ice bath. When pH of the solution reached to around 8, the product was extracted with CH_2Cl_2, the organic layer dried over anhydrous $MgSO_4$, filtered and the solvent removed under vacuum to obtain a light yellow oil (0.66 g, 50 % yield). ^{1}H NMR (500 MHz, $CDCl_3$): δ = 4.31 (t, *J* = 4.8 Hz, 2H), 3.69 (t, *J* = 4.8 Hz, 2H), 3.51 (t, *J* = 5.1 Hz, 2H), 2.84 (t , *J* = 4.7 Hz, 2H), 1.92 (s, 6H), 1.55 (s, 2H). ^{13}C NMR (125 MHz, $CDCl_3$): δ = 171.6, 73.3, 68.5, 65.0, 56.7, 41.7, 30.7.

3.2.4 Ligand exchange reaction of OA- and TOPO-coated Co NPs

In the ligand exchange process, 15 mg OA- and TOPO-coated Co NPs were dispersed into 15 mL *n*-hexane. 200 μL initiator in 1 mL dichloromethane was dropped into the NPs suspension while stirring. Precipitations appeared immediately and the suspension was kept stirring for 2 minutes in order to complete the ligand exchange. Then, NPs sedimentation was collected by a magnet and solvent was removed, the precipitated NPs could be easily dispersed into DMF. To purify NPs, toluene was added to flocculate the NPs in DMF suspension and NPs were collected by a magnet. The particles were either

redispersed into DMF for the polymerization or allowed to dry under vacuum for 2 days for characterization.

3.2.5 SI-ATRP of NIPAM from initiator-coated Co NPs

15 mg initiator capped Co NPs were dispersed into 6 mL DMF and 2 mL isopropanol in a 25 mL Schlenk flask. Then, NIPAM (4.52 g, 40 mmol), Me_6TREN (267 µL, 1 mmol) and 4 µL ethyl α-bromoisobutyrate were added into the flask. The mixture was degassed by three freeze-pump-thaw cycles, then CuCl (40 mg, 0.4 mmol) was added at the frozen state under N_2 flow. The system was subjected by another two freeze-pump-thaw cycles, the dispersion was stirred at 40 °C for 18 h. Then, the flask was opened to air and an appropriate amount of diethyl ether was added into the mixture, Co NPs-g-PNIPAM were collected by a magnet and purified by washing twice with CH_2Cl_2. The resulting Co NPs-g-PNIPAM were dispersed into water by slight sonication.

To estimate the molecular weight and molecular weight distribution of the grafted PNIPAM, 1 mL of the reaction mixture was diluted by adding 15 mL dichloromethane and passed through a neutral Al_2O_3 plug to remove the copper catalyst and Co NPs-g-PNIPAM. The polymer solution was concentrated and precipitated into diethyl ether (30 mL) twice to remove monomers, followed by drying in vacuum to yield a white powder for GPC and MALDI-ToF analysis.

3.2.6 Instruments

Fourier transform infrared (FT-IR) spectra were measured on Thermonicolet Nexus 470 (spectral resolution 0.125 cm^{-1}), sampling with attenuated total reflection (ATR) technique. The peak fitting was conducted in Origin 9.1 software.

TEM images were obtained by FEI Tecnai F20-ST Transmission Electron Microscopy operated at 200 kV. The samples were prepared by drop-casting a NPs suspension onto the carbon-coated copper grid, followed by drying in air. The size of OA- and TOPO-coated Co NPs was estimated by ImageJ software.

Thermogravimetric analyses (TGA) were conducted on a TA Instruments Q500. All samples were measured from 25 °C to 800 °C under a nitrogen atmosphere with a heating rate of 10 °C/min.

X-ray photoelectron spectroscopy (XPS) measurements were carried out using an AXIS165 instrument (Kratos Analytical, UK). Monochromatic Al K (alpha) radiation (300 W) was used for excitation. The instrument was run in electrostatic mode and thermal electrons from a filament were used to neutralize the sample charges. CASA-XPS software (2.3.16) was used for data processing. All quantification was carried out after subtracting a Shirley background and Gaussian-Lorentzian functions (30 % Lorentz) were used for peak fitting.

Dynamic light scattering (DLS) was conducted on a Malvern Zetasizer Nano ZS from Malvern Instruments. The temperature was varied at the rate of 0.1 °C per min. Assuming Mark-Houwink parameters to be A = 0.428 and B = $7.67 \cdot 10^{-5}$, 173° backscattering was analyzed with equilibration time of 120 s. Multi-parameter analysis was performed on an average of three runs for every data point.

The magnetic properties of Co NPs were measured by Dr. Konrad Siemensmeyer using a SQUID magnetometer (MPMS 3, by Quantum Design) at the Quantum Materials Core Lab at the Helmholtz Zentrum Berlin. The magnetic behavior of Co NPs was measured in field cooling (FC) and zero-field cooling (ZFC) modes from 5 K to 390 K under an applied field of 50 mTesla. Magnetization curves were obtained under the fields from 0 - 2 Tesla. The magnetic data were normalized from the sample mass of Co atoms.

Gel permeation chromatography (GPC) was performed using DMF with LiBr (1 mg/mL) as eluent, a flow rate of 1.0 ml/min, a high pressure liquid chromatography pump (Bischoff HPLC Compact pump) and a RI detector (Jasco RI- 2031 plus). Calibration was achieved using polystyrene standards. Results were evaluated using WinGPC Unity software.

Matrix-assisted laser desorption/ionization time-of-flight (MALDI-ToF) mass spectra were collected on a 337 nm Bruker microflex spectrometer with pulsed ion extraction. The masses were determined in positive ion linear mode. The sample solutions were applied on a ground steel target using the dried droplet technique. Millipore water: acetonitrile 7:3 with 0.1% trifluoroacetic acid was used as solvent for PNIPAM (5 mg/ml), matrix α-cyano-4-hydroxycinnamic acid (10 mg/mL), and sodium trifluoroacetate (13.6 mg/mL). Sample, matrix and salt solutions were mixed in 5:20:1 ratio and 2 µl of the mixture applied on the target.

Proton nuclear magnetic resonance (^{1}H-NMR) spectra were measured on a Varian INOVA 500 spectrometer from Barian Inc at 500 MHz. All samples were prepared in deuterated chloroform ($CDCl_3$, 99.8%). All spectra were referenced to the signal of non-deuterated solvent molecules relative to tetramethylsilane = 0 ppm.

3.3 Results and Discussion

3.3.1 Synthesis and characterization of OA- and TOPO-coated Co NPs

OA- and TOPO-coated Co NPs were prepared by thermal decomposition of octacarbonyldicobalt in 1,2-dichlorobenzene under reflux with OA and TOPO as stabilizers.[49] The size and morphology of oleic acid- and TOPO-coated Co NPs was characterized by TEM. Figure 3.1a and 3.1b show a narrow size distribution and spherical shape of as-prepared Co NPs. The average diameter is about 8.8 nm (with the variation of 0.56 nm). The critical diameter below which Co NPs become superparamagnetic is reported to be about 12 nm.[50] The magnetic behavior of the Co NPs in this study was characterized by ZFC and FC magnetic curves (Figure 3.2A) and hysteresis loops (Figure 3.2B). At 300 K, no hysteresis appears verifying the expected superparamagnetic behavior of the synthesized Co NPs. The saturation magnetization of OA- and TOPO-coated Co NPs is about 72 emu/g_{Co}, which is only half of the saturation magnetization of bulk Co (162 emu/g) at room temperature. The decrease of magnetization for the coated Co NPs compared to the bulk Co is probably due to a nonmagnetic surface layer from chemisorption of surfactants on each nanoparticles and/or a cobalt oxide surface layer.[51,52] DLS measurements (Figure 3.3) showed that OA- and TOPO-coated Co NPs are well dispersed in *n*-hexane without aggregations.

Furthermore, FT-IR spectra of free TOPO, free OA, and OA- and TOPO-coated cobalt NPs are shown in Figure 3.4. The comparison of the spectra of the free surfactants (curve a and b) and OA- and TOPO-coated NPs (curve c) shows distinct differences. The strong band at 1144 cm^{-1} ascribed to P=O (curve a) and the band at 1711 cm^{-1} corresponding to the carboxyl group of oleic acid (curve b) are absent in the spectrum of the NPs (curve c). Instead, a new band at 964 cm^{-1}, which is ascribed to P–O stretching vibration, and two new bands at 1543 cm^{-1} and 1404 cm^{-1}, which are the characteristic absorption bands of the asymmetric ν_{as} (COO^-) and symmetric ν_s (COO^-), appear. This reveals that oleic acid and TOPO are chemisorbed onto the Co NPs with the oxygen atoms coordinated to the cobalt atoms.[53,54]

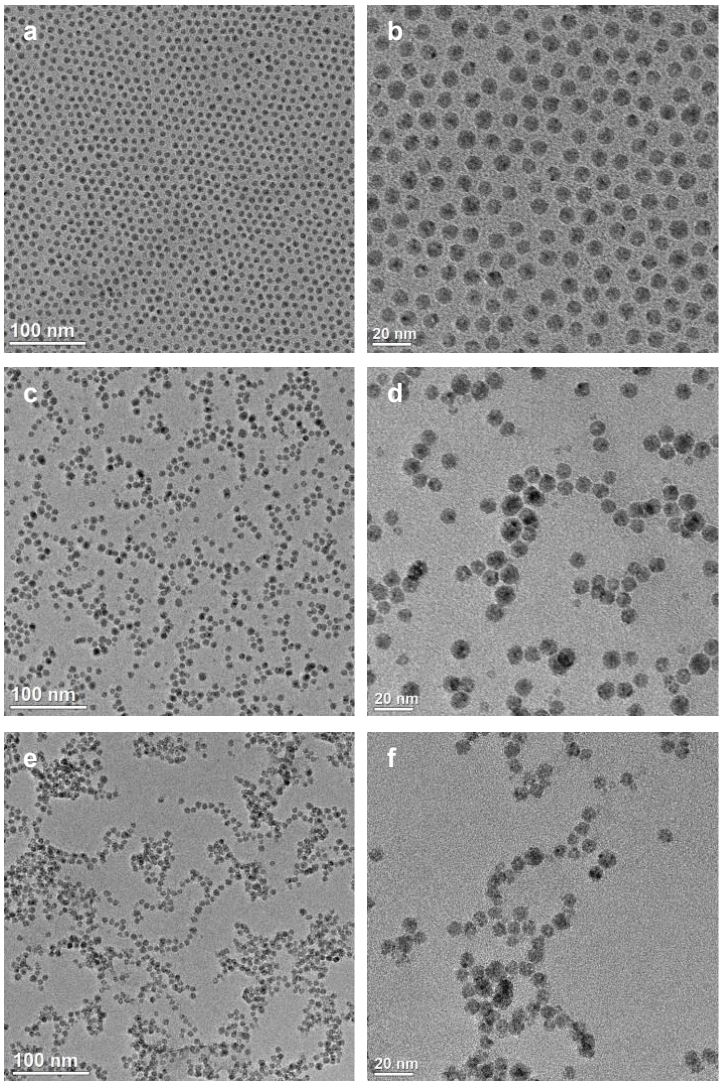

Figure 3.1 TEM images of Co NPs: (a, b) OA- and TOPO-coated Co NPs in *n*-hexane, (c, d) initiator-coated Co NPs in DMF and (e, f) Co NPs-g-PNIPAM in water.

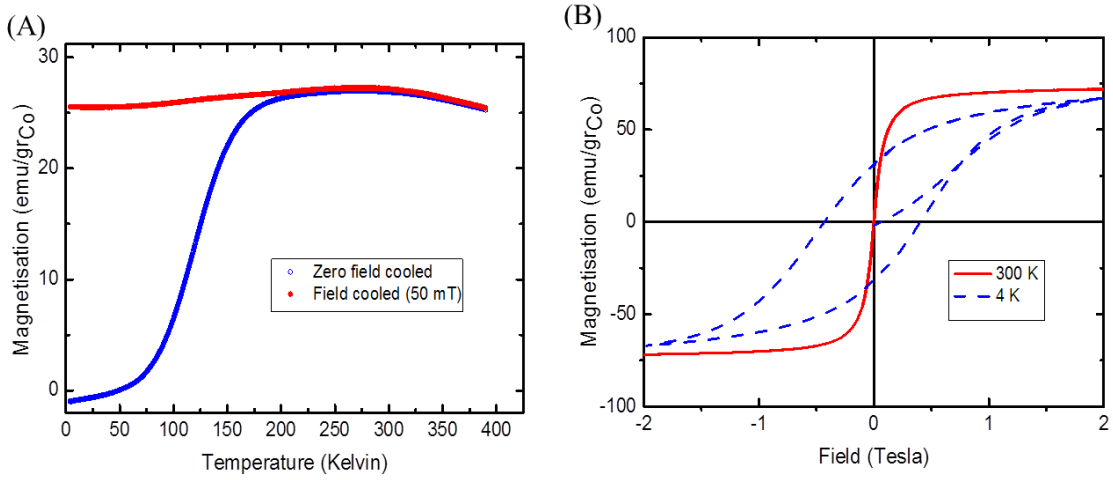

Figure 3.2 (A) Temperature dependence of zero field cooled (blue) and field cooled (red) magnetization of superparamagnetic Co NPs, measured in applied field of 50 mT; (B) Field dependence of magnetization of OA- and TOPO-coated Co NPs at 4 K and 300 K.

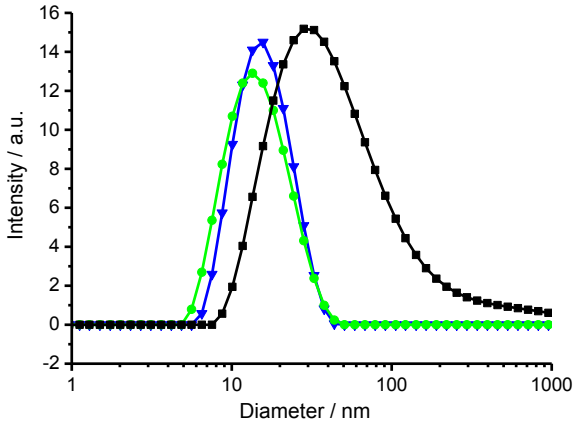

Figure 3.3 DLS measurements of OA- and TOPO-coated Co NPs in *n*-hexane (▲), initiator-coated Co NPs in DMF (●) and PNIPAM-g-Co NPs in water (■).

Furthermore, X-ray photoelectron spectroscopy (XPS) was used to examine the surface composition of oleic acid- and TOPO-coated cobalt nanoparticles. Figure 3.5 shows the XPS survey profile, the obtained binding energy of O1s is 531.9 eV, which is ascribed to OA and TOPO binding to the surface of Co NPs (curve a). Figure 3.6A shows the C1s spectra; the peak at 285.0 eV in curve a is the binding energy of C atoms which have bonds to carbon in OA and TOPO, and three peaks at 285.9 eV, 286.7 eV and 288.8 eV are associated with the C atom in C-O, O-C-O, O-C=O groups in the carboxylate group (COO^-), respectively. No C1s peak of carboxylic carbon (COOH) appeared in this spectrum, indicating that there is no free OA on the coated Co NPs.[55–57] Figure 3.7A shows the binding energy peaks of Co 2p of NPs, the peak at 778.2 eV corresponds to metal Co atoms, while the binding energies of 780.8 eV and 797.2 eV imply Co–O bond formation of carboxylate and phosphorus with cobalt atoms[53] and/or a cobalt oxide layer.[51,52]

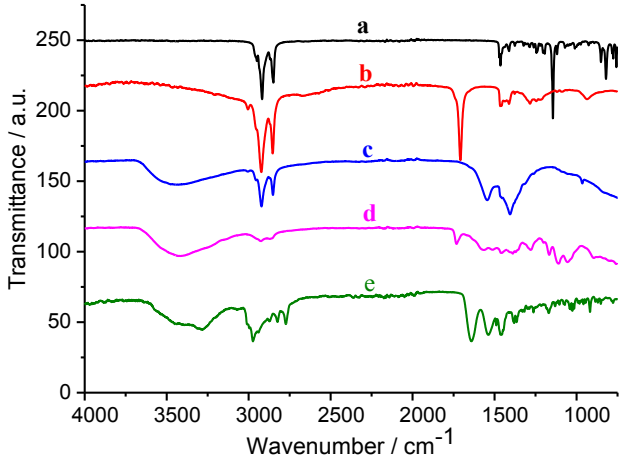

Figure 3.4 FT-IR spectra of (a) TOPO, (b) oleic acid, (c) OA- and TOPO-coated Co NPs, (d) initiator-coated Co NPs and (e) Co NPs-g-PNIPAM.

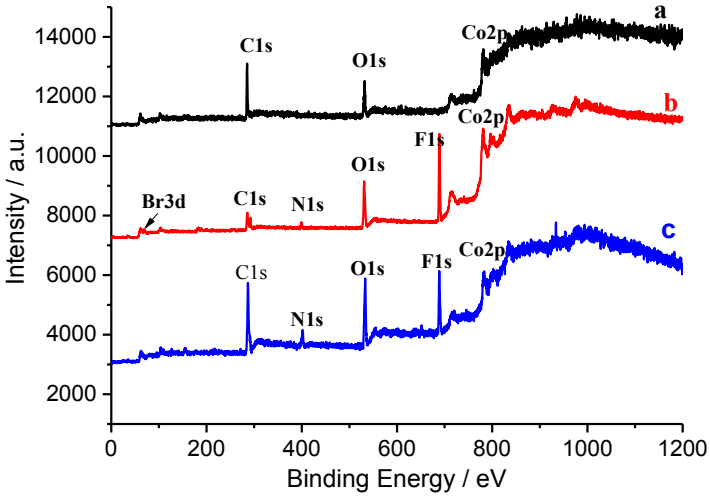

Figure 3.5 XPS survey spectra: (a) OA- and TOPO-coated Co NPs, (b) initiator-coated Co NPs and (c) Co NPs-g-PNIPAM.

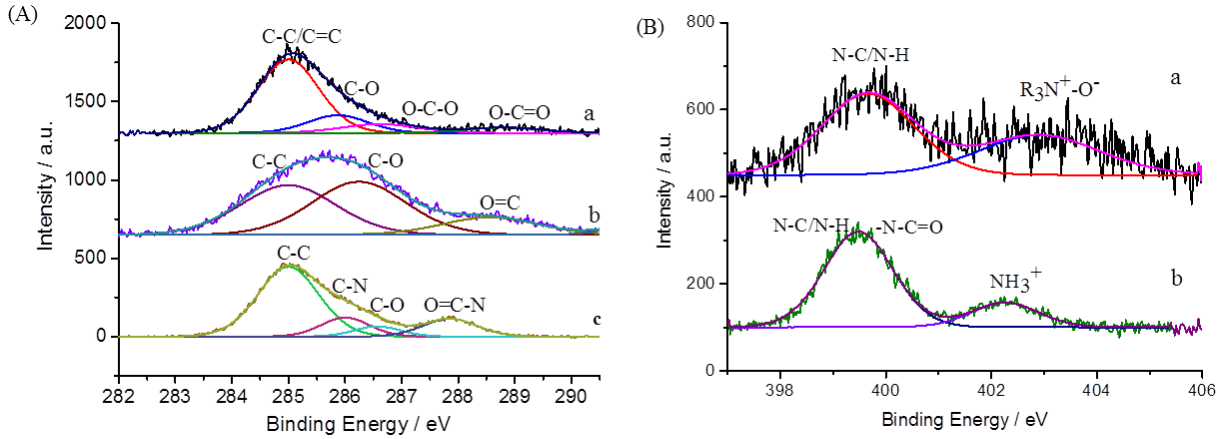

Figure 3.6 XPS spectra: (A) C1s spectra: (a) OA- and TOPO-coated Co NPs, (b) initiator-coated Co NPs and (c) Co NPs-g-PNIPAM; (B) N1s spectra: (a) initiator-coated Co NPs and (b) Co NPs-g-PNIPAM.

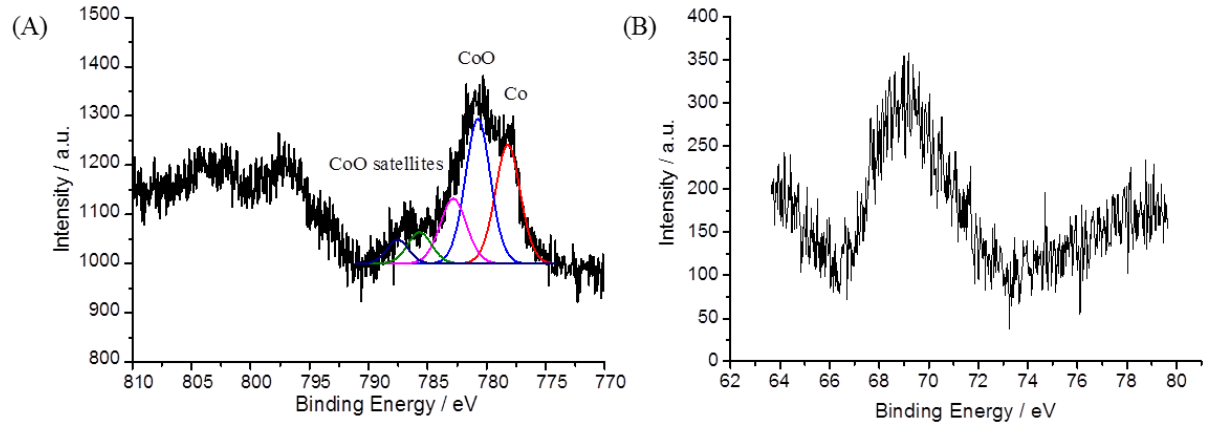

Figure 3.7 XPS spectra: (A) Co2p spectra of OA- and TOPO-coated Co NPs; (B) Br3d spectra of initiator-coated Co NPs.

3.3.2 Synthesis of ATRP initiator

In design of a functional ligand for Co NPs, both the binding properties to the NP surface as well as the initiating group for ATRP polymerization have to be considered. It is established that surfactants with functional groups -COOH, -NH_2 and -PO have strong affinity to the surface of cobalt, since N, O and P can donate the lone-pair electrons to the empty d-orbitals of Co atoms.[58] In this study, we chose a ligand containing a terminal amine group providing anchors binding to the surface of Co NPs. A 2-bromopropionate group was chosen at the other side, serving as the ATRP initiator functionality. Scheme 3.1 gives an overview of the synthesis of ATRP initiator. The amine group of 2-(2-aminoethoxy) ethanol was protected with *tert*-butyloxycarbonyl (Boc) at first. After reaction of **1** with BIBB, the protection group was removed by using trifluoroacetic acid. Compound **3** was deprotonated with aqueous $NaHCO_3$ to obtain the functional initiator **4** which was used immediately for the ligand exchange process.

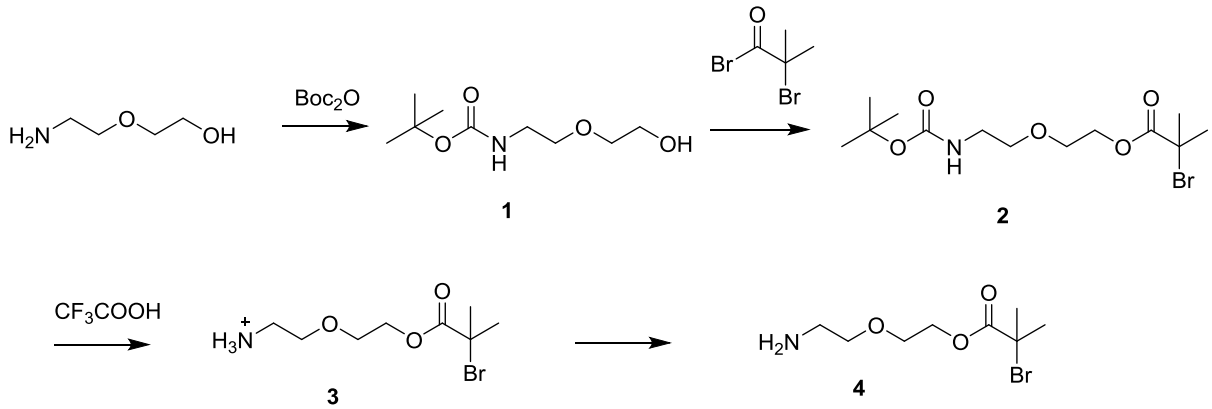

Scheme 3.1. Synthesis route for functional initiator **4**.

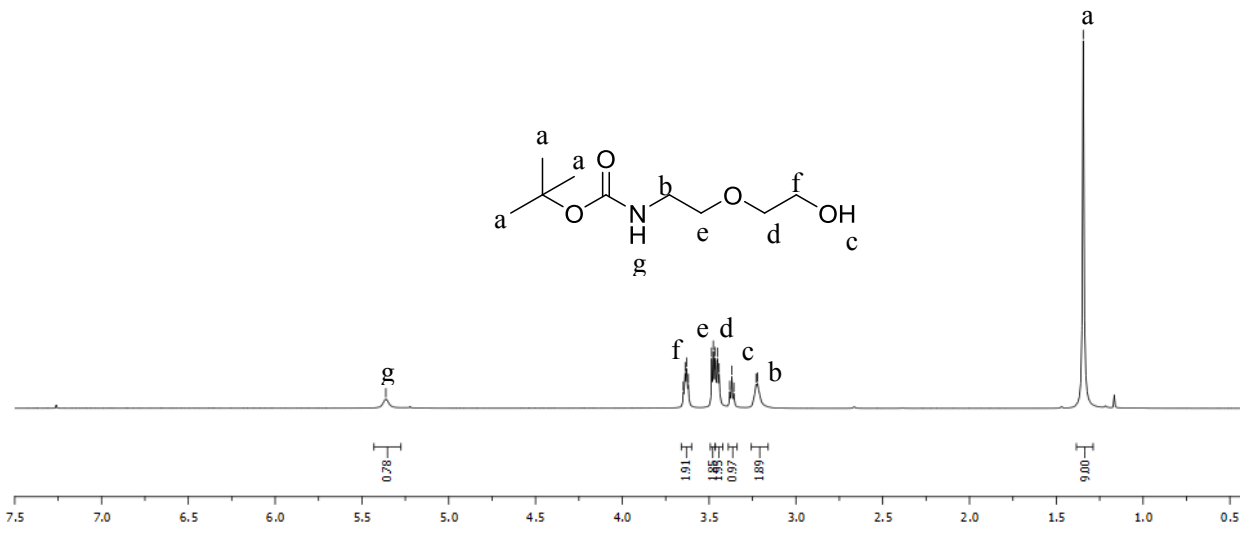

Figure 3.8 ^{1}H-NMR spectrum of **1** in $CDCl_3$.

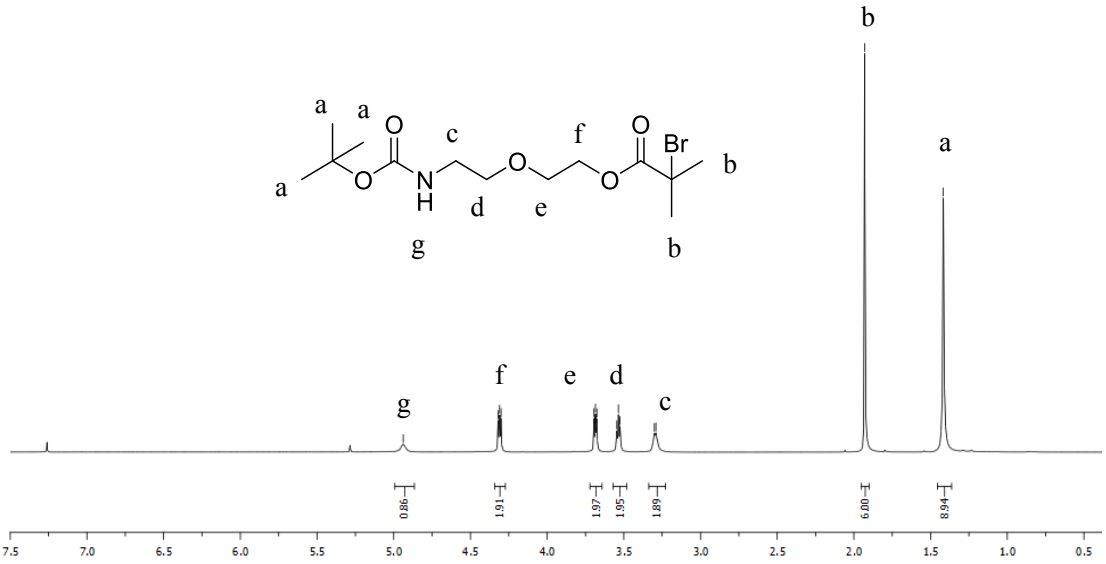

Figure 3.9 ^{1}H-NMR spectrum of **2** in $CDCl_3$.

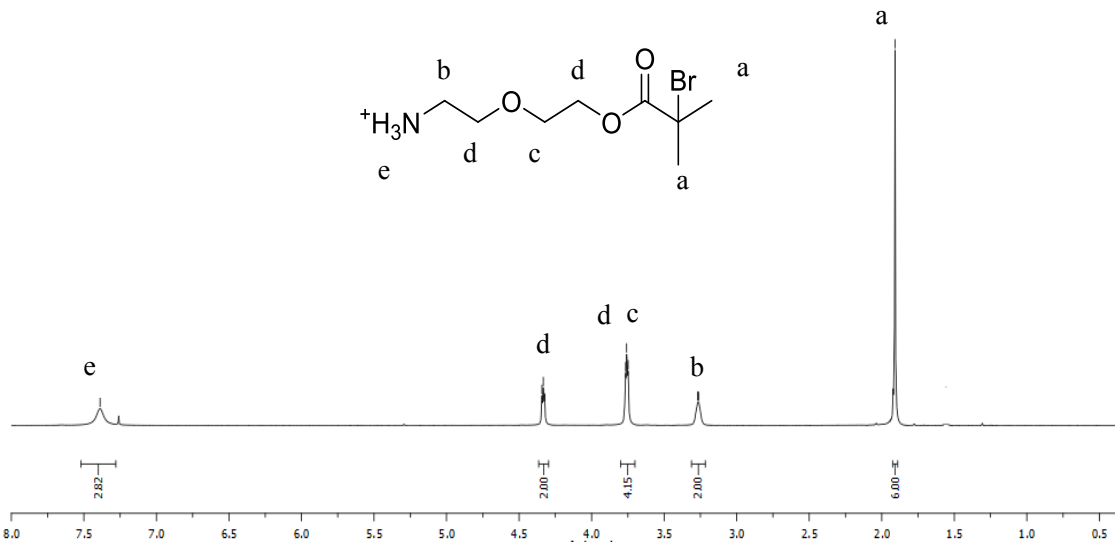

Figure 3.10 ^{1}H-NMR spectrum of **3** in $CDCl_3$.

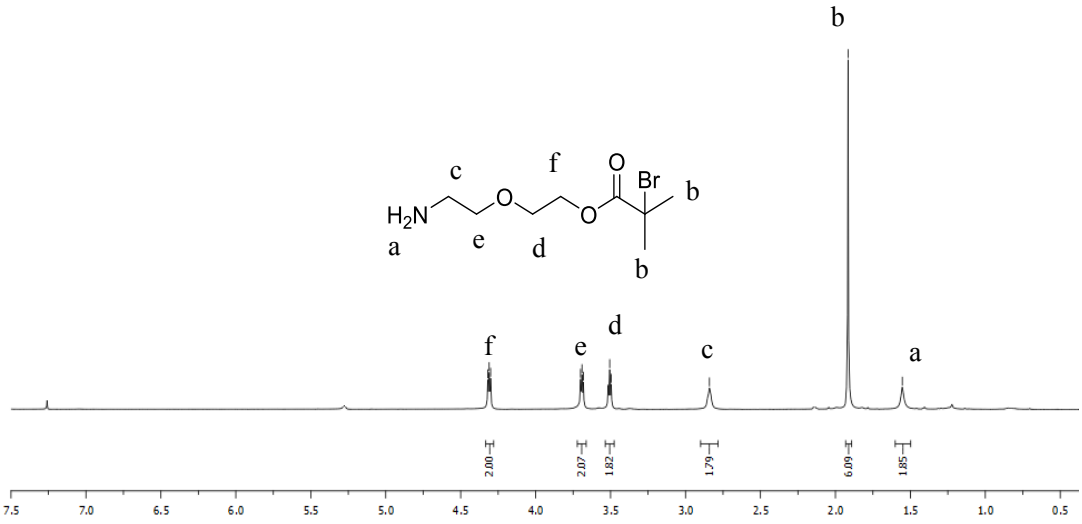

Figure 3.11 ^{1}H-NMR spectrum of **4** in $CDCl_3$.

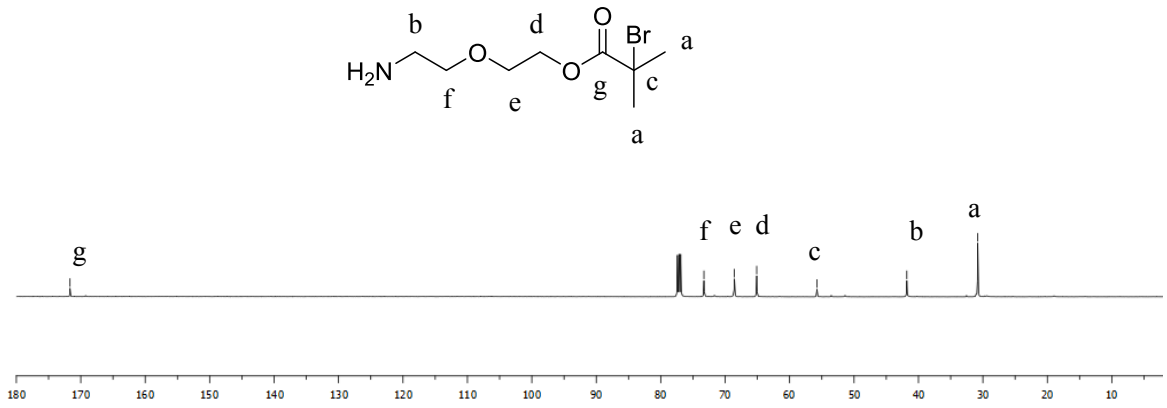

Figure 3.12 ^{13}C-NMR spectrum of **4** in $CDCl_3$.

3.3.3 Ligand exchange with functional initiator

Surface modification is a very important method to change the surface properties of NPs prepared from hydrophobic solution synthesis. In order to functionalize OA- and TOPO-coated Co NPs, ligand exchange was performed in *n*-hexane with ATRP initiator **4** solubilized in dichloromethane. As **4** is not well soluble in *n*-hexane, Co NPs should precipitate from *n*-hexane after ligand exchange. This process is inspired by the work from Dong and Murray.[59] Upon the addition of initiator, precipitation was observed immediately as shown in Figure 3.13A. Thereafter, the functionalized NPs can be easily dispersed into DMF and then purified from DMF/toluene by use of a magnet (Figure 3.13B). Before ligand exchange, Co NPs can only be dispersed into nonpolar solvents such as *n*-hexane, toluene, dichlorobenzene, etc. However, after ligand exchange, Co NPs can be dispersed into polar solvent like DMF. TEM images (Figure 3.1c, 3.1d) show that after ligand exchange, the particles are well dispersed in DMF without any aggregate formation. Meanwhile, DLS measurement shows that there is no distinct change in their size before and after the ligand exchange (Figure 3.3).

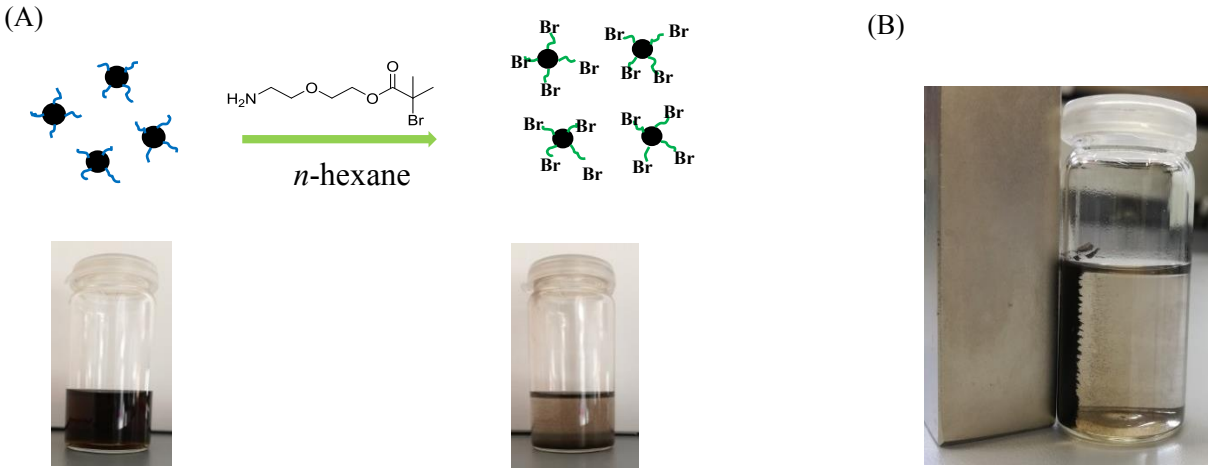

Figure 3.13 (A) Illustration of ligand exchange and altered surface properties of Co NPs; (B) Illustration of purification of Co NPs from DMF/toluene after ligand exchange. The NPs stick to the magnet nearby.

Furthermore, FTIR spectra clearly show different absorption bands before and after ligand exchange. After ligand exchange (Figure 3.4 curve d), the band corresponding to P–O stretching vibration disappeared, instead, a new characteristic band at 1730 cm^{-1} is ascribed to the carbonyl group from the attached initiators on the surface of the cobalt nanoparticles. However, a very weak absorption band of COO^- can still be found, which indicates that OA is not completely replaced by the initiator, and that OA has a stronger binding to Co than TOPO. In addition, XPS spectra also demonstrate the successful ligand exchange. As shown in Figure 3.5 (curve b), new characteristic peaks of N1s at 399.4 eV and Br3d at 68.4 eV appear. The observed binding energy of 288.5 eV belongs to the carbon atom in carbonyl group of the functional ligand (Figure 3.6A, curve b). The binding energy of N1s at 399.7 eV is ascribed to N-C and N-H of the initiator confirming the presence of the ligand with ATRP initiator (Figure 3.6B, curve a). It is worth mentioning that the peaks at 292.0 eV and 688.9 eV, are ascribed to C atoms in CF_2 groups and fluorine, respectively, of the PTFE substrate holder used for XPS measurements.

3.3.4 Calculation of grafting density of initiator

Generally, thermogravimetric analysis (TGA) is a widely used technique to evaluate the organic content on the surface of NPs.[60–62] The grafting density of initiator on the nanoparticle surface was calculated according to TGA. The equation for calculation of the grafting density of initiator on the surface of cobalt nanoparticles (φ) is shown below:

$$\varphi = \frac{N_{(org)}}{N_{(NPs)}\, S_{(NPs)}} = \frac{W_{(org)} N_A R\, \rho}{3\, M_{(org)}\, W_{(NPs)}}$$

Here, $W_{(org)}$ and $W_{(NPs)}$ present the weight loss percentage of initiator or polymer and the weight percentage of Co NPs, $N_{(org)}$ and $N_{(NPs)}$ present the number of initiator or polymer and Co NPs respectively, $S_{(NPs)}$ is the total surface area of NPs, ρ is the density of Co NPs (8.9 g/ cm^3), N_A is the Avogadro's number, R is the radius of Co NPs (4.4 nm by TEM analysis), and $M_{(org)}$ is the molecular weight of initiator or polymer.

TGA overview shows weight loss as a function of temperature for Co NPs with different ligands or grafted polymers as well as for free PNIPAM (Figure 3.14). Figure 3.14a shows the TGA profile of OA- and TOPO-coated Co NPs. The weight loss of about 3% below 200 °C is attributed to removal of adsorbed solvent.[63–65] Two significant weight loss stages of 28 % in total which are observed between 230–500 °C are attributed to the decomposition of OA and TOPO attached to the surface of Co NPs. Figure 3.14b shows the TGA profile after ligand exchange. The initial weight loss of about 3 % is equally explained by adsorbed solvent. The weight loss of about 9 % in the temperature range of 120–220 °C can be ascribed to the decomposition of functional initiator on the surface. The weight loss of about 5 % in the temperature range of 280–360 °C is probably due to the small amount of OA remaining on the surface of Co NPs, which is in accordance with the FT-IR measurement. Therefore, with $W_{(initiator)}$ = 9 % and $W_{(NPs)}$ = 68 %, we calculated the grafting density to 3.2 initiator / nm^2.

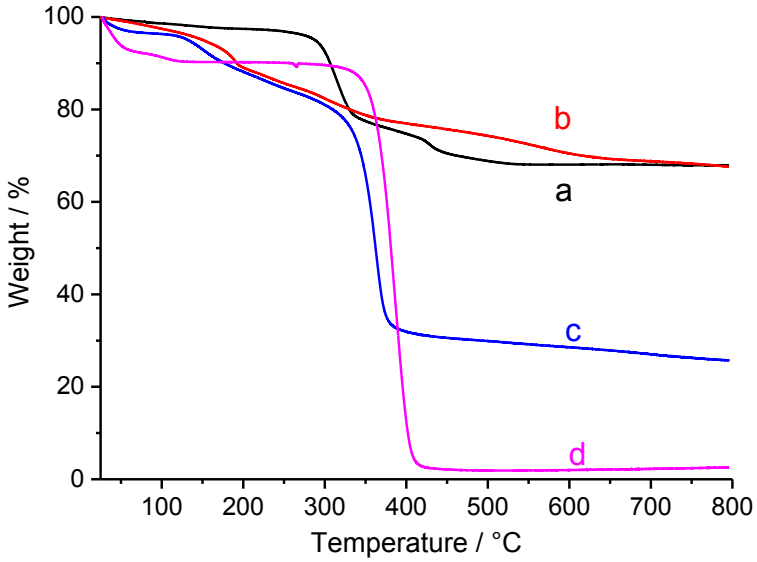

Figure 3.14 TGA analysis of Co NPs: (a) OA- and TOPO-coated Co NPs, (b) initiator-coated Co NPs, (c) Co NPs-g-PNIPAM and (d) free PNIPAM from sacrificial initiator.

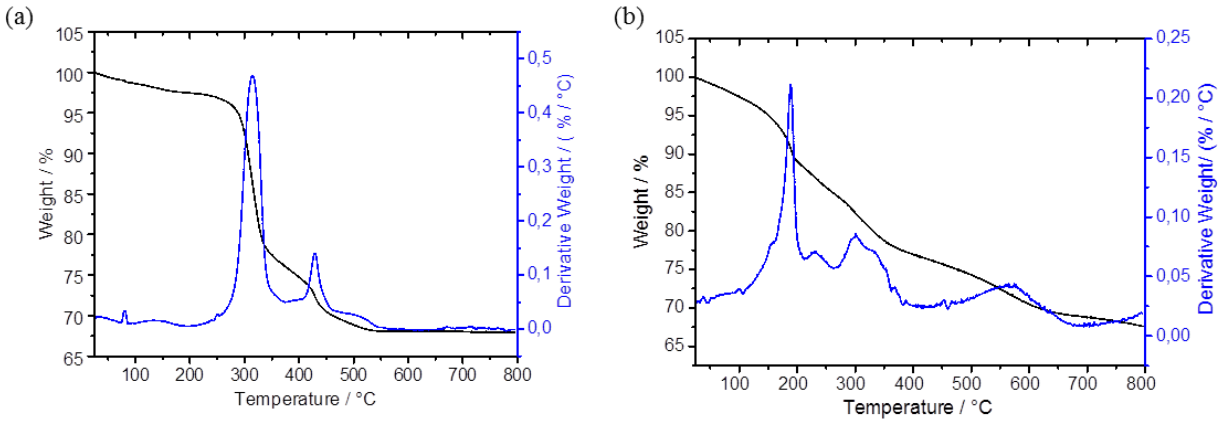

Figure 3.15 TGA analysis of Co NPs: (a) OA- and TOPO-coated Co NPs, (b) initiator-coated Co NPs. The black lines indicate the percent weight as a function of temperature and the weight loss derivative was is shown in blue.

3.3.5 Synthesis of Co NPs-g-PNIPAM via surface-initiated ATRP

Atom transfer radical polymerization (ATRP) is one of the most researched controlled radical polymerizations.[28,66–68] So far, NIPAM has been successfully polymerized via ATRP in organic solvents, pure water or mixtures of organic solvent and water.[69,70] Herein, surface-initiated ATRP of NIPAM was conducted in DMF/isopropanol (3/1) mixture according to the solubility of initiator-coated Co NPs and PNIPAM chains. CuCl/Me_6TREN was added as catalyst system. A CuCl-based catalyst was chosen to form a distinct amount of less active chloride-terminated dormant species by halogen exchange with bromide of the initiator. This allows a combination of the high initiation efficiency of the bromide initiator with a low propagation rate which renders the polymerization process more controlled.[67,71–73] Free sacrificial initiator ethyl α-bromoisobutyrate was added for the rapid accumulation of an appropriate amount of Cu^{II} through the termination of polymer radical at early stage of polymerization. The Cu^{II}

species can control the polymerization with persistent radical effect by accelerating the deactivation process and suppressing further termination reaction. Meanwhile, free polymers formed by free initiator in solution can entangle the nanoparticles and reduce the diffusion of nanoparticles, thus the termination reactions between nanoparticles can be prevented.[74] The polymerization was conducted at 40 °C. Subsequently, because Co NPs-g-PNIPAM dispersed very well in DMF and isopropanol, diethyl ether was added to flocculate the NPs and they could be easily collected by a magnet for their purification. After Co NPs-g-PNIPAM were dispersed into water, we first characterized them by TEM. As shown in Figure 3.1e and 3.1f, no obvious aggregation occurred. The dispersion was stable without aggregation for at least one week. The FTIR spectrum of the grafted NPs shows the characteristic vibration bands of PNIPAM, the band at 1642 cm^{-1} represents the amide I band (C=O), and the amide II band (N–H) at 1540 cm^{-1} appears as well (Figure 3.4e). Meanwhile, the asymmetric vibration of two methyl groups of isopropyl moiety is observed at 1466 cm^{-1} and 1457 cm^{-1}, and the symmetric vibration of the two methyl groups appears at 1381 cm^{-1} and 1364 cm^{-1}. Furthermore, the characteristic peaks at 286.0 eV and 287.8 eV in the C1s XPS spectrum in Figure 3.6A (curve c) are ascribed to C–N and N–C=O bonds, respectively. The binding energy of N1s at 399.5 eV originates from N-C/N-H and N-C=O (Figure 3.6B, curve b), which further confirms the proceeded polymerization. Due to the PNIPAM layer on the surface of cobalt nanoparticles which may shield the cobalt cores beyond the depth of XPS probing, the signal of cobalt is almost invisible (curve c in Figure 3.5).

The molecular weight and molecular weight distribution of the grafted polymer can be estimated by analysis of free polymer chains from the addition of sacrificial initiator.[31,75–77] Using a polystyrene standard, the GPC analysis gives $M_{n,GPC}$ and polydispersity index (PDI) of PNIPAM as 16 800 g/mol and 1.41, respectively (Figure 3.16A). However, the MALDI-ToF mass spectrum displays the molecular weight ($M_{n,MALDI}$) of free PNIPAM around 3750 Da (Figure 3.16B). This pronounced difference between $M_{n,GPC}$ and $M_{n,MALDI}$ could arise from the GPC calibration using PSt. Since PSt and PNIPAM have different hydrodynamic radii in the same eluent, they show different molecular weights in the same elution volume.[68,76] Hence, the $M_{n,GPC}$ of PNIPAM calculated using polystyrene as standard calibration is a relative value, and the more realistic molecular weight of PNIPAM is obtained with about 3750 Da from MALDI-ToF measurement.[73,78]

Additionally, TGA analyses of free PNIPAM and Co NPs-g-PNIPAM were studied (Figure 3.14). The initial weight loss of below 200 °C is explained by adsorbed solvent. The weight loss at the temperature range of 300–450 °C corresponds to the decomposition of surface grafted PNIPAM (Figure 3.17a) and pure PNIPAM (Figure 3.17b). The weight loss of grafted PNIPAM at the surface of Co NPs is about 50 %. Hence, with $W_{(NPs)}$ = 32 %, the grafting density of PNIPAM was calculated as 1.3 chains/nm^2 with an initiation efficiency of 0.4.

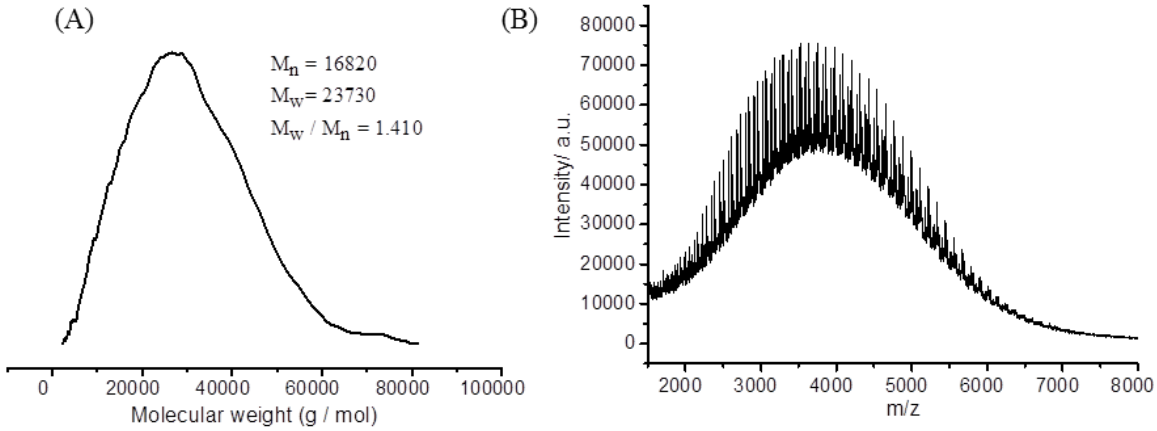

Figure 3.16 (A) GPC curve of free PNIPAM obtained from sacrificial initiator; (B) MALDI-ToF mass spectrum of free PNIPAM obtained from sacrificial initiator.

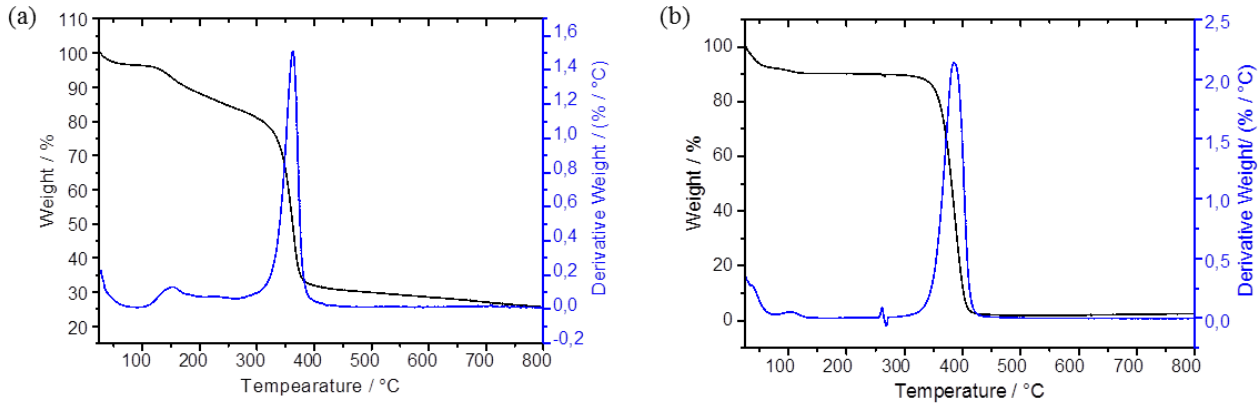

Figure 3.17 TGA analysis: (a) Co NPs-g-PNIPAM, (b) free PNIPAM from sacrificial initiator. The black lines indicate the percent weight as a function of temperature and the weight loss derivative is shown in blue.

3.3.6 Thermo-responsive behavior of Co NPs-g-PNIPAM

After polymerization of NIPAM on the surface of Co NPs, the nanocomposites are well dispersed into water (Figure 3.1 and Figure 3.3). As is well known, the LCST of pure PNIPAM is around 32 °C. By increasing the temperature, the conformation of PNIPAM changes from swollen state (T < LCST) to shrunken state (T > LCST). Therefore, the hydrodynamic diameter of the PNIPAM-coated nanoparticles was studied in the temperature range from 25 °C to 45 °C by DLS. Both increase and decrease of hydrodynamic size upon heating above the phase transition temperature was reported for PNIPAM-coated nanoparticles.[79–84] PNIPAM-coated Co NPs showed aggregation upon heating as shown in Figure 3.18. By lowering the temperature, the formed aggregates at high temperature can be redispersed, which demonstrates that the aggregation behavior is reversible. During the cooling process, the rehydration of the polymer chains has to overcome the adhesion between the particles.[80] Therefore, a hysteresis can be observed and the hydrodynamic diameter between 20–25 °C is slightly higher compared to the heating curve. TEM images from samples prepared at 45 °C also showed the aggregation behavior (Figure 3.19). It was reported that NPs with high polymer grafting density tend to show shrinkage rather than aggregation upon heating above their LCST, but those with low grafting density are more likely to

colloidally aggregate.[85] This is an indication that the grafting density of the Co NPs-g-PNIPAM is rather low.

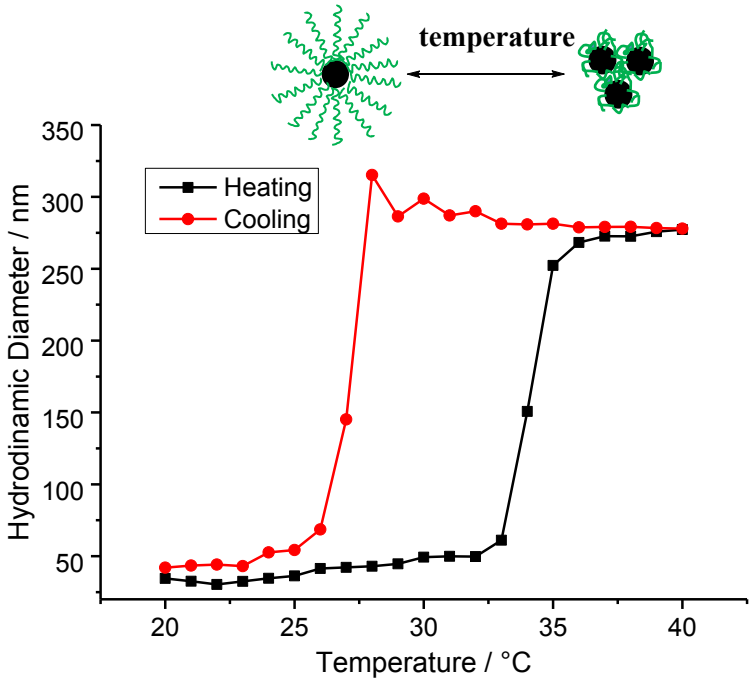

Figure 3.18 DLS measurement of hydrodynamic diameter as a function of temperature.

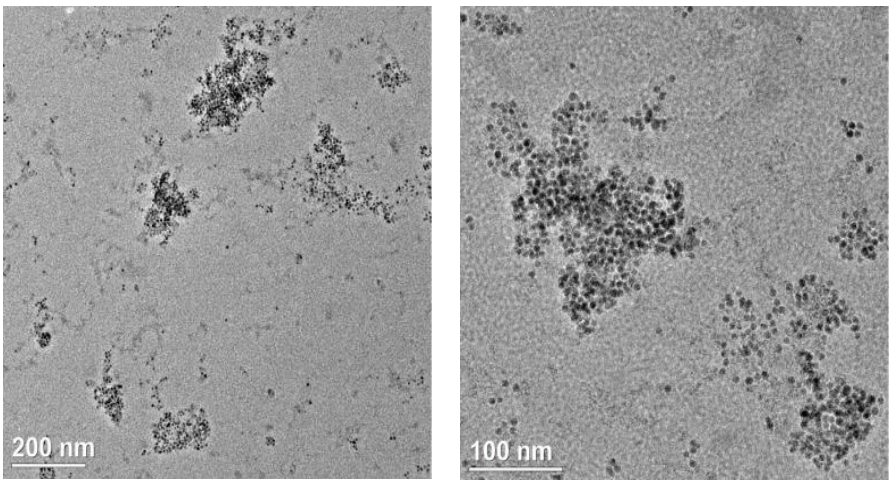

Figure 3.19 TEM images of Co NPs-g-PNIPAM prepared at 45 °C which causes aggregation.

3.4 Conclusions

In summary, SI-ATRP of NIPAM was performed on the surface of superparamagnetic cobalt nanoparticles to fabricate thermo-responsive cobalt-polymer nanocomposites. A facile and rapid ligand-exchange process was obtained to modify the surface of Co NPs with SI-ATRP initiator. The as-prepared Co NPs-g-PNIPAM nanocomposites were dispersable in water without aggregation and the grafting density of polymer was calculated to 1.3 chains/nm^2 from TGA analysis. The hybrid particles are responsive to temperature and showed aggregation behavior by increasing temperature above the phase

transition. The combination of superparamagnetic and thermo-responsive hybrid core-shell nanoparticles has great potential in biological applications.

3.5 References

1. de Dios, A. S. & Díaz-García, M. E. Multifunctional nanoparticles:analytical prospects. *Anal. Chim. Acta* **666,** 1–22 (2010).
2. Frey, N. A., Peng, S., Cheng, K. & Sun, S. Magnetic nanoparticles:synthesis, functionalization, and applications in bioimaging and magnetic energy storage. *Chem. Soc. Rev.* **38,** 2532 (2009).
3. Corot, C., Robert, P., Idée, J. M. & Port, M. Recent advances in iron oxide nanocrystal technology for medical imaging. *Adv. Drug Deliv. Rev.* **58,** 1471–1504 (2006).
4. Mornet, S., Vasseur, S., Grasset, F. & Duguet, E. Magnetic nanoparticle design for medical diagnosis and therapy. *Forunal Mater. Chem.* **14,** 2161–2175 (2004).
5. Kolhatkar, A. G., Jamison, A. C., Litvinov, D., Willson, R. C. & Lee, T. R. Tuning the magnetic properties of nanoparticles. *Int. J. Mol. Sci.* **14,** 15977–16009 (2013).
6. Akbarzadeh, A., Samiei, M. & Davaran, S. Magnetic nanoparticles: preparation, physical properties, and applications in biomedicine. *Nanoscale Res. Lett.* **7,** 144 (2012).
7. Park, J., Joo, J., Soon, G. K., Jang, Y. & Hyeon, T. Synthesis of monodisperse spherical nanocrystals. *Angew. Chemie-Int. Ed.* **46,** 4630–4660 (2007).
8. Kang, Y. & Murray, C. B. Synthesis and electrocatalytic properties of cubic Mn-Pt nanocrystals (Nanocubes).*J. Am. Chem. Soc.* **132,** 7568–7569 (2010).
9. Medintz, I. L., Uyeda, H. T., Goldman, E. R. & Mattoussi, H. Quantum dot bioconjugates for imaging, labelling and sensing. *Nat. Mater.* **4,** 435–446 (2005).
10. Bruchez Jr., M. Semiconductor nanocrystals as fluorescent biological labels. *Science.* **281,** 2013–2016 (1998).
11. Salgueiriño-Maceira, V., Liz-marza, L. M. & Farle, M. Water-based ferrofluids from Fe_xPt_{1-x} nanoparticles synthesized in organic media. *Langmuir*. 6946–6950 (2004).
12. Xie, J., Xu, C., Kohler, N., Hou, Y. & Sun, S. Controlled PEGylation of monodisperse Fe_3O_4 nanoparticles for reduced non-specific uptake by macrophage cells. *Adv. Mater.* **19,** 3163–3166 (2007).
13. Hong, R., Fischer, N. O., Emrick, T. & Rotello, V. M. Surface PEGylation and ligand exchange chemistry of FePt nanoparticles for biological applications. *Chem. Mater.* **17,** 4617–4621 (2005).
14. De Palma, R. *et al.* Silane ligand exchange to make hydrophobic superparamagnetic nanoparticles water-dispersible. *Chem. Mater.* **19,** 1821–1831 (2007).
15. Herrera, A. P., Barrera, C., Zayas, Y. & Rinaldi, C. Monitoring colloidal stability of polymer-coated magnetic nanoparticles using AC susceptibility measurements. *J. Colloid Interface Sci.* **342,** 540–549 (2010).
16. Kim, M., Chen, Y., Liu, Y. & Peng, X. Super-stable, high-quality Fe_3O_4 dendron-nanocrystals

dispersible in both organic and aqueous solutions. *Adv. Mater.* **17,** 1429–1432 (2005).

17. Tangirala, R., Baker, J. L., Paul Alivisatos, A. & Milliron, D. J. Modular inorganic nanocomposites by conversion of nanocrystal superlattices. *Angew. Chemie - Int. Ed.* **49,** 2878–2882 (2010).
18. Kovalenko, M. V. *et al.* Semiconductor nanocrystals functionalized with antimony telluride zintl ions for nanostructured thermoelectrics. *J. Am. Chem. Soc.* **132,** 6686–6695 (2010).
19. Chaves, R. *et al.* Colloidal nanocrystals with molecular. *Science.* **324**. 1417–1420 (2009).
20. Kim, S. B., Cai, C., Kim, J., Sun, S. & Sweigart, D. A. Surface modification of Fe_3O_4 and FePt magnetic nanoparticles with organometallic complexes. *Organometallics* **28,** 5341–5348 (2009).
21. Wei, Y., Yang, J. & Ying, J. Y. Reversible phase transfer of quantum dots and metal nanoparticles. *Chem. Commun.* **46,** 3179 (2010).
22. Ansari, S. M. *et al.* Cobalt nanoparticles for biomedical applications: Facile synthesis, physiochemical characterization, cytotoxicity behavior and biocompatibility. *Appl. Surf. Sci.* **414,** 171–187 (2017).
23. Michalek, F., Lagunas, A., Jimeno, C. & Pericàs, M. A. Synthesis of functional cobalt nanoparticles for catalytic applications. Use in asymmetric transfer hydrogenation of ketones. *J. Mater. Chem.* **18,** 4692 (2008).
24. Shimizu, T. Fabrication of pulsatile cardiac tissue grafts using a novel 3-dimensional cell sheet manipulation technique and temperature-responsive cell culture surfaces. *Circ. Res.* **90,** 40e–48 (2002).
25. Parkes, L. M. *et al.* Cobalt nanoparticles as a novel magnetic resonance contrast agent-relaxivities at 1.5 and 3 Tesla. *Contrast Media Mol. I.* **3,** 150–156 (2008).
26. Ingram, R. S., Hostetler, M. J. & Murray, R. W. Poly-hetero-ω-functionalized alkanethiolate-stabilized gold cluster compounds. *J. Am. Chem. Soc.* **119,** 9175–9178 (1997).
27. Matyjaszewski, K. Atom transfer radical polymerization and the synthesis of polymeric materials. *Adv. Mater.* **10,** 901–915 (1998).
28. Matyjaszewski, K. Bulk atom transfer radical polymerization. *Chem. Rev.* **101,** 96–112 (2001).
29. Wang, J. S. & Matyjaszewski, K. Controlled/"living" radical polymerization. atom transfer radical polymerization in the presence of transition-metal complexes. *J. Am. Chem.Soc* **117,** 5614–5615 (1995).
30. Feng, Q., Tang, D., Lv, H., Zhang, W. & Li, W. Temperature-responsive zinc oxide nanorods arrays grafted with poly(*N*-isopropylacrylamide) via SI-ATRP. *RSC Adv.* **5,** 62024–62032 (2015).
31. Li, D., He, Q., Cui, Y. & Li, J. Fabrication of pH-responsive nanocomposites of gold nanoparticles /poly(4-vinylpyridine). *Chem. Mat.* **19**. 412–417 (2007).
32. Wu, L., Glebe, U. & Böker, A. Surface-initiated controlled radical polymerizations from silica nanoparticles, gold nanocrystals, and bionanoparticles. *Polym. Chem.* **6,** 5143–5184 (2015).
33. Nuss, S., Böttcher, H., Wurm, H. & Hallensleben, M. L. Gold nanoparticles with covalently attached polymer chains. *Angew. Chemie Int. Ed.* **40,** 4016–4018 (2001).
34. Ohno, K., Koh, K., Tsujii, Y. & Fukuda, T. Synthesis of gold nanoparticles coated with well-

defined, high-density polymer brushes by surface-initiated living radical polymerization. *Macromolecules* **35,** 8989–8993 (2002).

35. Duan, H. *et al.* pH-responsive capsules derived from nanocrystal templating. *Langmuir* **21,** 11495–11499 (2005).
36. Duan, H., Kuang, M., Wang, D., Kurth, D. G. & Möhwald, H. Colloidally stable amphibious nanocrystals derived from poly{[2-(dimethylamino)ethyl] methacrylate} capping. *Angew. Chemie - Int. Ed.* **44,** 1717–1720 (2005).
37. Wu, T., Ge, Z. & Liu, S. Fabrication of thermoresponsive cross-linked poly(*N*-isopropylacrylamide) nanocapsules and silver nanoparticle-embedded hybrid capsules with controlled shell thickness. *Chem. Mater.* **23,** 2370–2380 (2011).
38. Heskins, M. & Guillet, J. E. Solution properties of poly(*N*-isopropylacrylamide). *J. Macromol. Sci. Part A - Chem.* **2,** 1441–1455 (1968).
39. Schild, H. G. Poly(*N*-isopropylacrylamide):experiment , theory and application. *Prog. Polym. Sci.* **17,** 163–249 (1992).
40. Gandhi, A., Paul, A., Sen, S. O. & Sen, K. K. Studies on thermoresponsive polymers:phase behaviour, drug delivery and biomedical applications. *Asian J. Pharm. Sci.* **10,** 99–107 (2015).
41. Chilkoti, A., Stayton, P. S., Chen, G. & Hoffman, A. S. Site-Specific conjugation of a temperature-sensitive polymer to a genetically-engineered protein. *Bioconjug. Chem.* **5,** 504–507 (1994).
42. Matsukata, M., Aoki, T., Sanui, K., Ogata, N. & Kikuchi, A. Effect of molecular architecture of poly(*N*-isopropylacrylamide)-trypsin conjugates on their solution and enzymatic properties. *Bioconjugate Chem.* 96–101 (1996).
43. Yamada, N. *et al.* Thermo-responsive polymeric surfaces; control of attachment and detachment of cultured cells. *Die Makromol. Chemie, Rapid Commun.* **11,** 571–576 (1990).
44. Kurisawa, M., Yokoyama, M. & Okano, T. Gene expression control by temperature with thermo-responsive polymeric gene carriers. *J. Control. Release* **69,** 127–137 (2000).
45. Gammas, S. *et al.* Thermo-responsive polymer nanoparticles with a core-shell micelle structure as site-specific drug carriers. *J. Control. Release* **48,** 157–164 (1997).
46. Yu, C. *et al.* Flow control valves for analytical microfluidic chips without mechanical parts based on thermally responsive monolithic polymers. *Anal. Chem.* **75,** 1958–1961 (2003).
47. Bao, Y., Pakhomov, A. B. & Krishnan, K. M. Brownian magnetic relaxation of water-based cobalt nanoparticle ferrofluids. *J. Appl. Phys.* **99,** (2006).
48. Yamato, M. & Okano, T. Cell sheet engineering. *Mater. Today* **7,** 42–47 (2004).
49. Puntes, V. F., Zanchet, D., Erdonmez, C. K. & Alivisatos, A. P. Synthesis of hcp-Co Nanodisks. *J. Am. Chem. Soc.* 12874–12880 (2002).
50. Alagiri, M., Muthamizhchelvan, C. & Hamid, S. B. A. Synthesis of superparamagnetic cobalt nanoparticles through solvothermal process. *J. Mater. Sci. Mater. Electron.* **24,** 4157–4160 (2013).
51. Held, G. A., Grinstein, G., Doyle, H., Sun, S. & Murray, C. B. Competing interactions in dispersions of superparamagnetic nanoparticles. *Phys. Rev. B* **64,** 012408 (2001).

52. Murray, C. B., Sun, S., Doyle, H. & Betley, T. Monodisperse 3d transition-metal (Co, Ni, Fe) nanoparticles and their assembly into nanoparticle superlattices. *MRS Bull.* **26,** 985–991 (2001).
53. Wu, N. *et al.* Interaction of fatty acid monolayers with cobalt nanoparticles. *Nano Lett.* **4,** 383–386 (2004).
54. Yang, H. T. *et al.* Stable cobalt nanoparticles passivated with oleic acid and triphenylphosphine. *Nanotechnology* **15,** 70–74 (2004).
55. Zhang, L., He, R. & Gu, H. C. Oleic acid coating on the monodisperse magnetite nanoparticles. *Appl. Surf. Sci.* **253,** 2611–2617 (2006).
56. Guan, X. H., Chen, G. H & Shang, C. ATR-FTIR and XPS study on the structure of complexes formed upon the adsorption of simple organic acids on aluminum hydroxide. *J. Environ. Sci.* **19,** 438–443 (2007).
57. He, H. & Gao, C. General approach to individually dispersed, highly soluble, and conductive graphene nanosheets functionalized by nitrene chemistry. *Chem. Mater.* **22,** 5054–5064 (2010).
58. Bao, Y., An, W., Heath Turner, C. & Krishnan, K. M. The critical role of surfactants in the growth of cobalt nanoparticles. *Langmuir* **26,** 478–483 (2010).
59. Dong, A. *et al.* A generalized ligand-exchange strategy enabling sequential surface functionalization of colloidal nanocrystals. *J. Am. Chem. Soc.* **133,** 998–1006 (2011).
60. Babu, K. & Dhamodharan, R. Synthesis of polymer grafted magnetite nanoparticle with the highest grafting density via controlled radical polymerization. *Nanoscale Res. Lett.* **4,** 1090–1102 (2009).
61. Benoit, D. N. *et al.* Measuring the grafting density of nanoparticles in solution by analytical ultracentrifugation and total organic carbon analysis. *Anal. Chem.* **84,** 9238–9245 (2015).
62. Mansfield, E., Tyner, K. M., Poling, C. M. & Blacklock, J. L. Determination of nanoparticle surface coatings and nanoparticle purity using microscale thermogravimetric analysis. *Anal. Chem.* **86,** 1478–1484 (2014).
63. Prakash, A. *et al.* Bylayers as phase transfer agents for nanocrystals prepared in nonpolar solvents. *ACS Nano* **3,** 2139–2146 (2009).
64. Rostami, A., Atashkar, B. & Moradi, D. Synthesis, characterization and catalytic properties of magnetic nanoparticle supported guanidine in base catalyzed synthesis of α-hydroxyphosphonates and α-acetoxyphosphonates. *Appl. Catal. A Gen.* **467,** 7–16 (2013).
65. Wang, M., Peng, M.-L., Cheng, W., Cui, Y.-L. & Chen, C. A Novel approach for transferring oleic acid capped iron oxide nanoparticles to water phase. *J. Nanosci. Nanotechnol.* **11,** 3688–3691 (2011).
66. Kato, M., Kamigaito, M., Sawamoto, M. & Higashimuras, T. Polymerization of methyl methacrylate with the carbon. *Macromolecules* **28,** 1721–1723 (1995).
67. Wang, J. S. & Matyjaszewski, K. Controlled/"living" radical polymerization. Halogen atom transfer radical polymerization promoted by a Cu(I)/Cu(II) redox process. *Macromolecules* **28,** 7901–7910 (1995).
68. Kamigaito, M., Ando, T. & Sawamoto, M. Metal-catalyzed living radical polymerization. *Chem.*

Rev. **101,** 3689-3746 (2001).

69. Nagase, K. *et al.* Effect of reaction solvent on the preparation of thermo-responsive stationary phase through a surface initiated atom transfer radical polymerization. *J. Chromatogr. A* **1218,** 8617–8628 (2011).
70. Ye, J. & Narain, R. Water-assisted atom transfer radical polymerization of *N*-isopropylacrylamide: nature of solvent and temperature. *J. Phys. Chem. B* **113,** 676–681 (2009).
71. Matyjaszewski, K. Atom transfer radical polymerization (ATRP): current status and future perspectives. *Macromolecules* **45,** 4015–4039 (2012).
72. Peng, C. H., Kong, J., Seeliger, F. & Matyjaszewski, K. Mechanism of halogen exchange in ATRP. *Macromolecules* **44,** 7546–7557 (2011).
73. Wu, L., Glebe, U. & Böker, A. Synthesis of hybrid silica nanoparticles densely grafted with thermo and pH dual-responsive brushes via surface-initiated ATRP. *Macromolecules* **49,** 9586–9596 (2016).
74. von Werne, T. & Patten, T. E. Atom transfer radical polymerization from nanoparticles: a tool for the preparation of well-defined hybrid nanostructures and for understanding the chemistry of controlled/"living" radical polymerizations from surfaces. *J. Am. Chem. Soc.* **123,** 7497–7505 (2001).
75. Mougin, N. C., Van Rijn, P., Park, H., Müller, A. H. E. & Böker, A. Hybrid capsules via self-assembly of thermoresponsive and interfacially active bionanoparticle-polymer conjugates. *Adv. Funct. Mater.* **21,** 2470–2476 (2011).
76. Pyun, J. & Matyjaszewski, K. Synthesis of nanocomposite organic / inorganic hybrid materials using controlled /"Living" radical polymerization. *Synthesis* 3436–3448 (2001).
77. Li, D., Sheng, X. & Zhao, B. Environmentally responsive 'hairy' nanoparticles:mixed homopolymer brushes on silica nanoparticles synthesized by living radical polymerization techniques. *J. Am. Chem. Soc.* **127,** 6248–6256 (2005).
78. Schilli, C. Novel Precursors for polymer-protein conjugate synthesis via reversible addition-fragmentation chain transfer polymerization. (2003).
79. Chakraborty, S., Bishnoi, S. W. & Pe, H. gold nanoparticles with poly(*N*-isopropylacrylamide) formed via surface initiated atom transfer free radical polymerization exhibit unusually slow aggregation kinetics. *J. Phys. Chem. C* **114,** 5947–5955 (2010).
80. Kurzhals, S., Zirbs, R. & Reimhult, E. Synthesis and magneto-thermal actuation of iron oxide core-PNIPAM shell nanoparticles. *ACS Appl. Mater. Interfaces* **7,** 19342–19352 (2015).
81. Marcelo, G. & Fernández-García, M. Direct preparation of PNIPAM coating gold nanoparticles by catechol redox and surface adhesion chemistry. *RSC Adv.* **4,** 11740–11749 (2014).
82. Raula, J. *et al.* Synthesis of gold nanoparticles grafted with a thermoresponsive polymer by surface-induced polymerization. *Polymer* 3499–3504 (2003).
83. Won, S., Phillips, D. J., Walker, M. & Gibson, M. I. Co-operative transitions of responsive-polymer coated gold nanoparticles; precision tuning and direct evidence for co-operative

aggregation. *J. Mater. Chem. B* **4,** 5673–5682 (2016).

84. Dani, R. K., Schumann, C., Taratula, O. & Taratula, O. Temperature-tunable iron oxide nanoparticles for remote-controlled drug release. *AAPS PharmSciTech* **15,** 963–972 (2014).

85. Gibson, M. I. & O'Reilly, R. K. To aggregate, or not to aggregate? considerations in the design and application of polymeric thermally-responsive nanoparticles. *Chem. Soc. Rev.* **42,** 7204–7213 (2013).

4 Magnetic-Field-Induced Assembly of Superparamagnetic Cobalt Nanoparticles

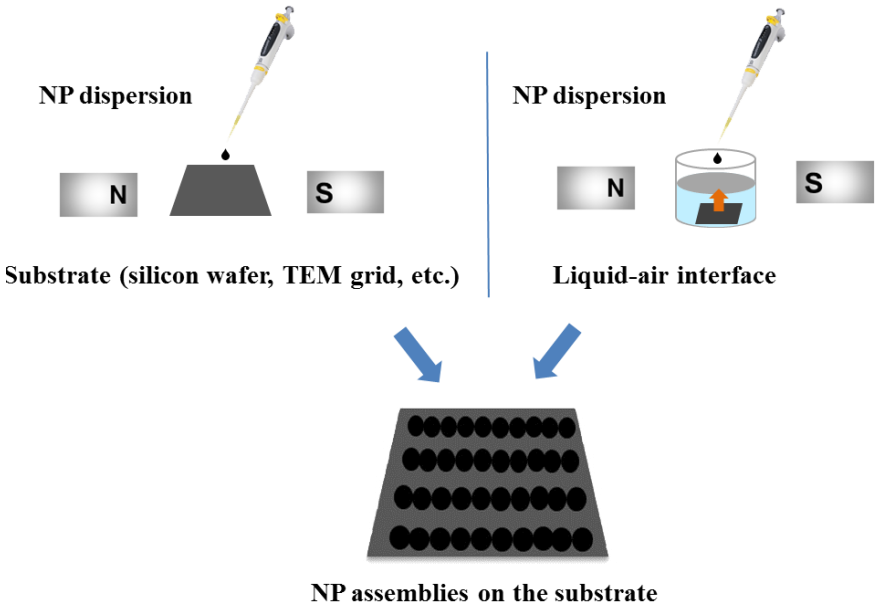

In this chapter, the magnetic-field-induced assembly of superparamagnetic cobalt nanoparticles both on solid substrates and at liquid-air interfaces was investigated. Oleic acid- and trioctylphosphine oxide-coated superparamagnetic Co NPs were synthesized via a thermolysis of cobalt carbonyl and dispersed into either hexane or toluene. The Co NP dispersion was dropped onto different substrates (e.g., TEM grid, silicon wafer) and at the liquid-air (water-air or ethylene glycol-air) interface. Transmission electron microscopy (TEM), scanning force microscopy (SFM), as well as scanning electron microscopy (SEM) showed that superparamagnetic Co NPs assembled into 1-D chains in an external magnetic field. By varying the concentration of the Co NP dispersion and the strength of the magnetic field, the morphology of the chains changed. In comparison, the assembly of Co NPs from hexane dispersion at ethylene glycol-air interface showed the most regular and homogeneous alignment, since a more efficient spreading could be achieved on ethylene glycol than on water and substrates.

4.1 Introduction

Magnetic nanoparticles have attracted great attention due to their potential application in various fields, such as high-density data storage, magnetic energy storage, drug delivery, biological imaging and medical applications.[1–7] For the electronics and magnetic switching, the ordering of magnetic nanoparticles plays an important role. In fact, understanding the assembly behavior of magnetic nanoparticles is essential to design the magnetic media, which would have much higher density data storage than that of the hard drives in computers. Thus, the investigation of assembly of magnetic nanoparticles is of great significance. Magnetic-field-induced assembly of magnetic nanoparticles provides a unique method for the assembly of

1-D, 2-D and 3-D superlattices. Due to the rapid response (within one second) and remote control, magnetic-field-induced assembly has been widely investigated.[8,9]

Among the various types of magnetic NPs, superparamagnetic NPs are most suitable for reversible assembly.[10] On the one hand, superparamagnetic NPs have a higher saturation magnetization compared with paramagnetic NPs, thus, they exhibit a stronger response to the applied magnetic field. On the other hand, their magnetic interaction can be controlled by an external magnetic field: when the magnetic field is applied, they are aligned in the direction of the external magnetic field, after removal of the magnetic field, no magnetization remains and they are disassembled.[11,12]

The 1-D chain structures are the result of dipole-dipole interaction between the superparamagnetic NPs. When superparamagnetic NPs are under an external magnetic field, they are magnetized. The magnetic dipole moment of superparamagnetic NPs, when the magnetic field is low, can be calculated with the formula: $m = \chi VH$, where χ is the particle's volume susceptibility, V is the particle's volume and H is the magnetic field.[13,14] When the external magnetic field is strong enough, the magnetic moments of NPs reach a saturation value. The induced magnetic field of one particle can affect any surrounding particle, and the dipole-dipole interaction with the second particle depends on the angle of the connecting line between the center of these two particles and the direction of the applied magnetic field.[13,15,16] When the angle is in the range of 0° to 54.09°, they attract each other, and when the angle is between 54.09° to 90°, repulsive interaction dominates. Thus, 1-D chain structures are formed due to the attractive dipolar interaction.[13,14]

The magnetic-field-induced assembly can be conducted by deposition of a magnetic nanoparticle dispersion either on substrates or at liquid-air interfaces. Numerous studies about the magnetic-field-induced assembly of magnetic NPs into 1-D superlattices have been reported.[17–22] The influence of the strength of the external magnetic field and the concentration of the NP dispersion on the magnetic assembly behavior have also been investigated on substrates.[19,20,23] Cobalt bulk material has a relatively high saturation magnetization (161 emu/g), compared with magnetite (92 emu/g), which is an ideal material for the application in the high density data storage.[24,25] Thus, the investigation of magnetic-field-induced assembly of Co NPs is of great significance. However, the magnetic-field-induced assembly of superparamagnetic Co NPs at liquid-air interface by varying parameters (e.g., strength of the applied magnetic field, concentration of Co NP dispersion) has never been reported. Herein, the assembly behavior of pre-synthesized OA- and TOPO-coated superparamagnetic Co NPs was investigated under the applied magnetic field at ethylene glycol-air interface by varying the concentration of Co NP dispersion and the strength of the magnetic field. For comparison, the magnetic-field-induced assembly behavior of superparamagnetic Co NPs on substrates and at the water-air interface was also investigated.

4.2 Experimental Section

4.2.1 Materials

N-hexane (95%) and ethanol (99.5%) were purchased from Th. Geyer; acetonitrile (HPLC grade) was purchased from VWR. Ethylene glycol (99.5%) was purchased from Carl Roth. Anhydrous 1,2-dichlorobenzene (DCB, 99%), cobalt carbonyl $Co_2(CO)_8$ containing 1-5% *n*-hexane as a stabilizer, oleic acid (OA, 99%) and trioctylphosphine oxide (TOPO, 90%) were purchased from Sigma Aldrich. All the chemicals were used as received without further purification. Neodymium magnets N45 (45×45×6 mm) were obtained from an online company, MagnetMax. Silica wafers were washed by a standard RCA (Radio Corporation of America) cleaning procedure.[26]

4.2.2 Synthesis of Co NPs

OA- and TOPO-coated Co NPs with size around 9 nm were prepared according to the literature.[27] In brief, 100 mg TOPO and 0.1 mL OA were dissolved in 15 mL degassed anhydrous DCB. 540 mg $Co_2(CO)_8$ in 3 mL of DCB was rapidly injected in the mixture at the reflux temperature of 182 °C. After 15 min, the temperature was reduced to 140 °C, and the reaction mixture stirred for another 15 min. The mixture was allowed to cool to the room temperature. The nanoparticle suspension was collected and precipitated into ethanol. The sedimentations were collected by centrifugation, and dispersed in *n*-hexane or toluene with concentrations ranging from 1–5 mg/mL for the investigation of magnetic-field-induced assembly.

4.2.3 Magnetic-field-induced assembly procedure

4.2.3.1 Magnetic-field-induced assembly on substrates by drop-casting

A clean silicon wafer (1×1 cm) or carbon-coated TEM grid was placed between two neodymium magnets. The distance between the two magnets was adjusted to 6.8 cm, 10.5 cm and 21 cm. OA- and TOPO-coated Co NPs were dispersed in toluene at different concentration of 1 mg/mL, 2.5 mg/mL and 5 mg/mL. 10 μL or 4 μL of the dispersion was dropped on the silicon wafer or TEM grid. The system was covered with a cap and left for 20 min until toluene was completely evaporated.

4.2.3.2 Magnetic-field-induced assembly at water-air interface

A glass beaker (diameter ≈ 4.5 cm, height ≈ 7.0 cm) was filled with MilliQ-grade water and was placed between two neodymium magnets until the water surface height reaches the middle of the magnets. The distance between the two magnets was adjusted to 10.5 cm. Co NPs were dispersed in toluene at different concentration of 1 mg/mL and 5 mg/mL. 15 μL of Co NP dispersion in toluene was carefully dropped on the water surface. The system was left for 3 h until toluene was completely evaporated. The film was carefully transferred onto the substrates by placing a silicon wafer under the film, followed by lifting up and drying in air.

4.2.3.3 Magnetic-field-induced assembly at ethylene glycol-air interface

A small Teflon well (diameter ≈ 2 cm, height ≈ 1.8 cm) was half-filled with ethylene glycol and was placed between two neodymium magnets. The distance between the two magnets was adjusted to 6.8 cm, 10.5 cm and 21 cm. OA- and TOPO-coated Co NPs were dispersed in *n*-hexane at different concentration

of 1 mg/mL, 2.5 mg/mL and 5 mg/mL. 15 μL of the dispersion was carefully dropped on the ethylene glycol surface. The system was left for 20 min until hexane was completely evaporated. Afterwards, 500 μL acetonitrile was added carefully along the wall of the Teflon well, so that the film was transferred from the ethylene glycol-air interface to the acetonitrile-air interface. Finally, the film was transferred onto substrates by placing a silicon wafer or a TEM grid under the floating film, followed by lifting up and drying in air.

4.2.4 Instruments

Transmission electron microscopy (TEM) characterization was performed by FEI Titan 80-300 microscope operated at 300 kV. The samples were prepared by drop-casting a NP suspension onto a carbon-coated copper grid under magnetic field or transferring a film by gently placing a grid under the film and lifting up, followed by drying in air. The size of OA- and TOPO-coated Co NPs was estimated by ImageJ software.

Scanning electron microscopy (SEM) images were obtained by JSM6330F from JOEL operated at the voltage of 5 kV and current of 12 μA. Samples were sputtered with platinum at a thickness of 4 nm.

Scanning force microscopy (SFM) images were obtained by Bruker Dimension Icon with Tapping Mode and OTESPA tip (k = 42 N/m, f_o = 300 kHz). The analysis and processing of the images were done by Nanoscope Analysis (Version 1.5).

4.3 Results and Discussion

4.3.1 Synthesis of OA- and TOPO-coated Co NPs

OA- and TOPO-coated Co NPs were synthesized by thermal decomposition of cobalt carbonyl in 1,2-dichlorobenzene under reflux with OA and TOPO as stabilizers.[27] The size and morphology of oleic acid- and TOPO-coated Co NPs was characterized by TEM. Figure 4.1a and 4.1b show a narrow size distribution and spherical shape of as-prepared Co NPs. The average diameter is about 9.0 nm (with the variation of 0.64 nm).

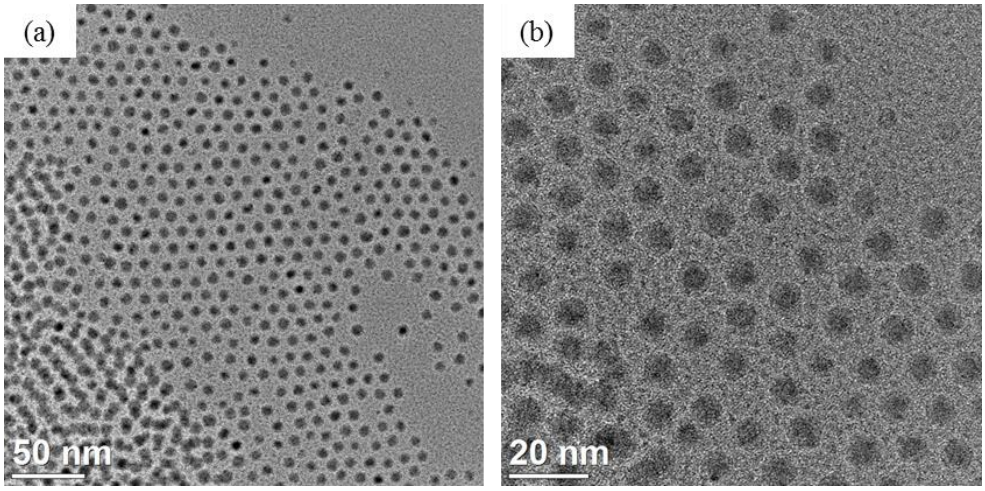

Figure 4.1 TEM images of OA- and TOPO-coated Co NPs in 1,2-dichlorobenzene.

4.3.2 Effect of concentration under the fixed applied magnetic field

When an external magnetic field is applied to superparamagnetic nanoparticles, the induced magnetic dipoles in a nanoparticle can interact with the surrounding particles, which is the so-called dipole-dipole interaction. Due to the gradient of magnetic field, the induced magnetic dipoles can also interact with the applied magnetic field, which is called dipole-field force, or the packing force. The packing force drives the magnetic nanoparticles to the area with strongest magnetic field, which leads to redistribution of NPs, and hence change the local NP concentrations during the magnetic NPs assembly.[28–30] Furthermore, the strength of the applied magnetic field can determine the induced moment in NPs, which affects the NP-NP interaction. Thus, the concentration of the nanoparticles and the applied magnetic field are very important factors which influence the assembly behavior of magnetic nanoparticles. At first, with fixed magnetic field strength, we used three different initial concentrations for the assembly process.

4.3.2.1 Magnetic-field-induced assembly on substrates by drop-casting

The as-prepared OA- and TOPO-coated Co NPs were dispersed in toluene and dropped onto different substrates, silicon wafer and TEM grid, in presence of an external magnetic field, as visualized in Figure 4.2. For the drop-casting method, the slow evaporation of the solvent plays an important role in the self-assembly into well-ordered structures. Thus a carrier solvent with high boiling-point like *n*-octane or toluene was used. Furthermore, the evaporation under a relatively high degree of solvent saturation atmosphere is also helpful to obtain a uniform film on the substrates. In view of low boiling point of *n*-hexane, toluene was chosen as the solvent to disperse Co NPs. At first, two magnets with the distance of 10.5 cm were fixed on a table, then, a silica wafer or a TEM grid was placed between the two magnets. The strength of the magentic field was calculated as 22 mT.[31] A Co NP dispersion with a concentration of 5 mg/mL or 1 mg/mL, respectively, was dropped onto the substrates, and the carrier solvent was allowed to evaporate. By varying the concentration of the Co NP dispersion, a different assembly behavior under the magnetic field was observed. Figure 4.3 and Figure 4.4 show the characterization of the resulting structures with SFM and TEM, respectively, when using a concentration of 5 mg/mL. All the images show that the Co NPs aligned in the direction of the applied magnetic field. Figure 4.3a shows that the 1-D chains are straight and closely distributed. However, the height of these chains varied (as shown in Figure 4.3b and Figure 4.3c), which indicated that the assembly was inhomogeneous. TEM characterization showed the close-packed Co NPs alignment (Figure 4.4). When the concentration of the Co NP dispersion was reduced to 1 mg/mL, the nanoparticles also assembled into 1-D chains. However, the length and the height of these chains decreased. In comparison of Figure 4.4 and Figure 4.5, multi-layers were formed at higher concentration, while monolayers and double layers were obtained at lower concentration. This can be explained by the fact that higher concentration allows high fraction of short dipolar chains, which will result in longer and thicker chains under applied magnetic field. This is in agreement with simulations conducted by other groups before.[32,33]

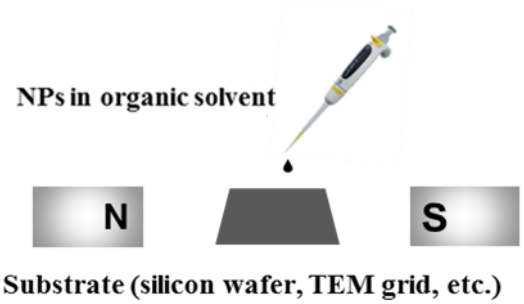

Figure 4.2 Illustration of magnetic-field-induced assembly of Co NPs on substrates.

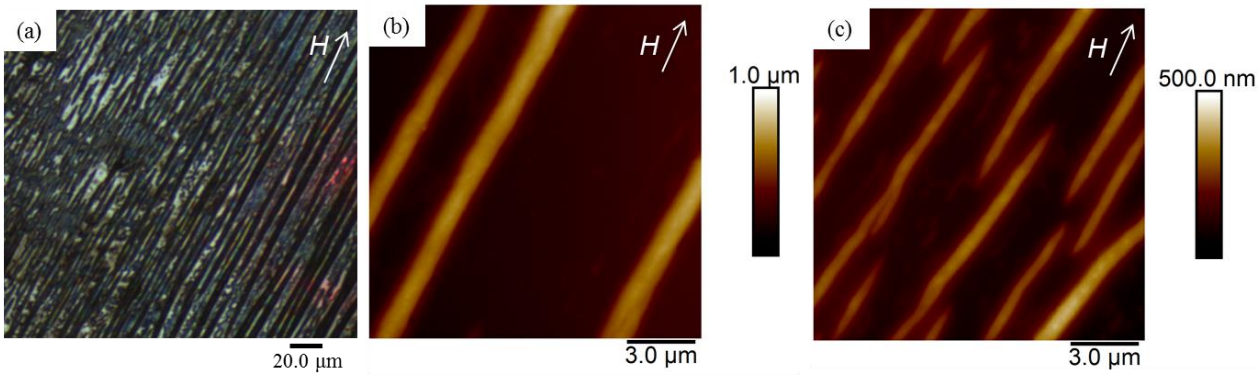

Figure 4.3 Magnetic-field-induced assembly of OA- and TOPO-coatedd Co NPs (5 mg/mL in toluene) by drop-casting on substrates: (a) SFM optical microscope image (the red color in the picture is the scattering from the laser of the SFM); (b, c) SMF height images of different areas in (a). The strength of the applied magnetic field is 22 mT and the direction of the magnetic field is indicated by the white arrow.

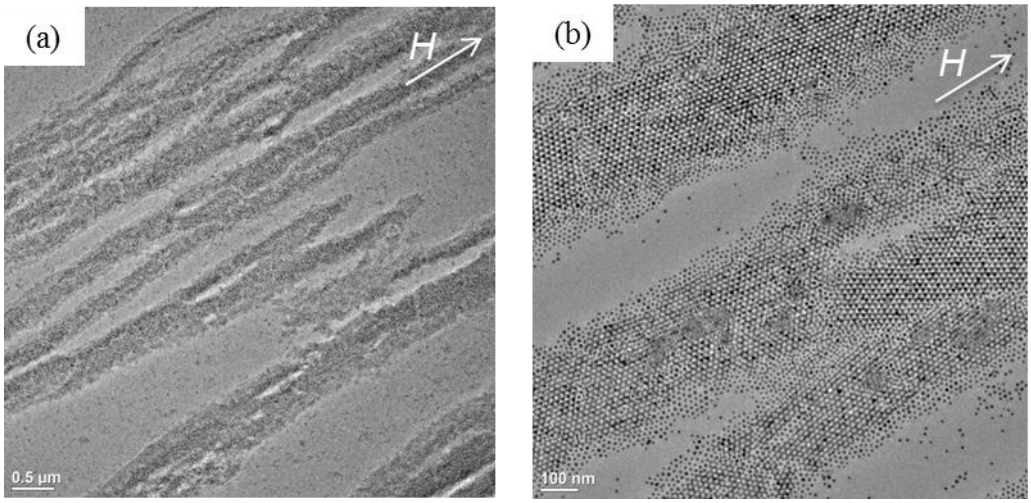

Figure 4.4 TEM images at different magnification of magnetic-field-induced assembly of OA- and TOPO-coated Co NPs (5 mg/mL in toluene) on a TEM grid. The strength of the applied magnetic field is 22 mT and the direction of the magnetic field is indicated by the white arrow.

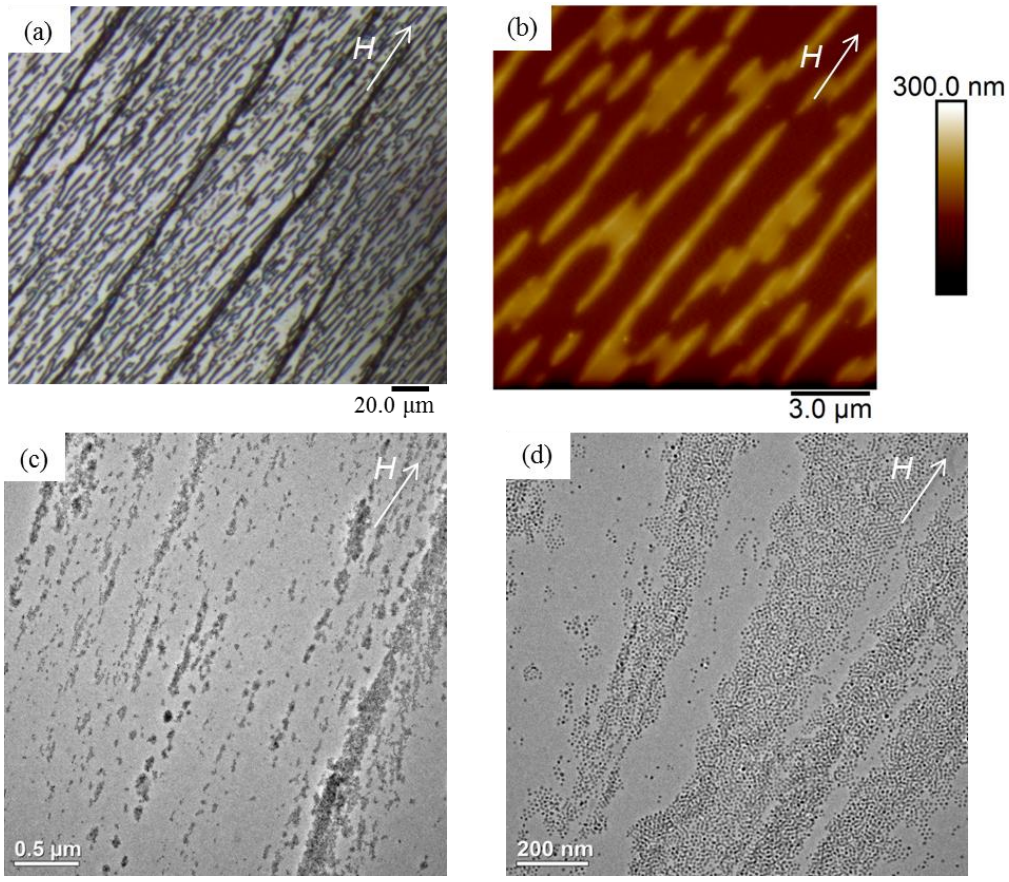

Figure 4.5 Magnetic-field-induced assembly of OA- and TOPO-coated Co NPs (1 mg/mL in toluene) on substrates: (a) SFM optical microscope image; (b) SFM height image; (c, d) TEM images at different magnifications. The strength of the applied magnetic field is 22 mT and the direction of the magnetic field is indicated by the white arrow.

4.3.2.2 Magnetic-field-induced assembly at water-air interface

In general, the assembly of nanoparticles at the water-air interface is conducted through the Langmuir technique, and a monolayer of nanoparticles can be obtained under certain conditions.[34–37] Such a monolayer can be transferred to various substrates (e.g. TEM grids, silica wafer, highly oriented pyrolytic graphite (HOPG)). Within this thesis, the experiments for the magnetic-field-induced assembly at the water-air interface were conducted by simply dropping the Co NP dispersion carefully on the water surface. Due to the large difference in polarity between water and hexane, NPs dispersed in hexane could not spread well on the water surface (Figure 4.6a). However, NPs in toluene provided a uniform distribution on the water surface, as shown in Figure 4.6b. Thus, toluene, instead of hexane, was used as the carrier solvent (Figure 4.6). As illustrated in Figure 4.7, two magnets with the distance of 10.5 cm were fixed on a table and a glass beaker filled with water was then placed between the two magnets. The magnetic field was calculatled as 22 mT.[31] Co NPs dispersed in toluene with a concentration of 5 mg/mL were carefully dropped onto the water surface. After the evaporation of toluene, the NP assemblies were transferred on a silicon wafer by dipping a silicon wafer under the floating film, followed by slowly lifting up. As shown in Figure 4.8a, the NPs formed very thick chains in the direction of the applied magnetic

field. When using the lower concentration of 1 mg/mL, much thinner chains were obtained, which is in agreement with the observed assembly on substrates in the external magnetic field (chapter 4.3.2.1). However, the films formed on water surface were discontinuous. Thus, a large area of the film is difficult to obtain by this method.

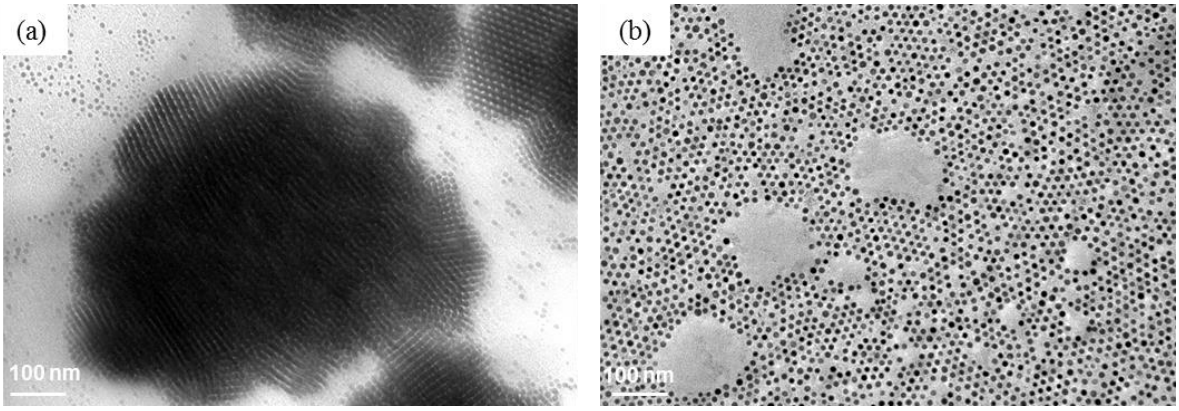

Figure 4.6 TEM images after assembly of Co NPs assembly at the water-air interface without an external magnetic field and transfer to a TEM grid; the concentration of the Co NP dispersion was 1 mg/mL: (a) Co NPs dispersed in *n*-hexane; (b) Co NPs dispersed in toluene.

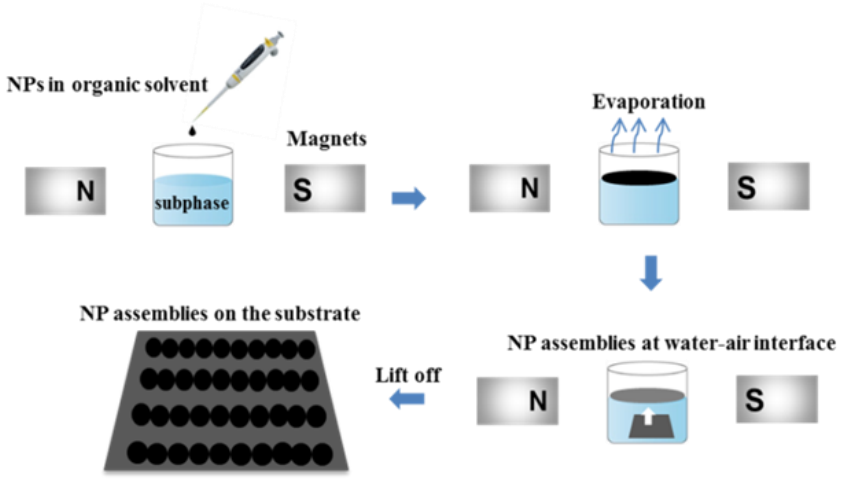

Figure 4.7 Illustration the procedure of magnetic-field-induced assembly of the Co NPs at water-air interface.

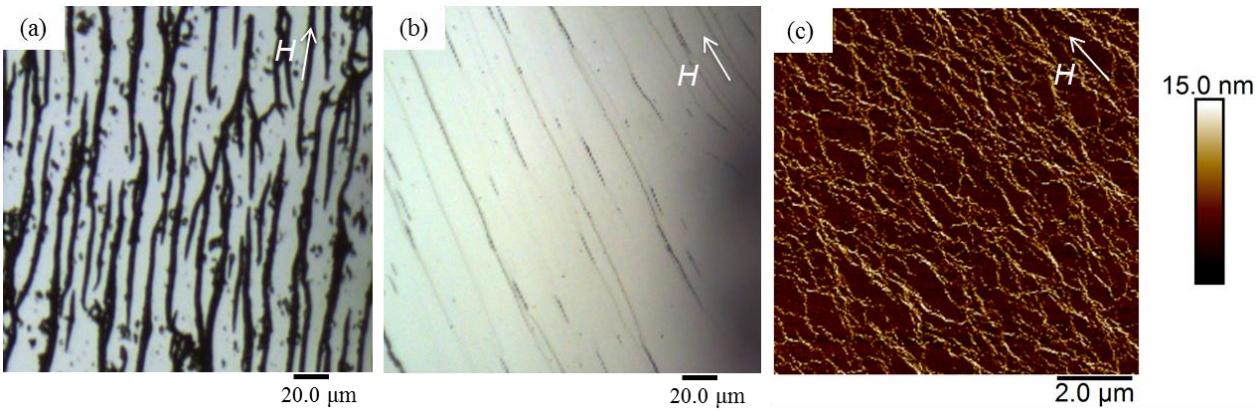

Figure 4.8 Magnetic-field-induced assembly of OA- and TOPO-coated Co NPs at the water-air interface: (a) SFM optical microscope image of 5 mg/mL Co NP dispersion in toluene; (b, c) 1 mg/mL Co NPs dispersion in toluene: SFM optical microscope image (b) and SFM height image (c).The strength of the applied magnetic field is 22 mT and the direction of the magnetic field is indicated by the white arrow.

4.3.2.3 Magnetic-field-induced assembly at ethylene glycol-air interface

Glycol, in comparison with water, has a lower polarity. The static relative dielectric constant for water is 80.10, while it is only 41.40 for ethylene glycol and 31.82 for diethylene glycol.[38] Since the as-synthesized nanoparticles were coated with hydrophobic ligands, like oleic acid, oleylamine or TOPO, it is difficult to achieve a well spreading film on the water surface. Thus, ethylene glycol is more suitable as subphase for assembly of hydrophobic NPs compared with water. Since Majetich's group and Weller's group used ethylene glycol and diethylene glycol as subphase in the Langmuir-Blodgett trough to obtain nanoparticle films,[38,39] the assembly of nanoparticles at glycol-air interface has been widely researched.[40,41] Dong *et al*. found that the solvent evaporation kinetics affected the growth of the film. By using a high boiling-point solvent like toluene led to random assembly of NPs.[40] Thus, in the thesis, ethylene glycol was used as subphase, Co NPs were dispersed in hexane and dropped on the surface. As shown in Figure 4.7, a Teflon well half-filled with ethylene glycol was placed between the two magnets with the distance of 10.5 cm, and the magnetic field was calcuated as 22 mT.[31] Co NPs dispersed in *n*-hexane were carefully dropped onto the liquid surface. The film was formed after the evaporation of hexane. Because of the high boiling-point of ethylene glycol, it is very difficult to evaporate the residual ethylene glycol on substrates after transferring the film. Thus, acetonitrile was carefully added along the wall of the Teflon well, and the film was transferred from ethylene glycol-air interface to acetonitrile-air interface. A large area film was obtained by gently placing the substrates under the floating film, followed by lifting up. The film was allowed to dry in air. Figure 4.9a shows the formation of the film in a Teflon well and Figure 4.9b shows the film after transfer onto a silicon wafer. The assembly behavior of Co NPs with different concentration at ethylene glycol-air interface was investigated. Figure 4.10 shows the 1-D chains of Co NPs assembled under the applied magnetic field when using the lowest concentration (1 mg/mL). These chains were sparsely distributed and flexible compared to the assembly from a higher concentration (2.5 mg/mL) shown in Figure 4.11. Here, the formed 1-D chains were more closely and regular (Figure 4.11a–c). The crack in Figure 4.11c probably resulted from the film transfer or drying process, which can be obviously

observed in Figure 4.9b. 1-D chains of Co NPs superstructures can also be seen from TEM images (Figure 4.11d and e). When the concentration was further increased up to 5 mg/mL, a more continuous film with almost full coverage of Co NPs was obtained (Figure 4.12). A large area of chains can be seen in the SEM image in Figure 4.12d. The formed 1-D chains are straight along the direction of the applied magnetic field (Figure 4.12). Thus, as conclusion from the results, the higher the concentration of the NP dispersion, the straighter are the 1-D chains. However, when the concentration of the Co NPs was less than 1 mg/mL, no chain structure was found. This was probably because the NPs were randomly distributed with a large distance between the individual particles which led to reduced interaction between the particles.[42]

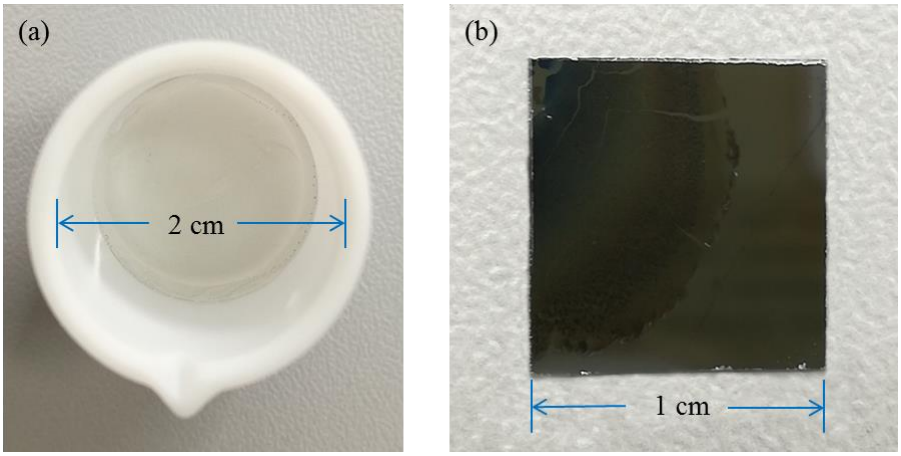

Figure 4.9 Illustration of the assembly of OA- and TOPO-coated Co NP films: (a) the formation of the film at ethylene glycol-air interface in a Teflon well; (b) after transferring the film to a silicon wafer by dipping the silicon wafer under the film, followed by lifting up.

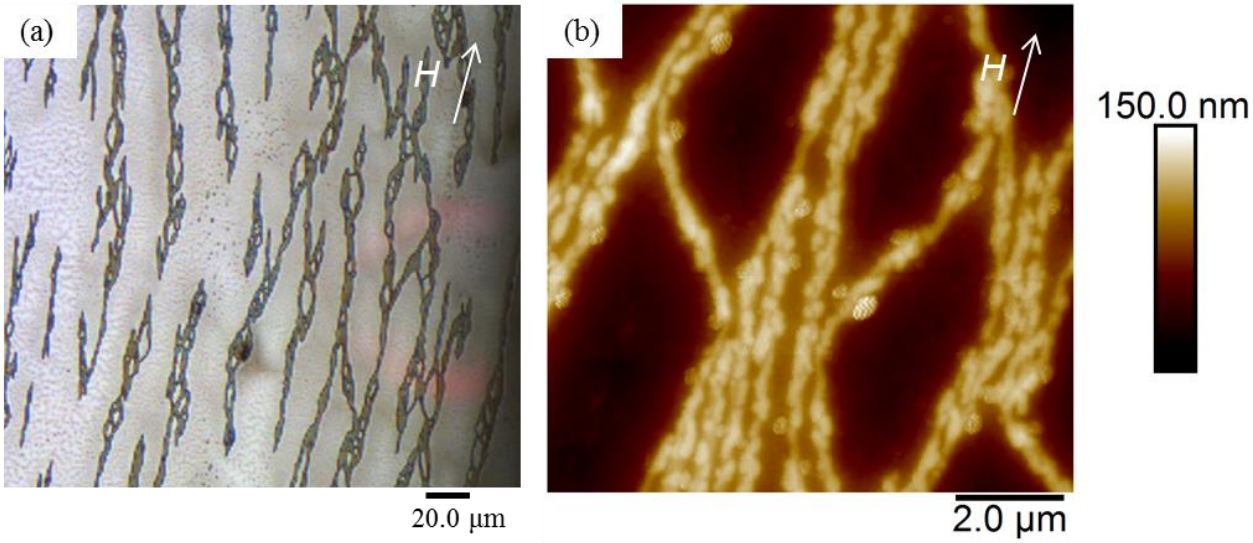

Figure 4.10 Magnetic-field-induced assembly of OA- and TOPO-coated Co NPs (1 mg/mL in hexane) at ethylene glycol-air interface: (a) SFM optical microscope image (the red color in the picture is the scattering from the laser of the SFM); (b) SMF height image. The strength of the applied magnetic field is 22 mT and the direction of the magnetic field is indicated by the white arrow.

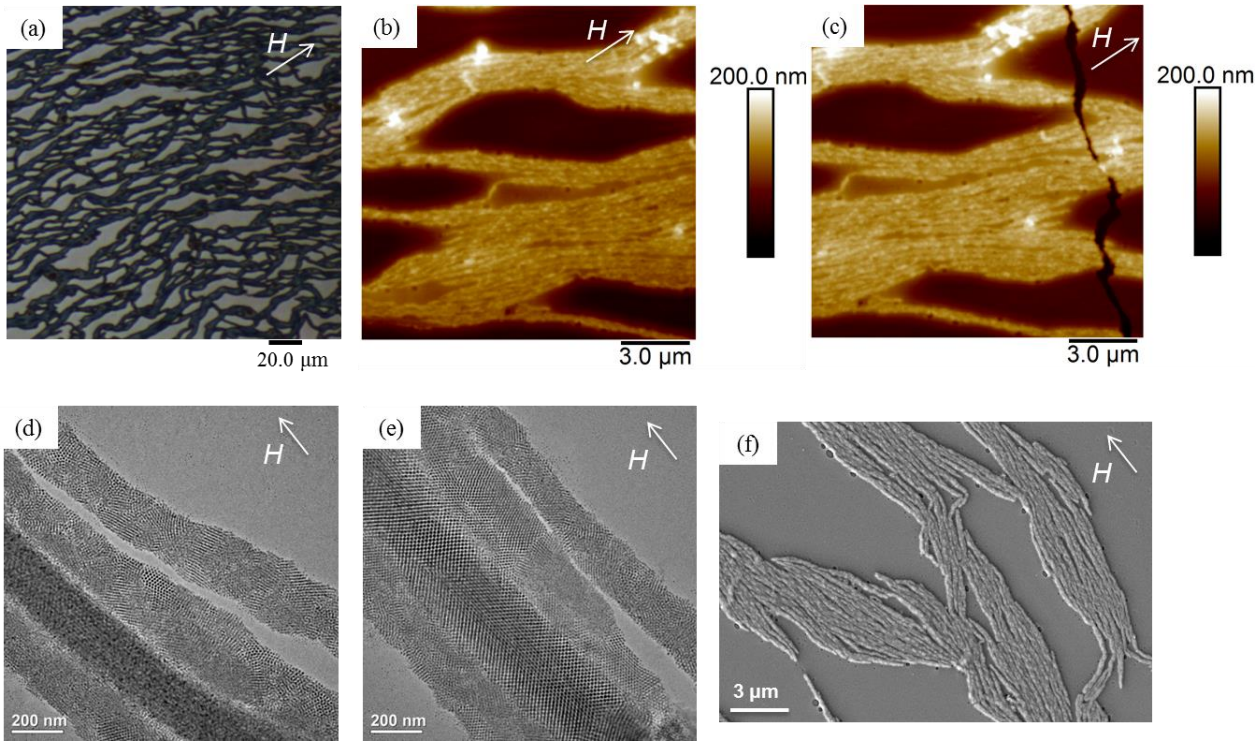

Figure 4.11 Magnetic-field-induced assembly of OA- and TOPO-coated Co NPs (2.5 mg/mL in hexane) at ethylene glycol-air interface: (a) SFM optical microscope image (the red color in the picture is the scattering from the laser of the SFM); (b, c) SFM height images; (d, e) TEM images; (f) SEM image. The strength of the applied magnetic field is 22 mT and the direction of the magnetic field is indicated by the white arrow.

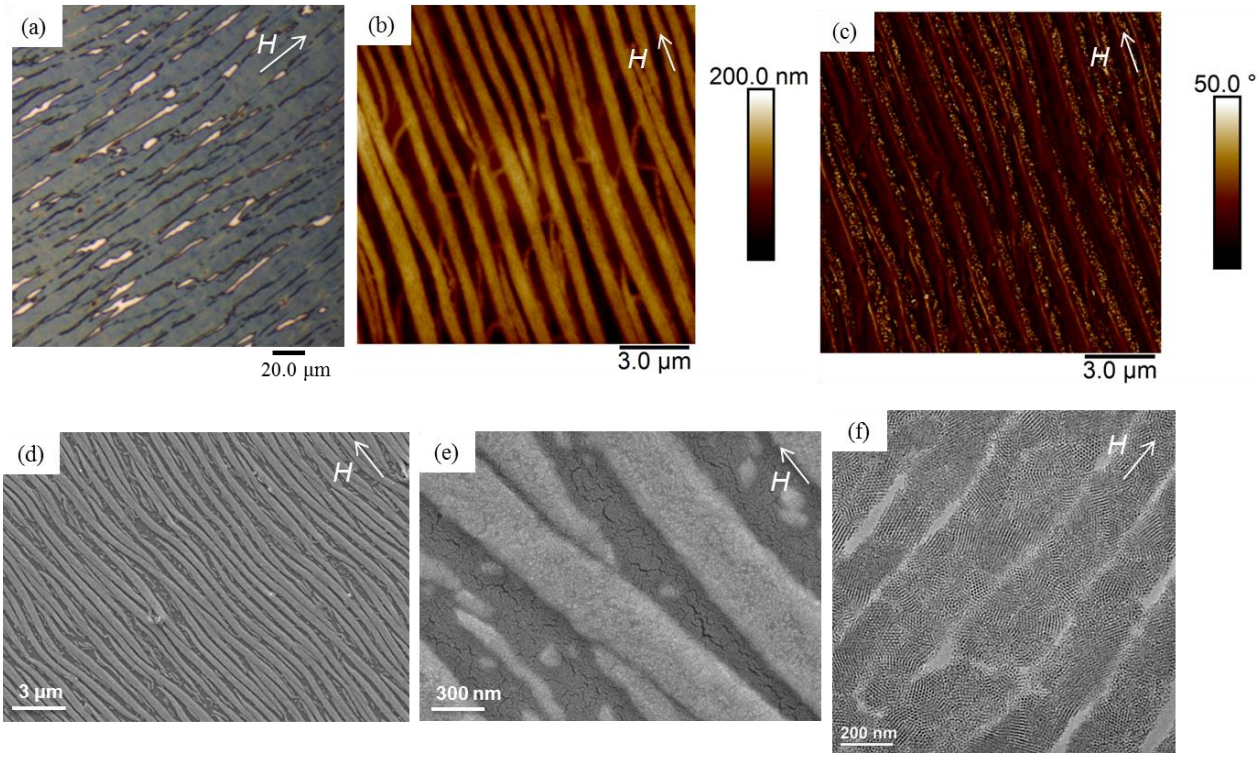

Figure 4.12 Magnetic-field-induced assembly of OA- and TOPO-coated Co NPs (5 mg/mL in hexane) at ethylene glycol-air interface: (a) SFM optical microscope image; (b, c) SFM images: height (b) and phase image (c); (d, e) SEM images at different magnifications; (f) TEM image. The magnetic field strength is 22 mT and the direction of the external magnetic field is indicated by the white arrow.

4.3.3 Effect of strength of magnetic field on the assembly of Co NPs at fixed concentration

When superparamagnetic nanoparticles are exposed to an external applied field, their induced moments tend to align along the field direction. The alignment depends on the competition between magnetic interaction induced by the external magnetic field and the fluctuation caused by Néel rotation or Brownian rotation.[42] Néel rotation can restructure the electronic spins and thus reorient the magnetic moment, and Brownian rotation refers to the rotation of the particle itself in dispersion.[43,44] When the magnetic field is weak, the assembled chains are usually short and flexible due to the fluctuation of the induced moments. When the magnetic field increases, the induced moments of the magnetic nanoparticles become larger, and dominate over the fluctuation. Thus, the formed short chains connect to each other and become longer chains; and thicker chains can be obtained through chain-chain interaction. What's more, the induced moments of the NPs tend to direct into one direction with increased magnetic field, hence the chains are straighter.[42] Thus, the assembly behavior of Co NPs under different strength of the magnetic field was investigated.

4.3.3.1 Magnetic-field-induced assembly on substrates by drop-casting

As illustrated in Figure 4.7, the as-prepared OA- and TOPO-coated Co NPs were dispersed in toluene at a fixed concentration (2.5 mg/mL) and dropped on a silicon wafer. In contrast to the experiments in chapter 4.3.2.1, not the concentration, but the magnetic field strength during the drop-casting was varied. The

distance of the two magnets was adjusted to 21 cm and 6.8 cm, hence, the magnetic field strength was calculated as 4 mT and 54 mT, respectively.[31] Figure 4.13a and b show short and worm-like chains aligned along the weaker magnetic field of 4 mT, which resulted from the fluctuation of the induced moments of these NPs. However, when the magnetic field increased to 54 mT, the chains were long and straight. Thus, the morphology of the NP assemblies can be changed by varying the strength of the magnetic field.

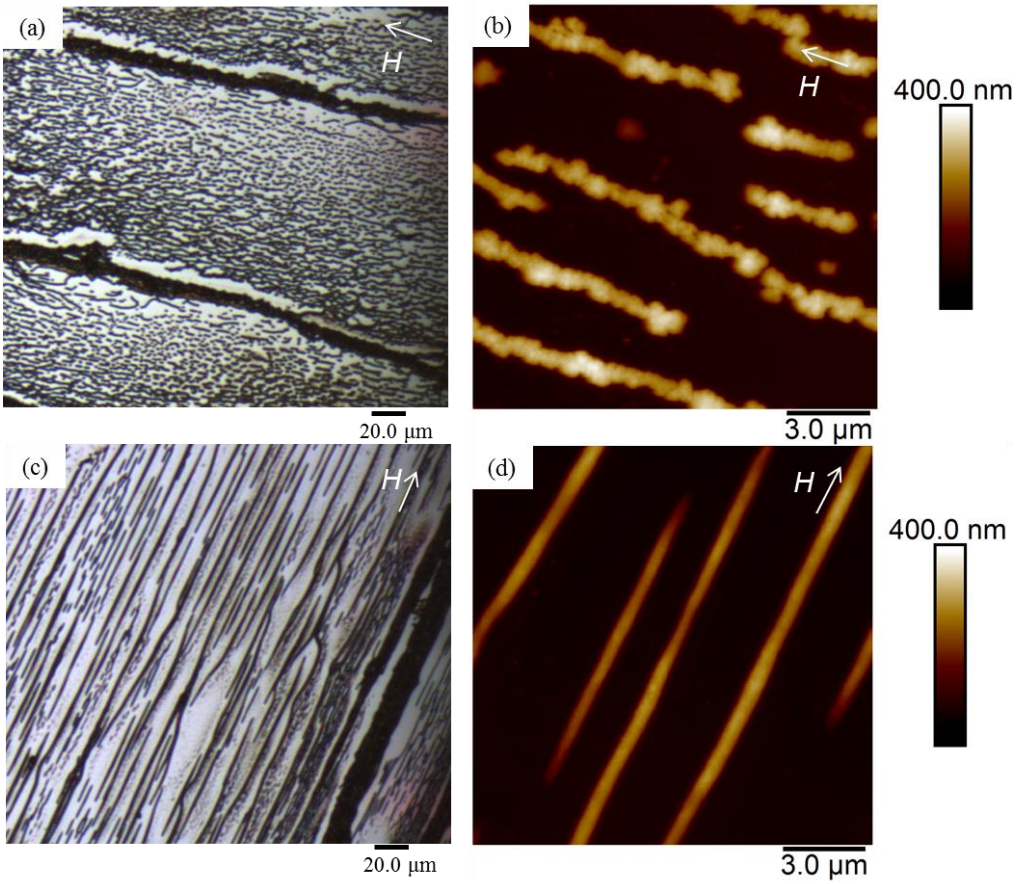

Figure 4.13 Magnetic-field-induced assembly of OA- and TOPO-coated Co NPs (2.5 mg/mL in hexane) by drop casting on a silicon wafer: (a, b) the applied magnetic field strength is 4 mT: SFM optical microscope image (the red color in the picture is the scattering from the laser of the SFM) (a); SFM height image (b); (c, d) the applied magnetic field strength is 54 mT: SFM microscope image (the red color in the picture is the scattering from the laser of the SFM) (c); SFM height image (d). The direction of the external magnetic field is indicated by the white arrow.

4.3.3.2 Magnetic-field-induced assembly at ethylene glycol-air interface

Here, Co NPs were dispersed into hexane at 2.5 mg/mL, dropped on the ethylene glycol surface and transferred to Si-wafers in the same way like before in chapter 4.3.2.3. By changing the distance of the two magnets to 21 cm and 6.8 cm, where the magnetic field was 4 mT and 54 mT, respectively, the assembly behavior changed. Figure 4.14a, b and c show the 1-D chains of Co NPs with weaker magnetic field of 4 mT. These chains were thinner and flexible structures. When the magnetic field strength increased to 54 mT, the formed 1-D chains were thicker and straighter along the direction of the applied magnetic field (Figure 4.14d, e and f). Thus, the stronger magnetic field leads to thicker and straighter 1-D

chains, which was a similar result compared to the assembly by drop casting on substrates under different magnetic field.

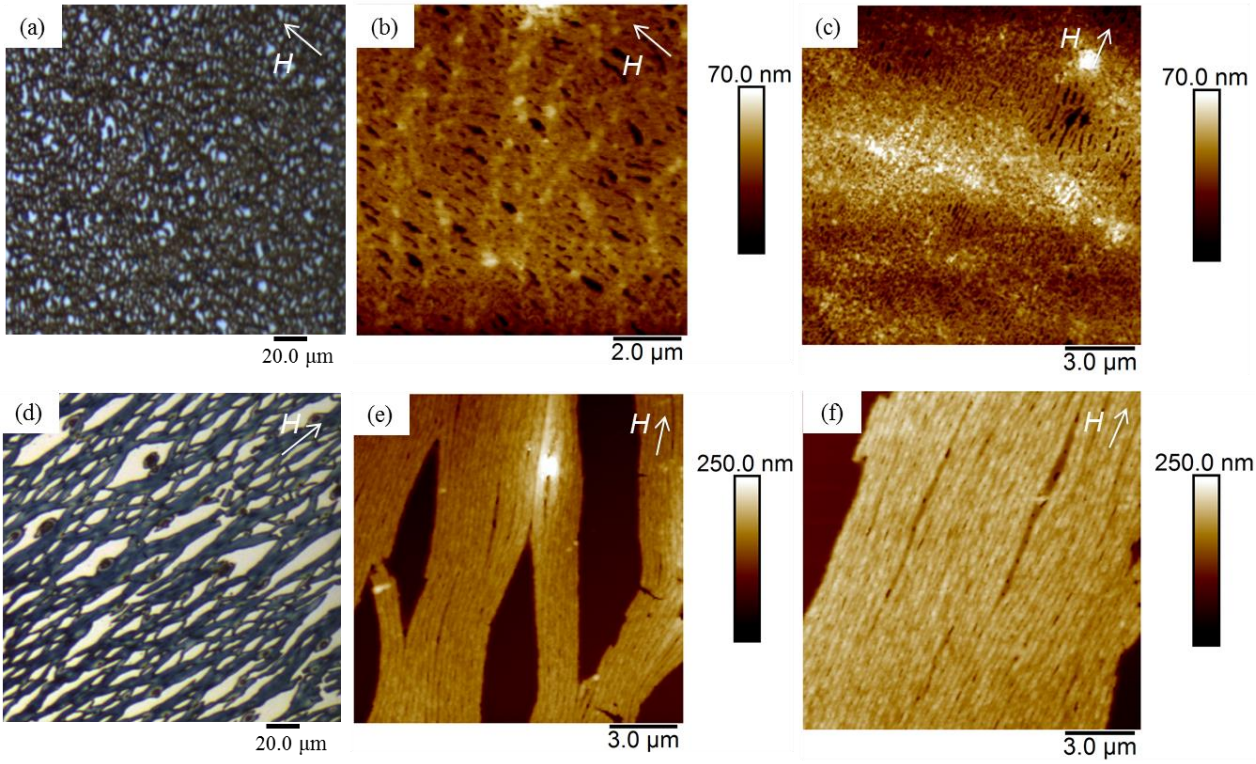

Figure 4.14 Magnetic-field-induced assembly of OA- and TOPO-coated Co NPs (2.5 mg/mL in hexane) at ethylene glycol-air interface: (a–c) the applied magnetic field strength is 4 mT: SFM optical microscope image (a); SMF height images (b and c); (d–f) the applied magnetic field strength is 54 mT: SFM optical microscope image (d); SFM height images (e and f). The direction of the external magnetic field is indicated by the white arrow.

4.4 Conclusions

In summary, monodisperse superparamagnetic OA- and TOPO-coated cobalt nanoparticles were synthesized. Well-defined Co NPs assemblies were formed under an external magnetic field by using various techniques, namely drop-casting on substrates, assembly at water-air interface and at ethylene glycol-air interface. By changing the concentration of the nanoparticle dispersion and the strength of the applied magnetic field, the assemblies exhibited different morphologies. TEM, SEM and SFM showed that the formed 1-D chains were shorter and flexible at either lower concentration of the Co NP dispersion or lower strength of the external magnetic field due to thermal fluctuation. However, by increasing the concentration of the NP dispersion or the strength of the applied magnetic field, these chains became longer, thicker and straighter. The magnetic-field-induced assembly of superparamagnetic nanoparticles provided a powerful approach for potential applications in electronic devices.

4.5 References

1. Corot, C., Robert, P., Idée, J. M. & Port, M. Recent advances in iron oxide nanocrystal technology for medical imaging. *Adv. Drug Deliv. Rev.* **58,** 1471–1504 (2006).

2. de Dios, A. S. & Díaz-García, M. E. Multifunctional nanoparticles: analytical prospects. *Anal. Chim. Acta* **666,** 1–22 (2010).
3. Dobson, J. Magnetic micro- and nano-particle-based targeting for drug and gene delivery. *Nanomedicine* **1,** 31–37 (2006).
4. Frey, N. A., Peng, S., Cheng, K. & Sun, S. Magnetic nanoparticles: synthesis, functionalization, and applications in bioimaging and magnetic energy storage. *Chem. Soc. Rev.* **38,** 2532 (2009).
5. Hütten, A. Applications beyond data storage. *Nat. Mater.* **4,** 725–726 (2005).
6. Mornet, S. *et al.* Magnetic nanoparticle design for medical applications. *Prog. Solid State Chem.* **34,** 237–247 (2006).
7. Mornet, S., Vasseur, S., Grasset, F. & Duguet, E. Magnetic nanoparticle design for medical diagnosis and therapy. *Forunal Mater. Chem.* **14,** 2161–2175 (2004).
8. Timonen, J. V. I., Latikka, M., Leibler, L., Ras, R. H. A. & Ikkala, O. Switchable static and dynamic self-assembly of magnetic droplets on superhydrophobic surfaces. *Science.* **341,** 253–257 (2013).
9. Cho, M. H. *et al.* A magnetic switch for the control of cell death signalling in in vitro and in vivo systems. *Nat. Mater.* **11,** 1038–1043 (2012).
10. Jeong, U., Teng, X., Wang, Y., Yang, H. & Xia, Y. Superparamagnetic colloids: controlled synthesis and niche applications. *Adv. Mater.* **19,** 33–60 (2007).
11. Sun, S. H. Recent advances in chemical synthesis, self-assembly, and applications of FePt nanoparticles. *Adv. Mater.* **18,** 393–403 (2006).
12. Rebolledo, A. F. *et al.* Signatures of clustering in superparamagnetic colloidal nanocomposites of an inorganic and hybrid nature. *Small* **4,** 254–261 (2008).
13. Ge, J., He, L., Hu, Y. & Yin, Y. Magnetically induced colloidal assembly into field-responsive photonic structures. *Nanoscale* **3,** 177–183 (2011).
14. Wang, M., He, L. & Yin, Y. Magnetic field guided colloidal assembly. *Materials Today* **16,** 110–116 (2013).
15. Jones, T. B. *Electromechanics of Particles*. (Cambridge University Press, 1995).
16. Kraftmakher, Y. Magnetic field of a dipole and the dipole-dipole interaction. *Eur. J. Phys.* **28,** 409–414 (2007).
17. Ngo, A. T. & Pileni, M. P. Assemblies of ferrite nanocrystals: partial orientation of the easy magnetic axes. *J. Phys. Chem. B* 53–58 (2001).
18. Ngo, A. T. & Pileni, M. P. Cigar-shaped ferrite nanocrystals: orientation of the easy magnetic axes. *J. Appl. Phys.* **92,** 4649–4652 (2002).
19. Pileni, M. P. Nanocrystal self-assemblies: fabrication and collective properties. *J. Phys. Chem. B* **105,** 3358–3371 (2001).
20. Sahoo, Y. *et al.* Field-directed self-assembly of magnetic nanoparticles. *J. Phys. Chem. B* 3380–3383 (2004).
21. Singamaneni, S., Bliznyuk, V. N., Binek, C. & Tsymbal, E. Y. Magnetic nanoparticles: recent

advances in synthesis, self-assembly and applications. *J. Mater. Chem.* **21,** 16819 (2011).

22. Wiedwald, U., Spasova, M., Farle, M., Hilgendorff, M. & Giersig, M. Ferromagnetic resonance of monodisperse Co particles. *J. Vac. Sci. Technol. A Vacuum, Surfaces, Film.* **19,** 1773–1776 (2001).
23. Park, J.-I., Jun, Y.-W., Choi, J.-S. & Cheon, J. Highly crystalline anisotropic superstructures via magnetic field induced nanoparticle assembly. *Chem. Commun.* **1,** 5001–5003 (2007).
24. Reiss, G. & Hütten, A. Magnetic nanoparticles: applications beyond data storage. *Nat. Mater.* **4,** 725–726 (2005).
25. Sun, S., Murray, C. B., Weller, D., Folks, L. & Moser, A. Monodisperse FePt nanoparticles and ferromagnetic FePt nanocrystal superlattices. *Science.* **287,** 4–5 (2009).
26. Irvine, U. Cleaning procedures for silicon wafers. *Fabrication* 2–5 (2010).
27. Puntes, V. F., Zanchet, D., Erdonmez, C. K. & Alivisatos, A. P. Synthesis of hcp-Co nanodisks. *J. Am. Chem. Soc.* **124,** 12874–12880 (2002).
28. Erb, R. M., Sebba, D. S., Lazarides, A. A. & Yellen, B. B. Magnetic field induced concentration gradients in magnetic nanoparticle suspensions: theory and experiment. *J. Appl. Phys.* **103,** (2008).
29. Erb, R. M. & Yellen, B. B. Concentration gradients in mixed magnetic and nonmagnetic colloidal suspensions. *J. Appl. Phys.* **103,** 2006–2009 (2008).
30. Sacanna, S. & Philipse, A. P. Preparation and properties of monodisperse latex spheres with controlled magnetic moment for field-induced colloidal crystallization and (dipolar) chain formation. *Langmuir* **22,** 10209–10216 (2006).
31. https://www.supermagnete.de/eng/faq/How-do-you-calculate-the-magnetic-flux-density.
32. Weis, J. J. Low density quasi-two-dimensional dipolar hard spheres in an external field. *Mol. Phys.* **103,** 7–10 (2005).
33. Satoh, A., Chantrell, R. W., Kamiyama, S. I. & Coverdale, G. N. Three dimensional Monte Carlo simulations of thick chainlike clusters composed of ferromagnetic fine particles. *J. Colloid Interface Sci.* **181,** 422–428 (1996).
34. Nie, H. L., Dou, X., Tang, Z., Jang, H. D. & Huang, J. High-yield spreading of water-miscible solvents on water for Langmuir-Blodgett assembly. *J. Am. Chem. Soc.* **137,** 10683–10688 (2015).
35. Tanaka, H., Mitsuishi, M. & Miyashita, T. Tailored-control of gold nanoparticle adsorption onto polymer nanosheets. *Langmuir.* **19.** 3103–3105 (2003).
36. Tao, A. R., Huang, J. & Yang, P. Langmuir-Blodgettry of nanocrystals and nanowires. *Acc. Chem. Res.* **41,** 1662–1673 (2008).
37. Zhao, L., Byun, M., Rzayev, J. & Lin, Z. Polystyrene-polylactide bottlebrush block copolymer at the air/water interface. *Macromolecules* **42,** 9027–9033 (2009).
38. Aleksandrovic, V. *et al.* Preparation and electrical properties of cobalt-platinum nanoparticle monolayers deposited by the Langmuir-Blodgett technique. *ACS Nano* **2,** 1123–1130 (2008).
39. Sachan, M., Walrath, N. D., Majetich, S. A., Krycka, K. & Kao, C. C. Interaction effects within Langmuir layers and three-dimensional arrays of ε-Co nanoparticles. *J. Appl. Phys.* **99,** 8–11 (2006).

40. Dong, A., Chen, J., Vora, P. M., Kikkawa, J. M. & Murray, C. B. Binary nanocrystal superlattice membranes self-assembled at the liquid-air interface. *Nature* **466,** 474–477 (2010).
41. Ye, X. *et al.* Shape alloys of nanorods and nanospheres from self-assembly. *Nano Lett.* **13,** 4980–4988 (2013).
42. Mousavi, N. S. S., Khapli, S. D. & Kumar, S. Direct observations of field-induced assemblies in magnetite ferrofluids. *J. Appl. Phys.* **117,** 1–9 (2015).
43. Shah, S. A., Reeves, D. B., Ferguson, R. M., Weaver, J. B. & Krishnan, K. M. Mixed Brownian alignment and Néel rotations in superparamagnetic iron oxide nanoparticle suspensions driven by an ac field. *Phys. Rev. B - Condens. Matter Mater. Phys.* **92,** 1–11 (2015).
44. Kopčanský, P. *et al.* Néel and Brownian rotations in ferronematics. *Physics Procedia* **9,** 82–86 (2010).

5 Synthesis of Polystyrene-Coated Superparamagnetic and Ferromagntic Cobalt Nanoparticles

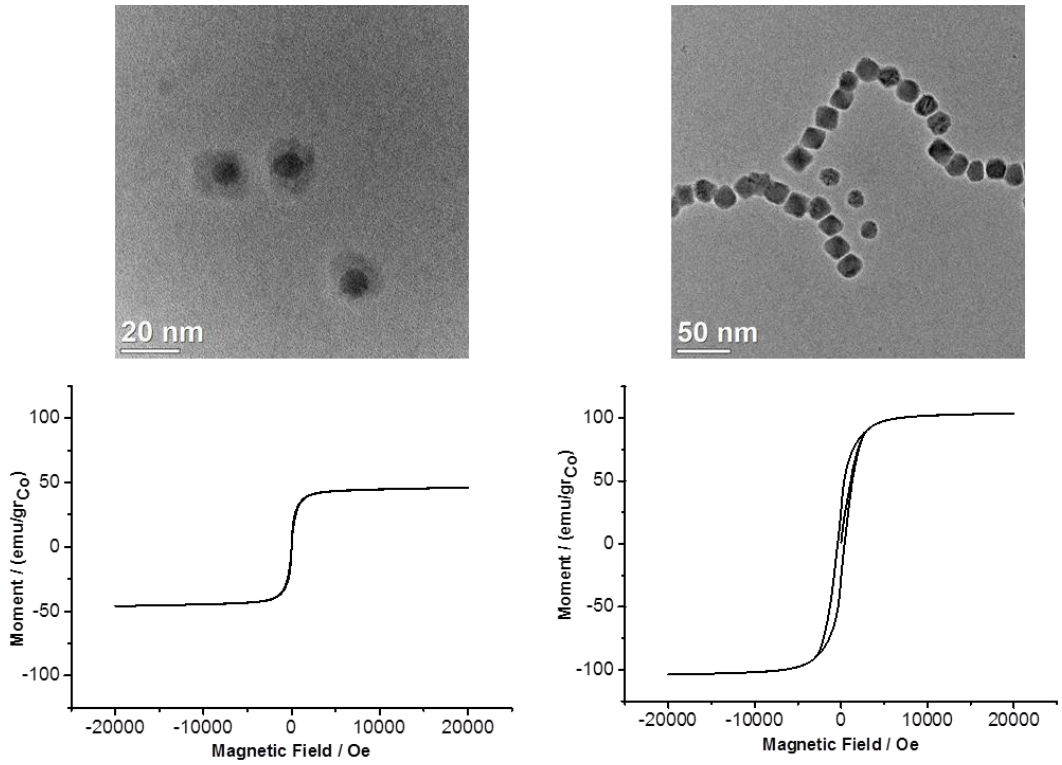

In this chapter, polystyrene-coated cobalt nanoparticles were synthesized through a dual-stage thermolysis of cobalt carbonyl ($Co_2(CO)_8$). The amine end-functionalized polystyrene surfactants with varying molecular weight were prepared via atom-transfer radical polymerization technique. By changing the concentration of these surfactants, Co NPs with different size, size distribution and magnetic properties were obtained. Transmission electron microscopy characterization showed that the size of cobalt nanoparticles stabilized with lower molecular weight polystyrene surfactants varied from 12–22 nm, while the size of Co NPs coated with polystyrene of middle and higher molecular weight showed little change around 20 nm. Magnetic measurements revealed that the small cobalt particles were superparamagnetic, while larger particles were ferromagnetic and self-assembled into 1-D chain structures. Thermogravimetric analysis revealed that the grafting density of polystyrene with lower molecular weight is higher than those with higher molecular weight. To the best of our knowledge, this is the first time to obtain both superparamagnetic and ferromagnetic Co NPs by changing the molecular weight and concentration of polystyrene through dual-stage decomposition method.

5.1 Introduction

Due to a variety of applications in biological imaging, therapeutic applications and magnetic energy storage,[1–4] the preparation of magnetic nanoparticles has been widely investigated. Decomposition of

metallic precursors at high temperature is a general method to synthesize well-defined magnetic nanoparticles. Up to now, both small molecules and polymers have been used as surfactants to prepare superparamagnetic and ferromagnetic nanoparticles.[5,6,15–20,7–14] However, the polymeric surfactants provide stronger repulsive force to stabilize magnetic nanoparticles against agglomeration than small molecules; thus, numerous studies about the preparation of polymer-coated magnetic nanoparticles have been reported.[6,9–12,17,20] For example, magnetic iron nanoparticles were prepared by Smith's group with vinyl polymers as surfactants through thermolysis of $Fe(CO)_5$.[20] However, due to the rapid oxidation, which led to a great reduction of magnetic moments, more attention was paid to the preparation of iron oxide nanoparticles and cobalt nanoparticles.[6,9,11,12,17] Many applications of magnetic NPs are attributed to their magnetic properties. The saturation magnetization of cobalt bulk material is 161 emu/g, which is higher than that of magnetite (Fe_3O_4) (92 emu/g),[21] thus, the investigation of cobalt nanoparticles is of great importance.

The size of magnetic nanoparticles plays an important role for their magnetic properties. Generally, ferromagnetic NPs are larger than superparamagnetic NPs. The magnetic properties of ferromagnetic NPs are dominated by a hysteresis loop exhibiting remanence and coercivity. Ferromagnetic NPs can self-assemble into one-dimensional (1-D) chain structures due to dipolar interaction.[12,22] When the size of ferromagnetic NPs is reduced below a critical value, the particles become superparamagnetic,[23] exhibiting no residual magnetization after removal of the external magnetic field. Thus, the control of the size of magnetic NPs is essential. In the preparation of magnetic NPs through the thermal decomposition of metal precursors, two steps are involved in the process: the formation of nucleation nanocrystals by decomposition of metal precursor at high temperature, followed by the growth of the nuclei. Therefore, many parameters can affect the size and morphology of magnetic NPs, including temperature, surfactants (composition, molecular weight and concentration), reaction time, solvent, etc. Up to now, some efforts have been made to control the size and morphology of Co NPs.[20,24–26] For example, Pyun's group synthesized magnetic Co NPs by using different end-functional polystyrene surfactants through thermal decomposition of cobalt carbonyl ($Co_2(CO)_8$).[24–26] By varying the reaction temperature, ferromagnetic Co NPs with different sizes ranging from 18 nm to 43 nm were obtained.[26] Different morphologies of Co NPs were observed when using different molecular weight of polystyrene.[24] However, the preparation of both ferromagnetic and superparamagnetic Co NPs by using polystyrene surfactant has never been reported. Herein, ferromagnetic and superparamagnetic Co NPs were synthesized by varying the concentration and molecular weight of amine end-functionalized polystyrene via dual-stage thermolysis of $Co_2(CO)_5$. In addition, we studied the influence of the polymers' molecular weight on the grafting density of the hybrid particles in detail.

5.2 Experimental Section

5.2.1 Materials

N-hexane (95%), THF (99.9%), dichloromethane were purchased from Th. Geyer; methanol, acetonitrile (HPLC-grade) were purchased from VWR, *N,N*-dimethylformamide (DMF, 99%) was purchased from Acros Organics; anhydrous 1,2-dichlorobenzene (DCB, 99%), methanol (HPLC-grade), cobalt carbonyl $Co_2(CO)_8$ containing 1-5% *n*-hexane as stabilizer, hydrazine monohydrate (N_2H_2 64 - 65%), 2,2′-bipyridyl (99%), styrene (99%), α,α′-dichloro-p-xylene (98%), 18-crown-16 (99%), phthalimide potassium salt (99%), copper(I) chloride (97%) and alumina (activated, neutral, Brockmann Activity I) were purchased from Sigma Aldrich and used as received without further purification. Copper(I) chloride was purified by stirring in glacial acetic acid overnight, washed with ethanol and dried under vacuum. $Co_2(CO)_8$ was kept in the fridge of a glovebox, and *n*-hexane evaporated in the glovebox before use. Styrene was passed through a short column of neutral alumina to remove inhibitors and deoxygenated by bubbling with N_2 before starting a polymerization.

5.2.2 Synthesis of amine end-functionalized polystyrene (PS-NH_2)

Synthesis of 4-(chloromethyl)benzyl phthalimide **2**

The synthesis of compound **2** was performed according to the literature.[25] In detail, in a 150 mL round-bottom flask, α,α′-dichloro-p-xylene (6.59 g, 376 mmol), phthalimide potassium salt (2.67g, 144 mmol) and 18-crown-6 (380 mg, 1.43 mmol) were dissolved in 75 mL acetonitrile. The reaction was refluxed overnight under the protection of N_2. After the reaction mixture cooled down to room temperature, the solvent was evaporated under vacuum. The resulting crude product was purified by column chromatography on silica gel (CH_2Cl_2:hexane = 5:1), giving a white crystalline solid **2** (2.0 g, 49 % yield). ^{1}H-NMR (400 MHz, $CDCl_3$): δ = 7.85 (m, Ar-H, 2H), 7.71 (m, Ar-H, 2H), 7.45-7.40 (m, Ar-H, 2H), 7.36–7.31 (m, Ar-H, 2H), 4.84 (s, CH_2, 2H), 4.54 (s, CH_2, 2H).

Synthesis of benzyl phthalimide end-functionalized polystyrene **3**

In a 100 mL Schlenk flask, compound **2** (500 mg, 1.75 mmol), 2,2′-bipyridyl (546 mg, 3.5 mmol) and CuCl (173 mg, 1.75 mmol) were added. The flask was sealed with a rubber septum, evacuated and back-filled with N_2 for three cycles. 2 mL degassed DMF was injected, followed by the addition of degassed styrene (24 mL, 210 mmol). The flask was placed into an oil bath at 110°C for 16 h. After cooling down to room temperature, the flask was opened to air. The reaction mixture was diluted with 300 mL dichloromethane, and passed through a neutral alumina plug to remove the copper catalyst. The collected solution was concentrated under vacuum and precipitated into 1 L methanol twice. The resulting white powder was dried in vacuum. ^{1}H-NMR (400 MHz, $CDCl_3$): δ = 7.82 (b, Ar-H, 2H), 7.68 (b, Ar-H, 2H), 7.2–6.3 (m, Ar-H), 4.77 (m, CH_2, 2H), 2.4-1.2 (m, CH + CH_2). $Mn_{,GPC}$ *=4500 g/mol; Mw/Mn = 1.28*.

To synthesize benzyl phthalimide end-functionalized polystyrene of different molecular weight, the procedure was conducted the same, only by changing the amount of monomer styrene and the reaction time. 12 mL styrene (105 mmol) and 14 h reaction time resulted in a polymer of *Mn =2300 g/mol;*

Mw/Mn = 1.38. Similarly, 24 mL styrene (105 mmol) and 41 h resulted in a polymer of *Mn =10500 g/mol; Mw/Mn = 1.17*.

Synthesis of amine end-functionalized polystyrene **4 (PS-NH_2)**

In a 100 mL round-bottom flask, benzyl phthalimide end-functionalized polystyrene (1.8 g, 0.4 mmol) was dissolved in 30 mL THF. 3 mL methanol was added dropwise, and hydrazine monohydrate (640 mg, 12.8 mmol) was slowly dropped. The reaction mixture was allowed to stir at room temperature overnight until a white precipitate was observed. The reaction mixture was concentrated and redissolved in dichloromethane, followed by the precipitation in 1L methanol twice. The resulting white powder was dried under vacuum. ^{1}H-NMR (400 MHz, $CDCl_3$): δ = 8.5 (s, NH_2, 2H), 7.2–6.3 (m, Ar-H), 3.9 (m, CH_2, 2H), 2.4–1.1 (m, CH + CH_2).

The other amine end-functionalized polystyrenes with different molecular weight were prepared by the same procedure.

5.2.3 Synthesis of PS-Co NPs with amine end-functionalized polystyrene as surfactant

For the synthesis of PS-Co NPs, PS-NH_2 of different molecular weight and concentration were used. Typically, in a clean and dried 100 mL three-neck round bottom flask, PS-NH_2 (Mn=4500 g/mol, 225 mg, 0.5 mmol) was added. The flask was then equipped with a condenser, and placed in an oil bath. The whole system was evacuated and back-filled with N_2 three cycles. Degassed 1,2-dichlorobenzene (18 mL) was injected, and the solution was heated to 175 °C. 150 mg $Co_2(CO)_8$ in 2 mL of DCB was rapidly injected at the reflux temperature. After 10 min, the temperature was lowered to 160 °C and the solution was stirred for another 30 min. The reaction mixture was cooled to room temperature under N_2 atmosphere, then, the suspension was collected with a syringe, and transferred into a Schlenk tube which was deoxygenated beforehand and stored in the fridge. To purify the nanoparticles, they were precipitated in *n*-hexane, and centrifuged to remove the supernatant. The particle size was determined by TEM though ImageJ software.

5.2.4 Instruments

Transmission electron microscopy (TEM) images were obtained by using a Titan 80-300 microscope (FEI) operated at 300 kV. The samples were prepared by drop-casting a NP suspension onto the carbon-coated copper grid, followed by drying in air. The size of PS-Co NPs was estimated by ImageJ software.

Thermogravimetric analyses (TGA) were conducted on a TA Instruments Q500. All samples were measured from 25 °C to 800 °C under a nitrogen atmosphere with a heating rate of 10 °C/min.

Wide angle X-ray scattering (WAXS) measurements were done by means of a Bruker-AXS texture goniometer (D5000 equipped with a closed Eulerian Cradle) in reflection technique. Ni-filtered Cu-Kα radiation operated at 30 mA and 40 kV was applied. Scattering intensities were recorded in the 2θ-range from 40° to 55° with a scan speed of 55 s / step and with a step size $\Delta\theta$ of 0.015° (total measurement time: 15 h 17 min). The samples were prepared as powder samples (manually in a mortar) and then put in an appropriate sample holder.

The magnetic properties of Co NPs were measured using a SQUID magnetometer (MPMS 3, by Quantum Design) at the Quantum Materials Core Lab at the Helmholtz Zentrum Berlin by Dr. Konrad Siemensmeyer. The magnetic behavior of Co NPs was measured in field cooling (FC) and zero-field cooling (ZFC) modes from 5 K to 390 K under an applied field of 50 mTesla. Magnetization curves were obtained under the fields from 0–2 Tesla. The magnetic data were normalized from the sample mass of Co atoms.

Polymer number-average molecular weight (Mn ,GPC), weight-average molecular weight (Mw ,GPC), and molecular weight distribution (also polydispersity index, PDI) were determined by gel permeation chromatography (GPC) using DMF with LiBr (1 mg/mL) as eluent, a flow rate of 1.0 mL/min, a high pressure liquid chromatography pump (Spectra Systems P 1000), and a refractometer SEC-3010 (WGE Dr. Bures) detector. Calibration was achieved using polystyrene standards. Results were evaluated using Parsec 5.62 (Brookhaven Instruments) software.

Matrix-assisted laser desorption/ionization time-of-flight (MALDI-ToF) mass spectra were collected on a 337 nm Bruker microflex spectrometer with pulsed ion extraction. The masses were determined in positive ion linear mode. The sample solutions were applied on a ground steel target using the dried droplet technique. THF was used as solvent for PS (5 mg/ml), matrix dithranol (10 mg/mL), and sodium trifluoroacetate (13.6 mg/mL). Sample, matrix and salt solutions were mixed in 5:20:1 ratio and 2 µl of the mixture applied on the target.

Proton nuclear magnetic resonance (^{1}H-NMR) spectra were measured on a Bruker DPX-400 spectrometer at 400 MHz. All samples were prepared in deuterated chloroform ($CDCl_3$, 99.8%). All spectra were referenced to the signal of non-deuterated solvent molecules relative to tetramethylsilane = 0 ppm.

5.3 Results and Discussion

5.3.1 Synthesis and characterization of PS-NH_2

In design of a functional polymer for Co NPs, the binding properties to the NP surface should be taken into consideration. It has been proven that surfactants with functional groups -COOH, -NH_2 and -PO have strong affinity to the surface of cobalt, since N, O and P can donate the lone-pair electrons to the empty d-orbitals of the Co atoms.[19] ATRP is the most widely used controlled radical polymerization.[27–30] The molecular weight, molecular weight distribution, as well as the functionality can be precisely controlled via ATRP technique.[31,32] Furthermore, ATRP can be conducted in a variety of solvents, including water, organic solvent or the mixture thereof, which explains the great potential for biological applications, such as drug delivery, medical imaging, etc.[33] In this study, polystyrene containing a terminal amine group providing anchors for binding to the surface of Co NPs was prepared by using the ATRP technique, similar to the report by Pyun's group.[25] It was aimed at synthesizing polymers of different molecular weight by varying the amount of monomer and the reaction time. Thus, amine end-functionalized polystyrene (PS-NH_2) with three different molecular weight (number average, *Mn*) of 2300 g/mol, 4500 g/mol and 10500 g/mol were synthesized, as shown in Figure 5.4. Relatively broad molecular weight

distribution (Mw/Mn = 1.38) was observed in PS-NH_2 with low molecular weight of 2300 g/mol, while, a narrower molecular weight distribution of PS-NH_2 (Mw/Mn = 1.28) was obtained in PS-NH_2 with higher molecular weight of 4500 g/mol. However, the narrowest molecular weight distribution (Mw/Mn = 1.17) was obtained in polystyrene with the highest molecular weight of 10500 g/mol. The synthesis process of PS-NH_2 is shown in Scheme 5.1, which is known as the Gabriel synthesis. Specifically, the primary chloride group in compound **1** reacted with potassium phthalimide to give compound **2**. Polymerization of styrene in DMF was initiated by **2**, followed by hydrolysis of phthalimide to give amine end-functionalized polystyrene **4**.[34] ^{1}H-NMR spectra of the intermediate compounds and the final polymer are shown in Figure 5.1–5.3.

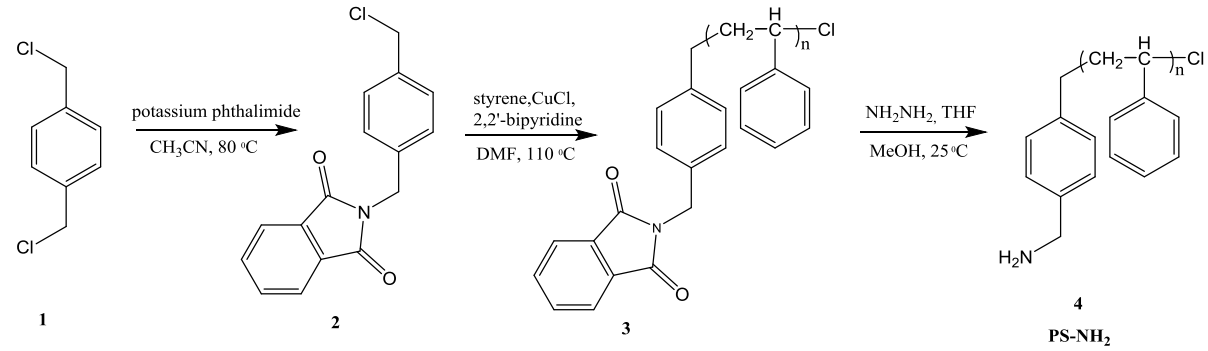

Scheme 5.1 Synthesis route for amine end-functionalized PS-NH_2.

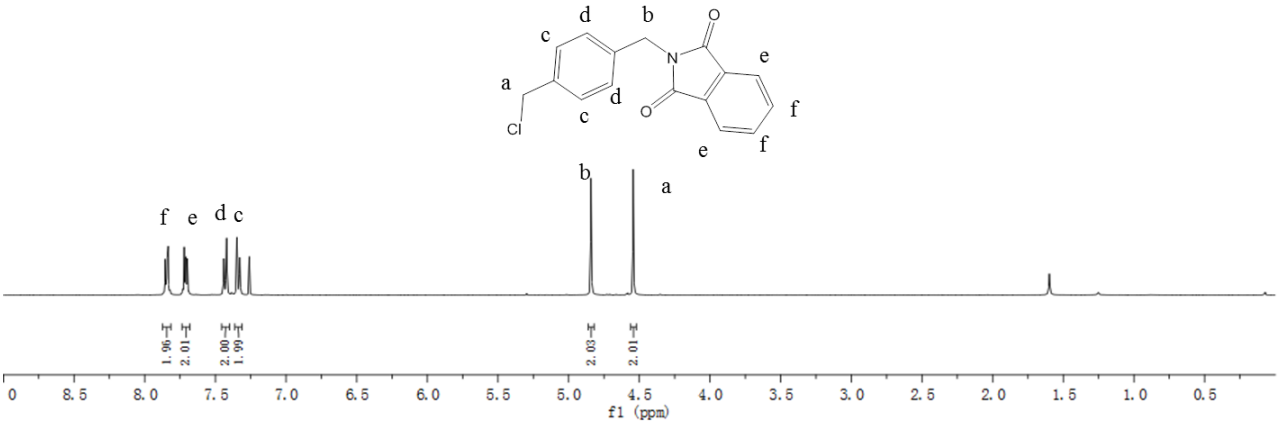

Figure 5.1 ^{1}H-NMR spectrum of **2** in $CDCl_3$.

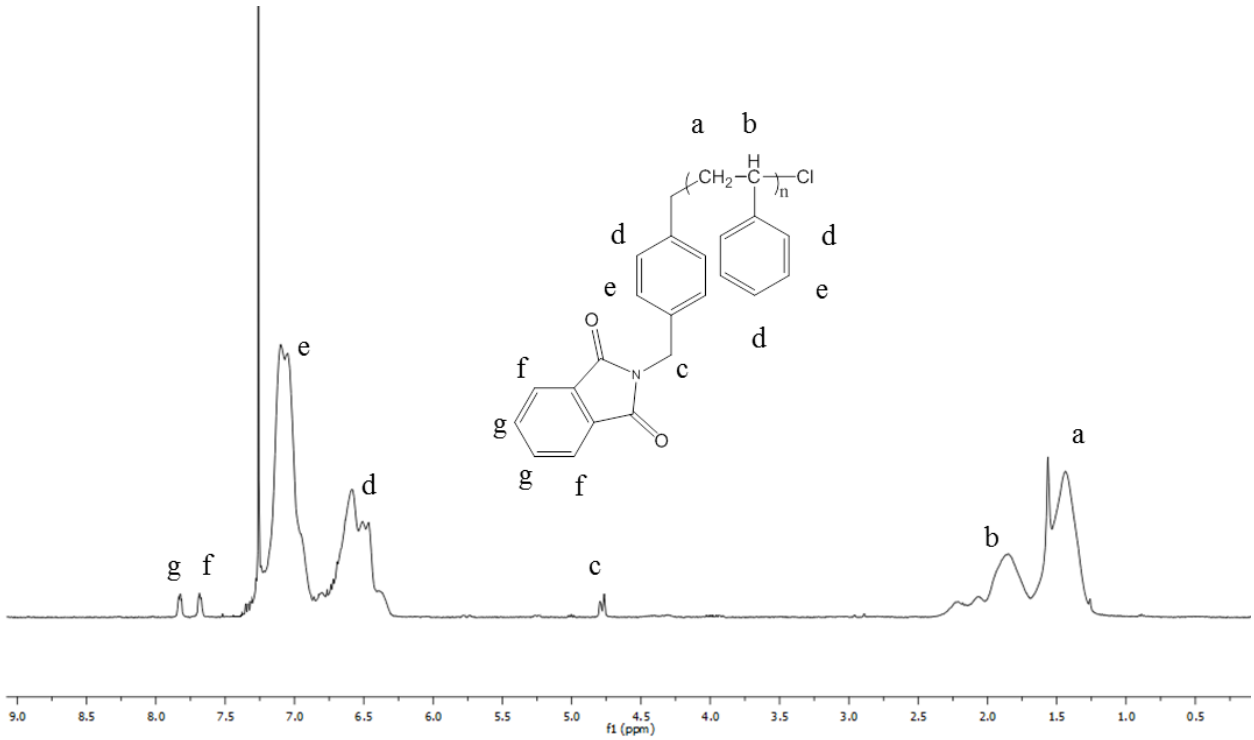

Figure 5.2 ^{1}H-NMR spectrum of **3** (Mn = 4500 g/mol) in $CDCl_3$.

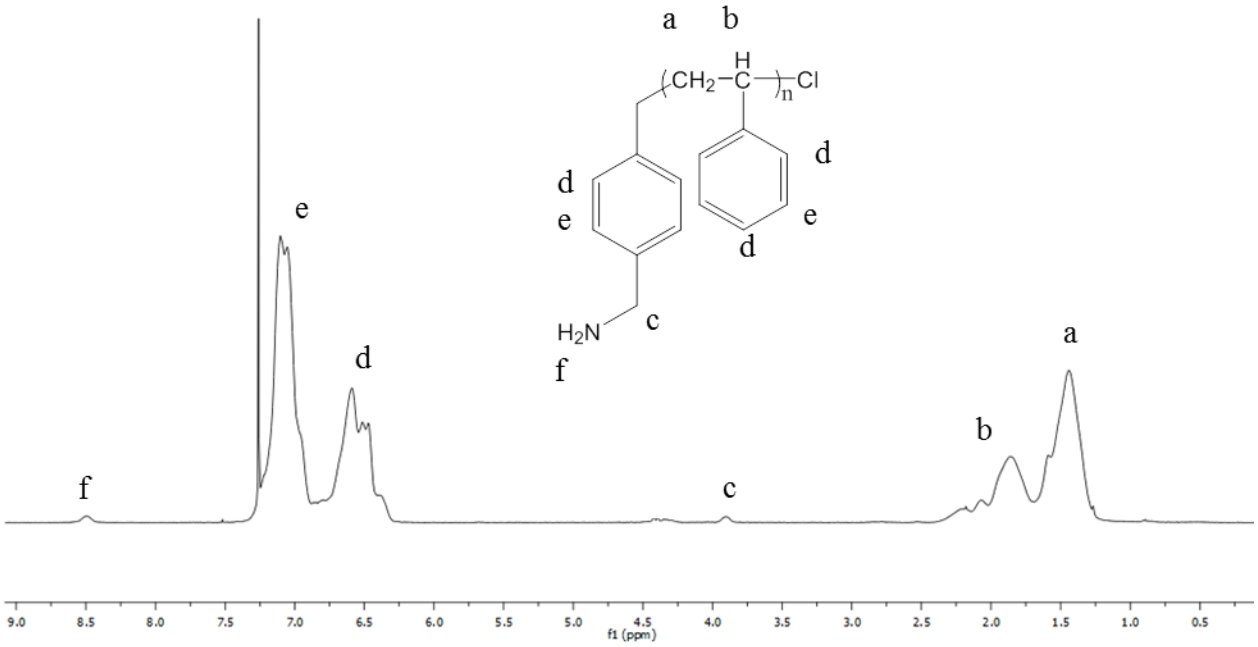

Figure 5.3 ^{1}H-NMR spectrum of **4** (Mn = 4500 g/mol) in $CDCl_3$.

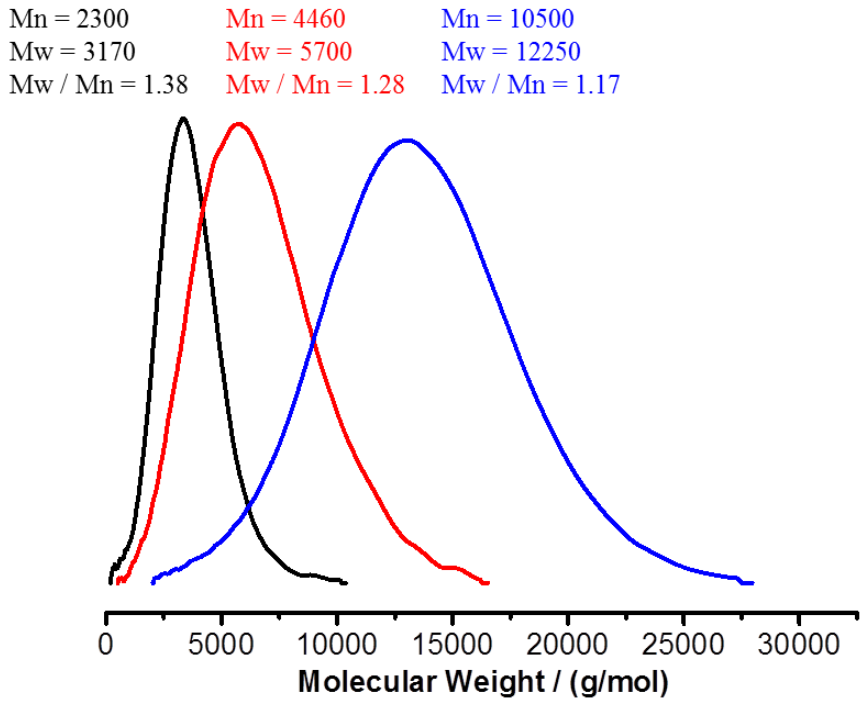

Figure 5.4 GPC curves of PS-NH_2 with different molecular weight.

5.3.2 Synthesis and characterization of PS-CoNPs

Pyun's group reported that ferromagnetic PS-Co NPs with the of around 21 nm were obtained by using PS-NH2 as surfactant via dual-stage thermolysis of cobalt carbonyl in 1,2-dichlorobenzene.25 It is well known that surfactants play an important role in the growth of Co NPs, and thus affect the size of Co NPs. Here, PS-Co NPs of different sizes were prepared by using the same method only by changing the molecular weight and concentration of PS-NH2 surfactants. The size and morphology of PS-Co NPs was characterized by TEM. Figure 5.5, Figure 5.6 and Figure 5.7 show the size distribution and morphology of the as-prepared PS-Co NPs by varying the synthesis parameters with different molecular weight and concentration of PS-NH2, as well as different concentration of cobalt carbonyl. Figure 5.8a presents the tabular overview of the size and size distribution of all prepared nanoparticles, the mean size and standard deviation were obtained from a statistic of around 200 NPs using ImageJ software fitting the clearly analyzable particles. Some images show aggregated ill-shaped particles, which are very difficult to measure, and thus couldn't be taken into account. Therefore, the standard deviation could be slightly underestimated for some samples. Figure 5.8a and b show that the molecular weight of the polymer has little influence on the size of the particles. Only in the case of low molecular weight and high concentration of PS, the particles size is significantly smaller. This difference in size is very interesting as it changes the magnetic properties of the nanoparticles, as will be discussed later.

Figure 5.5 demonstrates that with the same molecular weight of PS-NH_2 (Mn = 2300 g/mol) and the same concentration of cobalt carbonyl (21.9 mM), only by changing the concentration of PS-NH_2, the size of PS-Co NPs varied significantly, ranging from 12 nm to 21 nm. The morphology of the PS-Co NPs was also different. With higher concentration of PS-NH_2, the particles were well-defined, smaller in size, and spherical in shape. While with lower concentration, the particles are larger, ill-defined, and had different

shapes. It is interesting to note that the particles were surrounded by a thick polymer layer on the surface when using a higher polymer concentration (5 mM). In addition, they were clearly separated from each other (Figure 5.5a and b). However, with lower polymer concentration of 2.5 mM, the distance between the particles was shorter (Figure 5.5c and d). When the concentration of the polymer was lowered to 1.25 mM, the distance between the particles was further reduced and 1-D chain structures were observed (Figure 5.5e and f). When the polymer concentration further reduced (0.67 mM), which was too low to protect the particles, thus, the NPs were polydispersed and aggregated (Figure 5.5g and h). Figure 5.8a also shows that the lower the polymer concentration, the more polydispersed the particles are.

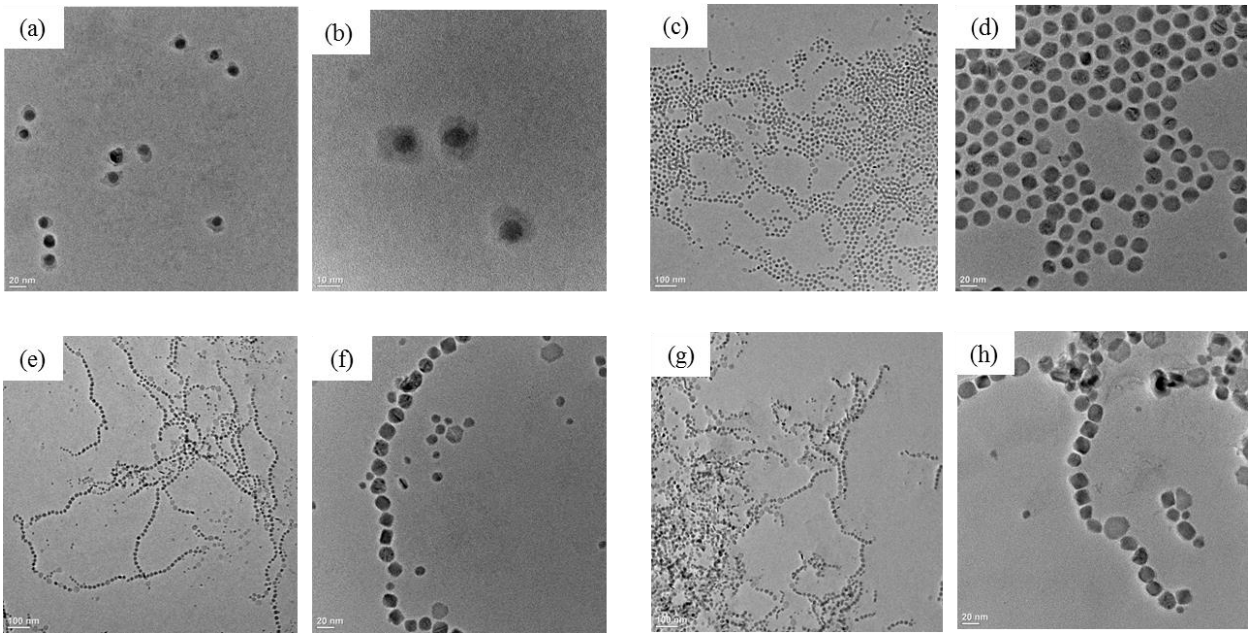

Figure 5.5 TEM images of PS-Co NPs synthesized with the concentration of cobalt carbonyl at 21.9 mM, and with different concentration of PS-NH_2 (Mn = 2300 g/mol, C_{PS}): (a, b) C_{PS} = 5 mM, *D* = 12 nm ± 1.9 nm; (c, d) C_{PS} = 2.5 mM, *D* = 21 nm ± 1.3 nm; (e, f) C_{PS} = 1.25 mM, *D* = 18 nm ± 2.1 nm; (g, h) C_{PS} = 0.63 mM, *D* = 20 nm ± 3.3 nm. The PS-Co NP samples were prepared on TEM grids from respective Co NP dispersion in DCB.

PS-Co NPs with higher molecular weight of PS-NH_2 (Mn = 4500 g/mol) as surfactant were also prepared. On the contrary to the synthesis of PS-Co NPs with PS-NH_2 (Mn = 2300 g/mol), the size of the nanoparticles did not change notably by varying the concentration of the polymer. Most of these nanoparticles were around 20 nm in size and formed 1-D chain structures (Figure 5.6a–h). Furthermore, the influence of the concentration of $Co_2(CO)_8$ on the size and size distribution of PS-Co NPs was also investigated. The concentration of polymer was fixed at 2.5 mM for these experiments. Well-defined and narrowly distributed particles were obtained when the concentration of cobalt carbonyl is lower (7.3 mM) than the usually used concentration (21.9 mM) (Figure 5.6i and j). When increasing the concentration of $Co_2(CO)_8$ up to 58.4 mM, ill-defined particles were observed (Figure 5.6k and l). Figure 5.8b revealed that the higher concentration of $Co_2(CO)_8$, which means a lower ratio of polymer/cobalt, resulted in larger and polydispersed PS-Co NPs. Thus, presence of adequate amount of surfactants is required to form well-defined nanoparticles and simultaneously provide stabilization against agglomeration.

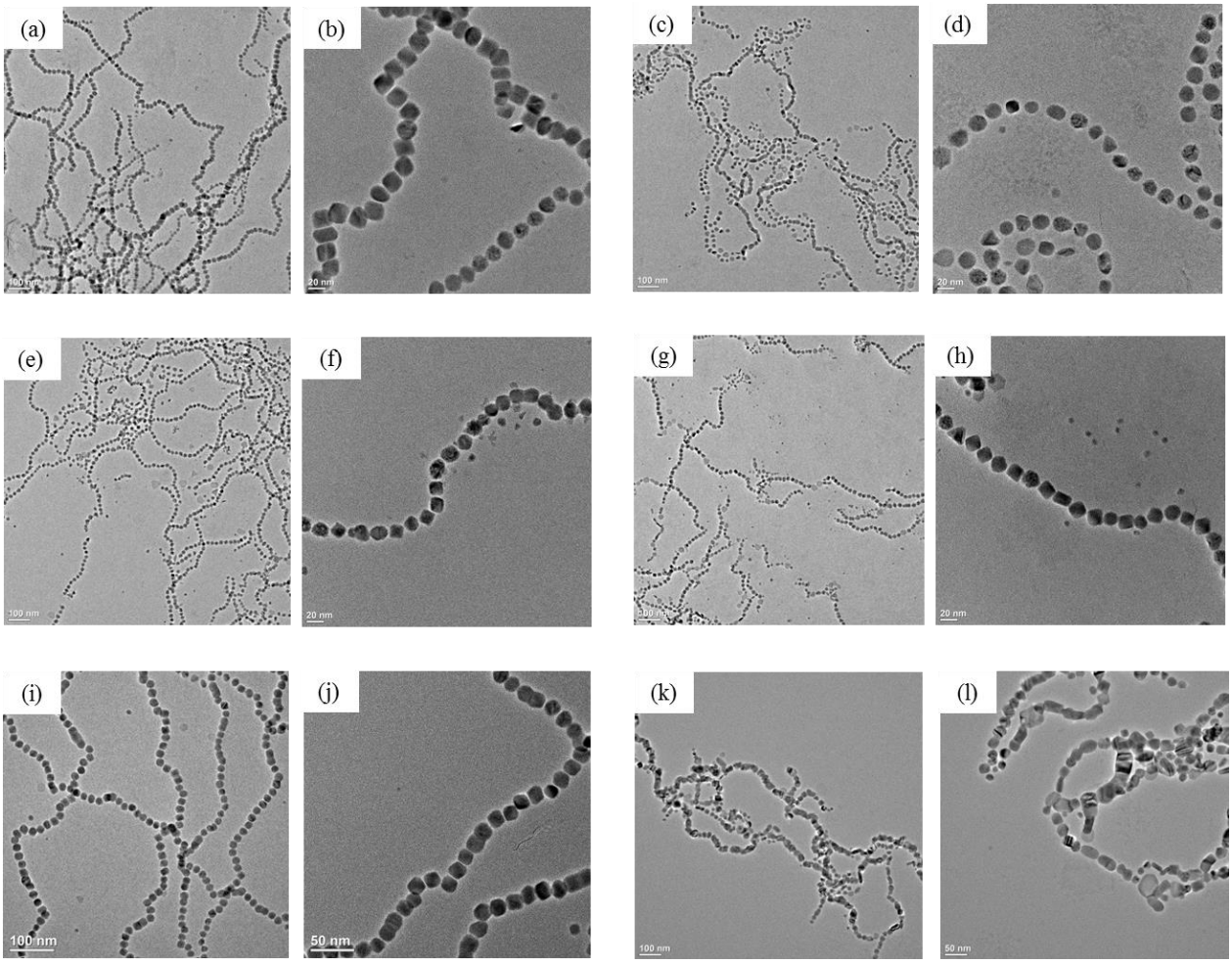

Figure 5.6 (a–h)TEM images of PS-Co NPs synthesized with the concentration of cobalt carbonyl at 21.9 mM, and with different concentration of PS-NH_2 (Mn = 4500 g/mol, C_{PS}): (a, b) C_{PS} = 5 mM, D = 21 nm ± 1.9 nm; (c, d) C_{PS} = 2.5 mM, D = 20 nm ± 2.1 nm; (e, f) C_{PS} = 1.25 mM, D = 20 nm ± 1.5 nm; (g, h) C_{PS} = 0.63 mM, D = 18 nm ± 3.0 nm. (i–l) TEM images of PS-Co NPs synthesized with the concentration of PS-NH_2 (Mn = 4500 g/mol) at 2.5 mM, only with different concentration of cobalt carbonyl (C_{Co}): (i, j) C_{Co} = 7.3 mM, D = 18.8 nm ± 1.3 nm; (k, l) C_{Co} = 58.4 mM, D = 26.6 nm ± 7.9 nm. The PS-Co NP samples were prepared on TEM grid from the respective NP dispersion in DCB.

PS-Co NPs were synthesized with a third molecular weight of PS-NH_2 (Mn = 10500 g/mol) as surfactant. Similar to the NPs prepared with PS-NH_2 (Mn = 4500 g/mol), the size of the nanoparticles was around 20 nm and did not change significantly by varying the concentration of the polymer. Most of these nanoparticles self-assembled into 1-D chain structures (Figure 5.7). Figure 5.8c shows the size distribution when using different molecular weight and concentration of PS-NH_2. A significant change in the size was observed only with the molecular weight of 2300 g/mol and the concentration of 5 mM by fixing cobalt carbonyl concentration at 21.9 mM. The observation that Co NPs synthesized with PS-NH_2 (Mn = 2300 g/mol) at higher concentration were smaller than these synthesized in the presence of PS of higher molecular weight could be explained by the Co NPs growth process and the steric hindrance of surfactant.

After injection of metal precursor $Co_2(CO)_8$, they formed either nuclei or Co-surfactant complexes, which were competing with each other. The nucleation was dependent on the supersaturation level of Co atoms, which is influenced by the Co-surfactant complexes. Thus, the Co-surfactant determines the growth of nanoparticles. In this study, the lower molecular weight of PS-NH_2 with less steric hindrance formed a closely packed shell on the surface of the nanoparticles. As long as the nanoparticles surface was well covered by the surfactants, the nanoparticles stop growing.[8,19] Such a close shell was not formed in presence of PS-NH_2 of higher molecular weight and hence, larger NPs were obtained.

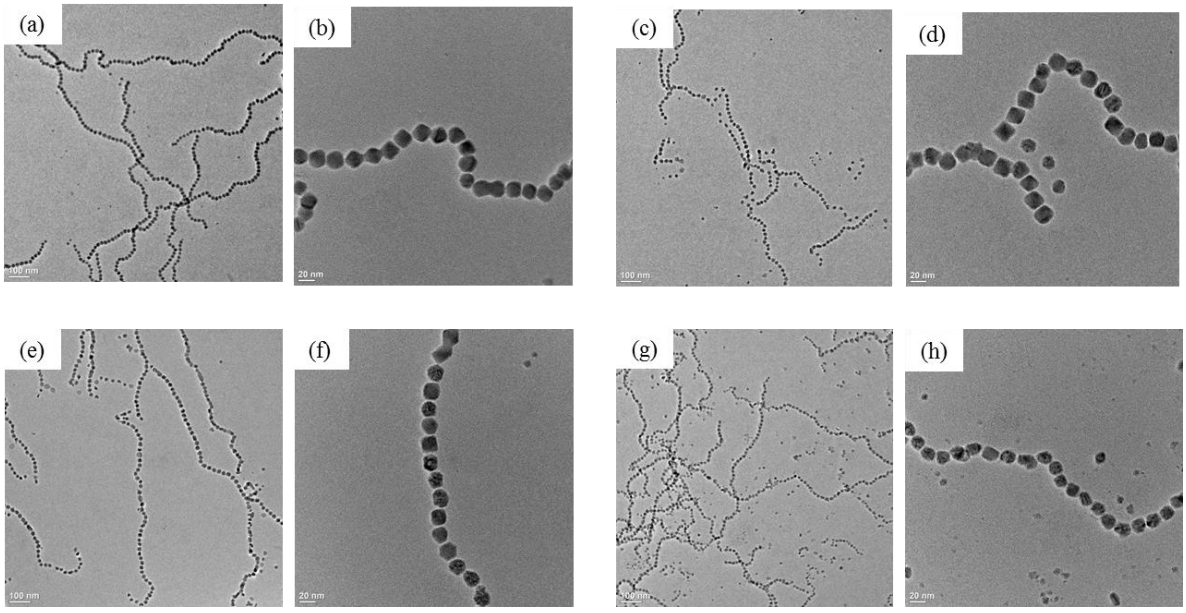

Figure 5.7 TEM images of PS-Co NPs synthesized with the concentration of cobalt carbonyl at 21.9 mM, and only with different concentration of PS-NH_2 (Mn = 10500 g/mol, C_{PS}): (a, b) C_{PS} = 5 mM, D = 20 nm ± 2.0 nm; (c, d) C_{PS} = 2.5 mM, D = 21 nm ± 1.7 nm; (e, f) C_{PS} = 1.25 mM, D = 22 nm ± 1.6 nm; (g, h) C_{PS} = 0.63 mM, D = 17 nm ± 1.8 nm. The PS-Co NPs dispersion in DCB was dropped on to the TEM grid.

(a)

Molecular weight of PS (g/mol)	2300				4500						10500			
Concentration of $Co_2(CO)_8$ (mM)	21.9				21.9	21.9	21.9	21.9	7.3	58.4	21.9			
Concentration of PS (mM)	5.0	2.5	1.25	0.63	5.0	2.5	1.25	0.63	2.5	2.5	5.0	2.5	1.25	0.63
Diameter (nm)	12.0	20.7	17.8	19.7	21.4	20.4	19.5	18.4	18.8	26.6	20.0	20.5	21.6	16.8
Standard Deviation (nm)	1.9	1.3	2.1	3.3	1.9	2.1	1.5	3.0	1.3	7.9	2.0	1.7	1.6	1.8

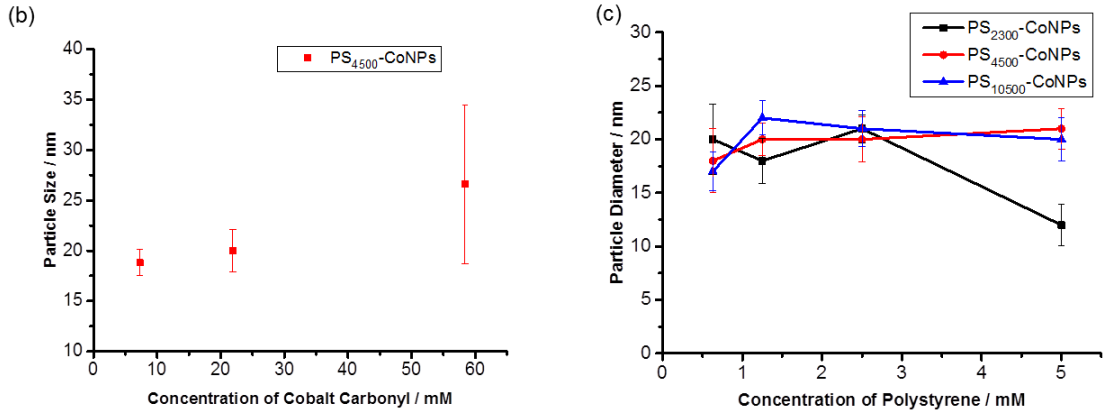

Figure 5.8 (a) Overview of varied synthesis parameters and diameter of the as-synthesized PS-Co NPs; (b) plot of size distribution of PS-Co NPs synthesized by fixing the concentration of PS-NH_2 (2.5 mM, Mn = 4500 g/mol), the concentration of cobalt carbonyl was varied (C_{Co}); (c) plot of size distribution of PS-Co NPs synthesized by fixing the concentration of cobalt carbonyl at 21.9 mM, the concentration and molecular weight of PS-NH_2 was varied. The size of PS-CoNPs was measured by ImageJ software.

In view of the difference in size and morphology between PS-Co NPs prepared by varying the parameters, two particles were exemplarily chosen to compare their magnetic properties, crystalline structures, and grafting density. One is PS-Co NPs of comparably small size of 12 nm prepared from PS-NH_2 (Mn = 2300 g/mol, 5 mM; PS_{2300}-Co NPs), and the other one is the NPs of 21 nm prepared from PS-NH_2 (Mn = 10500 g/mol, 2.5 mM; PS_{10500}-Co NPs). The NPs were prepared with cobalt carbonyl concentration of 21.9 mM), thus, the main difference in synthesis originated from the molecular weight and concentration of the polymeric surfactant.

5.3.3 Magnetic properties of PS-Co NPs

The measurements were conducted by Dr. Konrad Siemensmeyer at Helmholtz-Zentrum Berlin (HZB) with a SQUID magnetometer. TEM images and magnetization curves of the two nanoparticles were shown in Figure 5.9. The magnetic behavior of the PS_{2300}-Co NPs was characterized by a hysteresis loop at 4K (Figure 5.9a). At 300 K, no hysteresis appears verifying the expected superparamagnetic behavior of the synthesized particles with a size below the critical diameter for Co NPs. No saturation magnetization was observed at 4 K due to the thick polystyrene layer on the surface of Co NPs, which were shown in

TEM images (Figure 5.5a and b). The magnetization of the PS_{2300}-Co NPs is about 125 emu/g_{Co} at 4 K and 45 emu/g_{Co} at 300 K, which is lower than the saturation magnetization of bulk Co (162 emu/g) at room temperature.[35–37] The reason for this small reduction could be manifold. It is well-known that the energy of a magnetic nanoparticle under an external magnetic field is proportional to the volume of the particle, thus the energy of small particles is also small, and the thermal fluctuation greatly reduces the total magnetic moment.[38] Furthermore, the thick layer of polystyrene bound to the surface of the nanoparticles can also quench the magnetic moment.[39] Last but not least, the magnetic cobalt atoms on the surface of the nanoparticles, which have an incomplete coordination that increases their spin disorientation, can further decrease the effective magnetic moment.[40–43] While the 12 nm NPs are superparamagnetic, a hysteresis loop appeared for the PS_{10500}-Co NPs at 300 K, which indicated the ferromagnetic behavior of these 21 nm particles. The saturation magnetization of PS_{10500}-Co NPs at 300 K is around 104 emu/gr_{Co}, which is higher than that of PS_{2300}-Co NPs, indicating permanent dipolar interaction between the nanoparticles. This is the explanation why PS-Co NPs with larger sizes can self-assemble into 1-D chain structures.

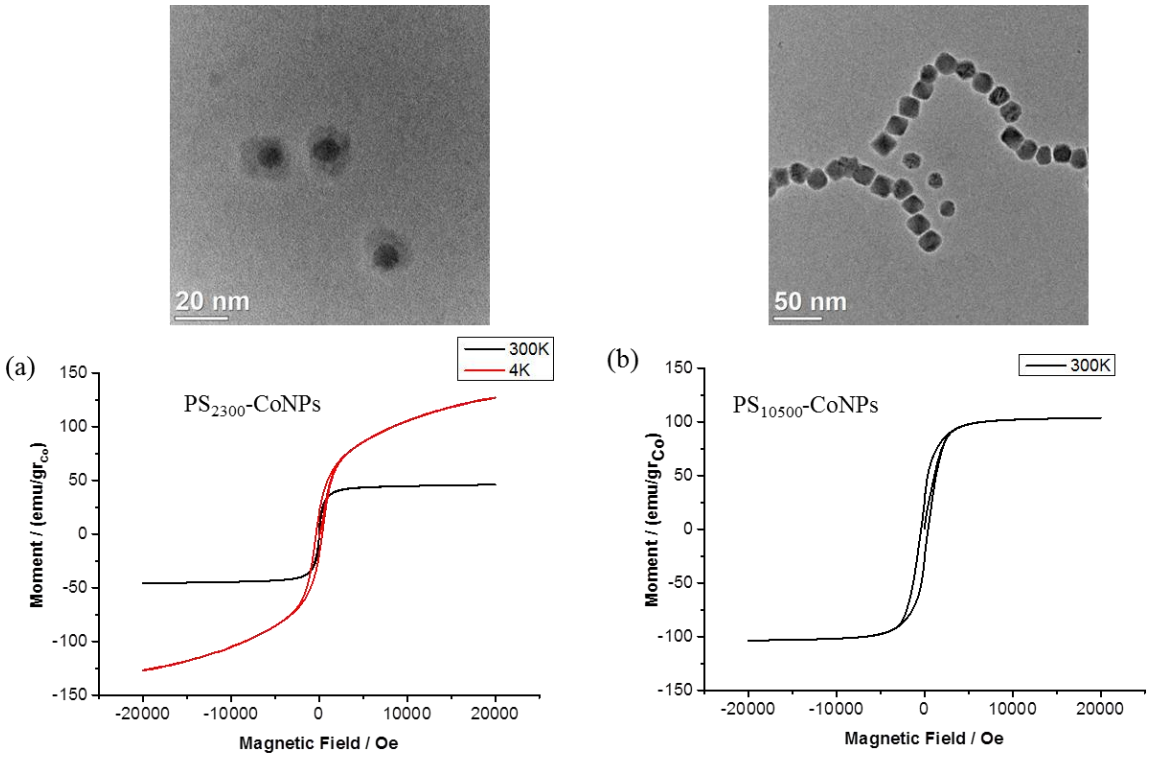

Figure 5.9 TEM images (upper) and field dependence of magnetization of PS-Co NPs (lower): (a) PS_{2300}-CoNPs at 4 K and 300 K; (b) PS_{10500}-Co NPs at 300K.

5.3.4 Wide angle X-ray scattering of PS-Co NPs

Cobalt nanoparticles have appeared in two different crystal structures— hexagonal-close-packed (hcp) and face-centered-cubic (fcc). However, when Bawendi synthesized cobalt nanoparticles through the thermolysis of cobalt carbonyl with trioctylphosphane oxide (TOPO) as the ligand, a new crystalline phase, the epsilon (ε) structure was identified.[5] Later, other researchers also found the epsilon cobalt crystalline phase by preparation via decomposition of cobalt carbonyl at high temperature with oleic acid (OA) and dioctylamine (DOA) as surfactants.[8] In this study, wide angle X-ray scattering was used to

investigate the crystalline phase of 12 nm PS_{2300}-Co NP and 21 nm PS_{10500}-Co NPs. As shown in Figure 5.10, both of these two samples exhibited the epsilon (ε) crystal structure, the diffraction peaks at 2θ 44.6°, 47.1° and 49.6° are corresponding to (221), (310) and (311) reflections of the samples, respectively.[44–46] This was in accordance with the previous report by Pyun, who synthesized PS-Co NPs by using PS-NH_2 as surfactant via a dual-stage temperature decomposition of $Co_2(CO)_8$ at 175 °C and 160 °C.[25] In Figure 5.10, the sample PS_{2300}-Co NPs shows sharp and clear peaks, indicating a good crystallinity, while for the sample of PS_{10500}-Co NPs, the peaks are broad, and the peak 2θ at 49.6° is almost invisible, which exhibited a ill crystallinity of the sample.

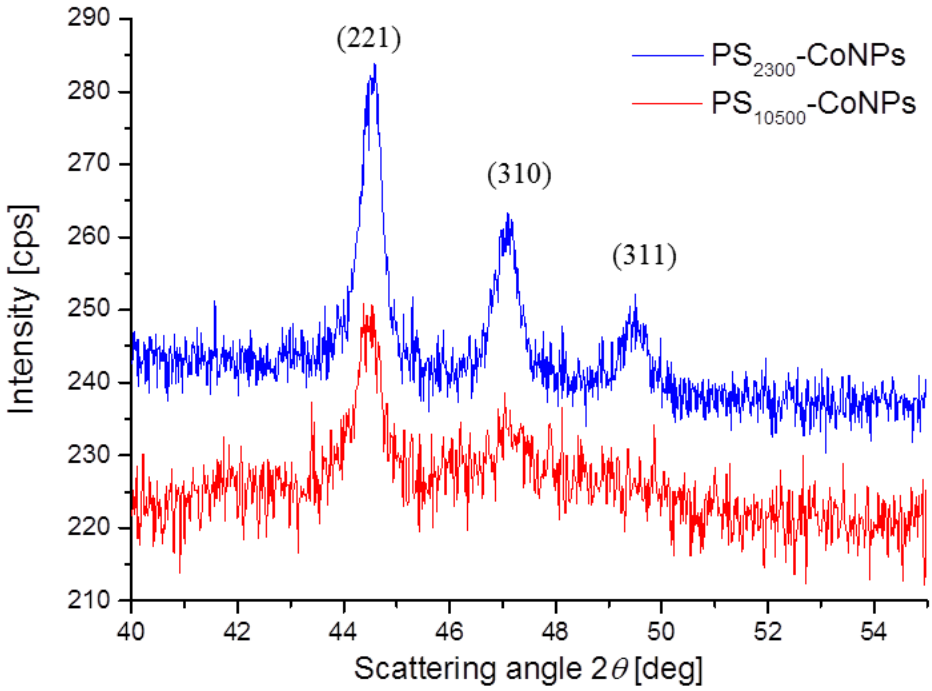

Figure 5.10 WAXS patterns of PS_{2300}-Co NPs and PS_{10500}-Co NPs.

5.3.5 Calculation of surface polymer density

Generally, thermogravimetric analysis (TGA) is a widely used technique to evaluate the organic content on the surface of NPs.[47–49] The density of polystyrene on the nanoparticle surface was calculated according to TGA. The equation for calculation of the grafting density of the polymer content on the surface of cobalt nanoparticles (φ) is shown below:

$$\varphi = \frac{N_{(polymer)}}{N_{(NPs)}\, S_{(NPs)}} = \frac{W_{(polymer)} N_A R\, \rho}{3\, M_{(polymer)}\, W_{(NPs)}}$$

Here, $W_{(polymer)}$ and $W_{(NPs)}$ present the weight loss percentage of polystyrene and the weight percentage of Co NPs, $N_{(polymer)}$ and $N_{(NPs)}$ present the number of polystyrene and Co NPs, respectively, $S_{(NPs)}$ is the total surface area of NPs, ρ is the density of Co NPs (8.9 g/cm^3), N_A is the Avogadro's number, R is the radius of PS-Co NPs, and $M_{(polymer)}$ is the molecular weight of polystyrene. In this study, the grafting density of 12 nm PS_{2300}-Co NPs and 21 nm PS_{10500}-Co NPs was calculated.

Gel permeation chromatography (GPC) and matrix-assisted laser desorption/ionization time-of-flight (MALDI-ToF) mass spectrometry are two popular techniques for the determination of the molecular

weight of a polymer. GPC results are shown in Figure 5.4, the molecular weight of the synthesized PS-NH_2 were 2300 g/mol and 10500 g/mol, respectively. As polystyrene was used for calibration during GPC measurements, it can be expected that the GPC results should be rather accurate. The molecular weight was also analyzed by MALDI-ToF mass spectrometry, as shown in Figure 5.11. The polymer with lower molecular weight showed Mn of 3130 Da according to the MALDI-ToF measurement (Figure 5.11a), which was higher than that of 2300 g/mol measured by GPC. However, the molecular weight of 10600 Da measured by MALDI-ToF mass spectrometry for the second polymer, was well in agreement with the 10500 g/mol measured by GPC. In fact, the molecular weight determined by MALDI-ToF is similar to the GPC value only if the polymer has a narrow molecular weight distribution (Mw/Mn < 1.2). For broad distributions, the molecular weight obtained by MALDI-ToF mass spectrometry usually deviates from the real molecular weight. Since the value of Mw/Mn is 1.17 for PS (Mn = 10500 g/mol), which is lower than 1.2, the molecular weight measured by MALDI-ToF matches with GPC. However, for PS (Mn = 2300 g/mol), the value of Mw/Mn is 1.38, which is beyond the range of realistic values obtained by MALDI-TOF, and thus, the deviation between the results of these two techniques is not surprising.[50,51] Therefore, the molecular weight of the polymers measured by GPC was chosen for the calculation of the grafting density.

The TGA overview shows the weight loss as a function of temperature for Co NPs with the two investigated polymers as well as for free PS-NH_2 (Mn = 2300 g/mol) (Figure 5.12a). Figure 5.12b demonstrates that the weight loss in the temperature range of 200–420 °C corresponds to the decomposition of PS-NH_2. For PS_{10500}-Co NPs, the weight loss of about 6.5 % below 200 °C is attributed to removal of adsorbed solvent.[52–54] The significant weight loss stages of 47.5 % in total which is observed between 200–420 °C is attributed to the decomposition of PS-NH_2 (Mn = 10500 g/mol) attached to the surface of Co NPs (Figure 5.12c). Figure 5.12d shows the TGA profile of PS_{2300}-CoNPs. The initial weight loss of about 9.8 % below 200 °C is equally explained by adsorbed solvent. The weight loss of about 52.8 % in the temperature range of 200–420 °C can be ascribed to the decomposition of PS-NH_2 (Mn = 2300 g/mol) on the surface. Therefore, for PS_{10500}-Co NPs, with $W_{(PS)}$ = 47.5 % and $W_{(NPS)}$ = 43.6 %, the polymer density was calculated to 1.9 chains / nm^2. Similarly, the polymer density was calculated for PS_{2300}-Co NPs, with $W_{(PS)}$ = 52.8 % and $W_{(NPs)}$ = 28 %, as 8.7 chains / nm^2. Therefore, the polymer density of PS (Mn = 2300 g/mol) on the surface of Co NPs is much higher than that of PS (Mn = 10500 g/mol), which is in agreement with TEM images (Figure 5.4a and b, Figure 5.6c and d).

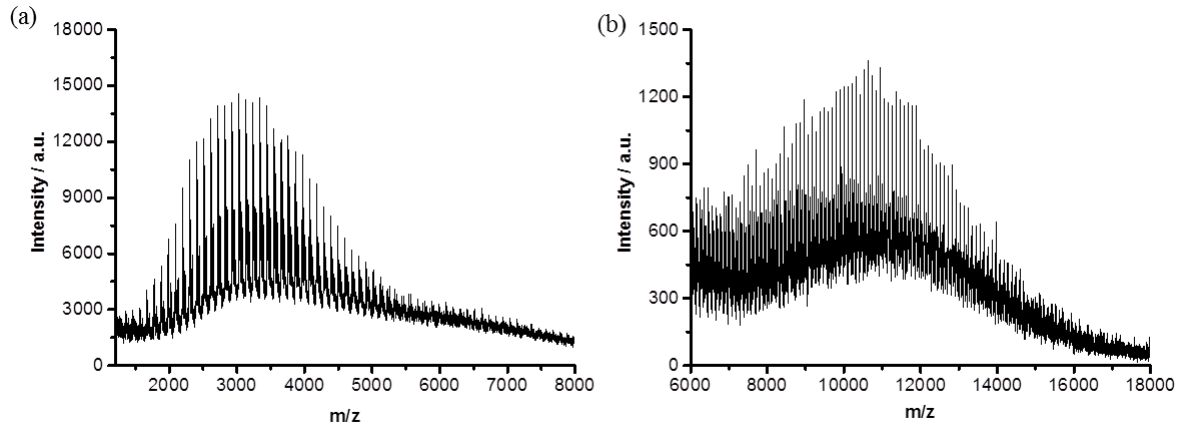

Figure 5.11 MALDI-ToF mass spectra of polystyrene: 3130 Da (a) and 10600 Da (b).

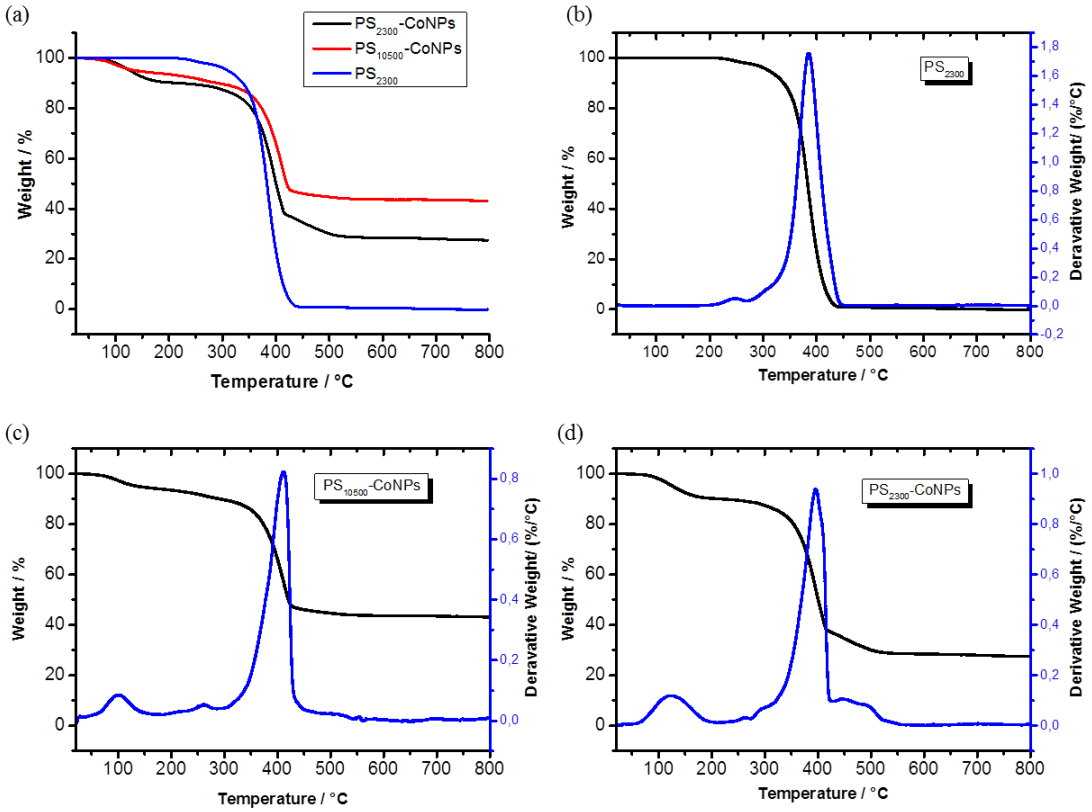

Figure 5.12 TGA analysis: (a) overview profile of PS_{2300}-Co NPs, PS_{10500}-Co NPs and free PS-NH_2 (Mn = 2300); (b) free PS-NH_2 (Mn = 2300); (c) PS_{10500}-Co NPs; (d) PS_{2300}-Co NPs. The black lines indicate the percent weight as a function of temperature and the weight loss derivative is shown in blue.

5.3.6 Stability study

The amine end-functionalized polystyrene provides steric repulsion between cobalt nanoparticles and prevents them from agglomerating. As the surfactants play a significant role in the growth of the nanoparticles, their preparation by changing the conditions of surfactant could influence their stability. Therefore, the stability of the NP dispersions was monitored after 20 days. As shown in Figure 5.13, the stability of the PS-Co NPs can be readily observed visually. Figure 5.13 (a–d) shows PS-Co NPs prepared by using PS-NH_2 (Mn = 2300 g/mol), (e–h) shows PS-NH_2 (Mn = 10500 g/mol), (i–m) shows PS-NH_2 (Mn = 4500 g/mol) at different concentration, respectively. The first conclusion was that Co NPs prepared

with higher polymer molecular weight were more stable than these with lower molecular weight at the same concentration. This can be easily observed from the samples with a rather low polymer concentration of 0.63 mM (Figure 5.13 (d, h and l)), in which (d) showed clear precipitation, while h and l showed less aggregation or no aggregation. Second, higher concentration of polymer enhances the stability of the nanoparticles, which can be observed from (a) to (d), as the nanoparticles gradually become less stable with lower polymer concentration. Third, higher concentration of cobalt carbonyl reduces the stability, which is shown in (m) and (n). All in all, a thicker polymer coating and longer polymer chain (e.g., Mn = 10500 g/mol) enhanced the NP stability, which could be stored at least three months.

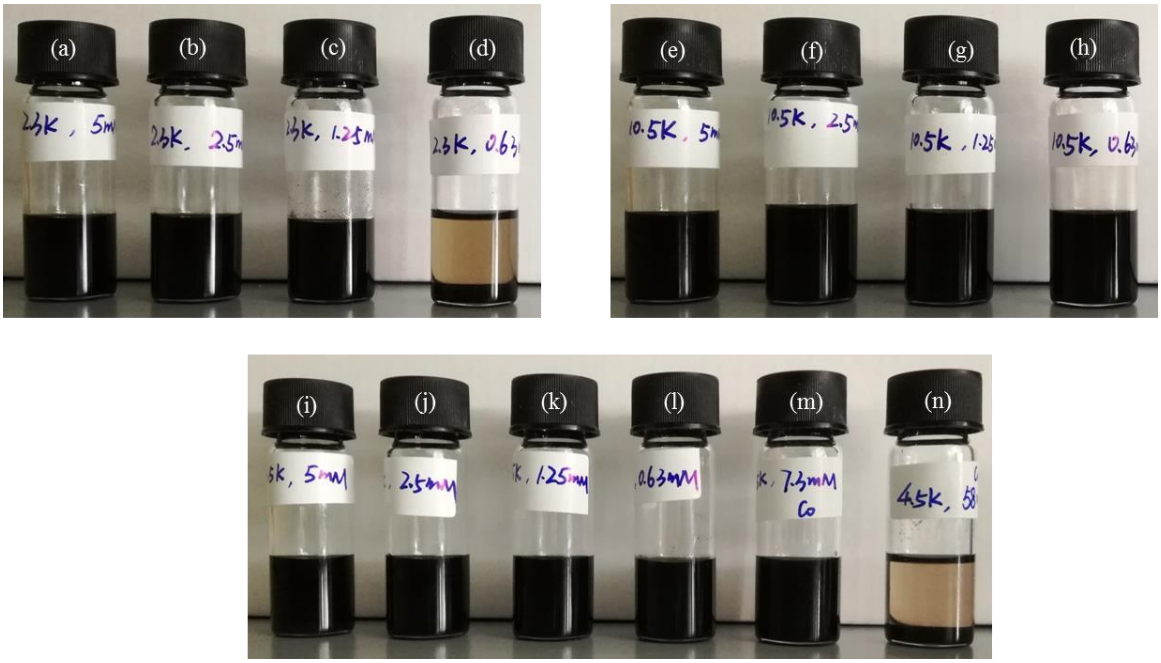

Figure 5.13 Photographs of PS-Co NPs synthesized at different conditions in 1,2-dichlorobenzene: (a–d) prepared with PS-NH_2 (Mn = 2300 g/mol) at concentration of 5 mM (a), 2.5 mM (b), 1.25 mM (c), 0.63 mM (d) with cobalt carbonyl concentration of 21.9 mM; (e–h) prepared with PS-NH_2 (Mn = 10500 g/mol) at concentration of 5 mM (a), 2.5 mM (b), 1.25 mM, with cobalt carbonyl concentration of 21.9 mM; (i–l) prepared with PS-NH_2 (Mn = 4500 g/mol) at concentration of 5 mM (a), 2.5 mM (b), 1.25 mM, with cobalt carbonyl concentration 21.9 mM; (m, n) prepared with PS-NH_2 (Mn = 4500 g/mol) at concentration of 2.5 mM, and cobalt carbonyl concentration of 7.3 mM (m) and 58.4 mM (n). These photographs were taken three weeks after the synthesis.

5.4 Conclusions

In summary, amine end-functionalized polystyrene-coated cobalt nanoparticles were prepared via the dual-stage thermolysis of cobalt carbonyl ($Co_2(CO)_8$). The polystyrene surfactants with different molecular weight were prepared via atom-transfer radical polymerization technique. By changing the surfactants molecular weight and concentration, the size, morphology and magnetic properties were different. Transmission electron microscopy characterization showed that the size of cobalt nanoparticles stabilized with PS (Mn = 2300 g/mol) varied from 12–22 nm, while the size of PS-Co NPs with PS (Mn =

4500 g/mol and 10500 g/mol) showed little change. Magnetic measurements exhibited that the small cobalt particles of 12 nm were superparamagnetic, while larger particles were ferromagnetic and self-assembled into 1-D chains. Thermogravimetric analysis showed that a higher grafting density of polystyrene was reached with the polymeric surfactant of lower molecular weight compared to those with higher molecular weight. Wide angle X-ray scattering measurements revealed that both superparamagnetic and ferromagnetic cobalt nanoparticles exhibited the epsilon crystalline phase.

5.5 References

1. Mornet, S., Vasseur, S., Grasset, F. & Duguet, E. Magnetic nanoparticle design for medical diagnosis and therapy. *Forunal Mater. Chem.* **14,** 2161–2175 (2004).
2. Frey, N. A., Peng, S., Cheng, K. & Sun, S. Magnetic nanoparticles: synthesis, functionalization, and applications in bioimaging and magnetic energy storage. *Chem. Soc. Rev.* **38,** 2532 (2009).
3. de Dios, A. S. & Díaz-García, M. E. Multifunctional nanoparticles:analytical prospects. *Anal. Chim. Acta* **666,** 1–22 (2010).
4. Corot, C., Robert, P., Idée, J. M. & Port, M. Recent advances in iron oxide nanocrystal technology for medical imaging. *Adv. Drug Deliv. Rev.* **58,** 1471–1504 (2006).
5. Dinega, D. P. & Bawendi, M. G. A solution-phase chemical approach to a new crystal structure of cobalt. *Angew. Chemie - Int. Ed.* **38,** 1788–1791 (1999).
6. Valetsky, P. M., Yanovskaya, I. M. & Obolonkova, E. S. Cobalt nanoparticles in block copolymer micelles : Preparation and properties. *Polymer.* **2,** 1–6 (1996).
7. Ribeiro, R. U., Liberatori, J. W. C., Winnishofer, H., Bueno, J. M. C. & Zanchet, D. Colloidal Co nanoparticles supported on SiO_2:synthesis, characterization and catalytic properties for steam reforming of ethanol. *Appl. Catal. B Environ.* **91,** 670–678 (2009).
8. Bao, Y., Beerman, M., Pakhomov, A. B. & Krishnan, K. M. Controlled crystalline structure and surface stability of cobalt nanocrystals. *J. Phys. Chem.* **109,** 7220–7222 (2005).
9. Diana, F. S., Lee, S. H., Petroff, P. M. & Kramer, E. J. Fabrication of hcp-Co nanocrystals via rapid pyrolysis in inverse PS-b-PVP micelles and thermal annealing. *Nano Lett.* **3,** 891–895 (2003).
10. Burke, N. A. D., Stöver, H. D. H. & Dawson, F. P. Magnetic nanocomposites:preparation and characterization of polymer-coated iron nanoparticles. *Chem. Mater.* **14,** 4752–4761 (2002).
11. Liu, G., Yan, X., Lu, Z., Curda, S. A. & Lal, J. One-pot synthesis of block copolymer coated cobalt nanocrystals. *Chem. Mater.* **17,** 4985–4991 (2005).
12. Thomas, J. R. Preparation and magnetic properties of colloidal cobalt particles. *J. Appl. Phys.* **37,** 2914–2915 (1966).
13. Tripp, S. L., Pusztay, S. V., Ribbe, A. E. & Wei, A. Self-assembly of cobalt nanoparticle rings. *J. Am. Chem. Soc.* **124,** 7914–7915 (2002).
14. Iablokov, V. *et al.* Size-controlled model Co nanoparticle catalysts for CO_2 hydrogenation:

synthesis, characterization, and catalytic reactions. *Nano Lett.* **12,** 3091–6 (2012).

15. Puntes, V. F., Krishnan, K. & Alivisatos, A. Synthesis of colloidal cobalt nanoparticles with controlled size and shapes. *Top. Catal.* **19,** 145–148 (2002).
16. Puntes, V. F., Zanchet, D., Erdonmez, C. K. & Alivisatos, A. P. Synthesis of hcp-Co nanodisks. *J. Am. Chem. Soc.* **124,** 12874–12880 (2002).
17. Kim, D. *et al.* Synthesis of uniform ferrimagnetic magnetite nanocubes. *J. Am. Chem. Soc.* **131,** 454–5 (2009).
18. Puntes, V. F., Krishnan, K. M. & Alivisatos, P. Synthesis, self-assembly, and magnetic behavior of a two-dimensional superlattice of single-crystal ε-Co nanoparticles. *Appl. Phys. Lett.* **78,** 2187–2189 (2001).
19. Bao, Y., An, W., Heath Turner, C. & Krishnan, K. M. The critical role of surfactants in the growth of cobalt nanoparticles. *Langmuir* **26,** 478–483 (2010).
20. Griffiths, C. H., O'Horo, M. P. & Smith, T. W. The structure, magnetic characterization, and oxidation of colloidal iron dispersions. *J. Appl. Phys.* **50,** 7108–7115 (1979).
21. Zalich, M. A., Vadala, M. L., Riffle, J. S., Saunders, M. & St. Pierre, T. G. Structural and magnetic properties of cobalt nanoparticles encased in siliceous shells. *Chem. Mater.* **19,** 6597–6604 (2007).
22. Safran, S. A. Ferrofluids: Magnetic strings and networks. *Nat. Mater.* **2,** 71–72 (2003).
23. Kolhatkar, A. G., Jamison, A. C., Litvinov, D., Willson, R. C. & Lee, T. R. Tuning the magnetic properties of nanoparticles. *Int. J. Mol. Sci.* **14,** 15977–16009 (2013).
24. Korth, B. D. *et al.* Polymer-coated ferromagnetic colloids from well-defined macromolecular surfactants and assembly into nanoparticle chains. *J. Am. Chem. Soc.* **128,** 6562–6563 (2006).
25. Keng, P. Y., Shim, I., Korth, B. D., Douglas, J. F. & Pyun, J. Synthesis and self-assembly of polymer-coated ferromagnetic nanoparticles. *ACS Nano* **1,** 279–292 (2007).
26. Bull, M. M. *et al.* Synthesis of ferromagnetic polymer coated nanoparticles on multi-gram scale with tunable particle size. *J. Mater. Chem.* **20,** 6023 (2010).
27. Matyjaszewski, K. & Tsarevsky, N. V. Nanostructured functional materials prepared by atom transfer radical polymerization. *Nat. Chem.* **1,** 276–288 (2009).
28. Braunecker, W. A. & Matyjaszewski, K. Controlled/living radical polymerization: Features, developments, and perspectives. *Prog. Polym. Sci.* **32,** 93–146 (2007).
29. Wang, J. S. & Matyjaszewski, K. Controlled/"living" radical polymerization. atom transfer radical polymerization in the presence of transition-metal complexes. *J. Am. Chem. Soc.* **117,** 5614–5615 (1995).
30. Matyjaszewski, K. & Xia, J. Atom transfer radical polymerization. *Chem. Rev.* **101,** 2921–2990 (2001).
31. di Lena, F. & Matyjaszewski, K. Transition metal catalysts for controlled radical polymerization. *Prog. Polym. Sci.* **35,** 959–1021 (2010).
32. Coessens, V., Pintauer, T. & Matyjaszewski, K. Functional polymers by atom transfer radical polymerization. *Prog. Polym. Sci.* **26,** 337–377 (2001).

33. Siegwart, D. J., Oh, J. K. & Matyjaszewski, K. ATRP in the design of functional materials for biomedical applications. *Prog. Polym. Sci.* **37,** 18–37 (2012).
34. Nigh, W. G. The gabriel synthesis of benzylamine. *J. Chem. Educ.* **50,** 670–671 (1975).
35. Tracy, J. B., Weiss, D. N., Dinega, D. P. & Bawendi, M. G. Exchange biasing and magnetic properties of partially and fully oxidized colloidal cobalt nanoparticles. *Phys. Rev. B - Condens. Matter Mater. Phys.* **72,** 1–8 (2005).
36. Srikala, D., Singh, V. N., Banerjee, A., Mehta, B. R. & Patnaik, S. Control of magnetism in cobalt nanoparticles by oxygen passivation. *J. Phys. Chem. C* **112,** 13882–13885 (2008).
37. Childress, J. R. & Chien, C. L. Reentrant magnetic behavior in fcc Co-Cu alloys. *Phys. Rev. B* **43,** 8089–8093 (1991).
38. Shafi, K. V. P. M., Gedanken, A., Prozorov, R. & Balogh, J. Sonochemical preparation and size-dependent properties of nanostructured $CoFe_2O_4$ particles. *Chem. Mater.* **10,** 3445–3450 (1998).
39. Van Leeuwen, D. A. *et al.* Quenching of magnetic moments by ligand-metal interactions in nanosized magnetic metal clusters. *Phys. Rev. Lett.* **73,** 1432–1435 (1994).
40. Mørup, S. Superparamagnetism and spin glass ordering in magnetic nanocomposites. *EPL* **28,** 671–676 (1994).
41. Shamim, N., Hong, L., Hidajat, K. & Uddin, M. S. Thermosensitive polymer (*N*-isopropylacrylamide) coated nanomagnetic particles: Preparation and characterization. *Colloids Surfaces B Biointerfaces* **55,** 51–58 (2007).
42. Chen, D. H. & Wu, S. H. Synthesis of nickel nanoparticles in water-in-oil microemulsions. *Chem. Mater.* **12,** 1354–1360 (2000).
43. Hwang, J. H. *et al.* Magnetic properties of graphitically encapsulated nickel nanocrystals. *J. Mater. Res.* **12,** 1076–1082 (1997).
44. Sun, S. & Murray, C. B. Synthesis of monodisperse cobalt nanocrystals and their assembly into magnetic superlattices (invited). *J. Appl. Phys.* **85,** 4325–4330 (1999).
45. Park, J. Il *et al.* Superlattice and magnetism directed by the size and shape of nanocrystals. *ChemPhysChem* **3,** 543–547 (2002).
46. Bao, Y., Beerman, M., Fakhomov, A. B. & Krishnan, K. M. Controlled crystalline structure and surface stability of cobalt nanocrystals. *J. Phys. Chem. B* **109,** 7220–7222 (2005).
47. Mansfield, E., Tyner, K. M., Poling, C. M. & Blacklock, J. L. Determination of nanoparticle surface coatings and nanoparticle purity using microscale thermogravimetric analysis. *Anal. Chem.* **86,** 1478–1484 (2014).
48. Benoit, D. N. *et al.* Measuring the grafting density of nanoparticles in solution by analytical ultracentrifugation and total organic carbon analysis. *Anal. Chem.* **84,** 9238–9245 (2012).
49. Babu, K. & Dhamodharan, R. Synthesis of polymer grafted magnetite nanoparticle with the highest grafting density via controlled radical polymerization. *Nanoscale Res. Lett.* **4,** 1090–1102 (2009).
50. Macha, S. F. & Limbach, P. A. Matrix-assisted laser desorption/ionization (MALDI) mass spectrometry of polymers. *Curr. Opin. Solid State Mater. Sci.* **6,** 213–220 (2002).

51. Wu, K. J. & Odom, R. W. Characterizing synthetic polymers by MALDI MS. *Anal. Chem.* **70,** 456A–461A (1998).

52. Rostami, A., Atashkar, B. & Moradi, D. Synthesis, characterization and catalytic properties of magnetic nanoparticle supported guanidine in base catalyzed synthesis of α-hydroxyphosphonates and α-acetoxyphosphonates. *Appl. Catal. A Gen.* **467,** 7–16 (2013).

53. Wang, M., Peng, M.-L., Cheng, W., Cui, Y.-L. & Chen, C. A Novel approach for transferring oleic acid capped iron oxide nanoparticles to water phase. *J. Nanosci. Nanotechnol.* **11,** 3688–3691 (2011).

54. Prakash, A. *et al.* Bylayers as phase transfer agents for nanocrystals prepared in nonpolar solvents. *ACS Nano* **3,** 2139–2146 (2009).

6 Summary and Outlook

This thesis mainly covers the synthesis, surface modification, magnetic-field-induced assembly and thermo-responsive functionalization of superparamagnetic Co NPs initially stabilized by hydrophobic small molecules oleic acid (OA) and trioctylphosphine oxide (TOPO), as well as the synthesis of both superparamagnetic and ferromagnetic Co NPs by using end-functionalized-polystyrene as stabilizer.

Co NPs, due to their excellent magnetic and catalytic properties, have great potential application in various fields, such as ferrofluids, catalysis, and magnetic resonance imaging (MRI). Superparamagnetic Co NPs are especially interesting, since they exhibit zero coercivity. They get magnetized in an external magnetic field and reach their saturation magnetization rapidly, but no magnetic moment remains after removal of the applied magnetic field. Therefore, they do not agglomerate in the body when they are used in biomedical applications. Normally, decomposition of metallic precursors at high temperature is one of the most important methods in preparation of monodisperse magnetic NPs, providing tunability in size and shape. Hydrophobic ligands like OA, TOPO and oleylamine are often used to both control the growth of NPs and protect them from agglomeration. The as-prepared magnetic NPs can be used in biological applications as long as they are transferred into water. Moreover, their supercrystal assemblies have the potential for high density data storage and electronic devices. In addition to small molecules, polymers can also be used as surfactants for the synthesis of ferromagnetic and superparamagnetic NPs by changing the reaction conditions. Therefore, chapter 2 gives an overview on the basic concept of synthesis, surface modification and self-assembly of magnetic nanoparticles. Various examples were used to illustrate the recent work.

The hydrophobic Co NPs synthesized with small molecules as surfactants limit their biological applications, which require a hydrophilic or aqueous environment. Surface modification (e.g., ligand exchange) is a general idea for either phase transition or surface-functionalization. Therefore, in chapter 3, a ligand exchange process was conducted to functionalize the surface of Co NPs. PNIPAM is one of the most popular smart polymers and its lower critical solution temperature (LCST) is around 32 °C, with a reversible change in the conformation structure between hydrophobic and hydrophilic. The novel nanocomposites of superparamagnetic Co NPs and thermo-responsive PNIPAM are of great interest. Thus, well-defined superparamagnetic Co NPs were firstly synthesized through the thermolysis of cobalt carbonyl by using OA and TOPO as surfactants. A functional ATRP initiator, containing an amine (as anchoring group) and a 2-bromopropionate group (SI-ATRP initiator), was used to replace the original ligands. This process is rapid and facial for efficient surface functionalization and afterwards the Co NPs can be dispersed into polar solvent DMF without aggregation. FT-IR spectroscopy showed that the TOPO was completely replaced, but a small amount of OA remained on the surface. A TGA measurement allowed the calculation of the grafting density of the initiator as around 3.2 initiator/nm^2. Then, the surface-initiated ATRP was conducted for the polymerization of NIPAM on the surface of Co NPs and rendered the nanocomposites water-dispersible. A temperature-dependent dynamic light scattering study showed the aggregation behavior of PNIPAM-coated Co NPs upon heating and this process was proven to

be reversible. The combination of superparamagnetic and thermo-responsive properties in these hybrid nanoparticles is promising for future applications e.g. in biomedicine.

In chapter 4, the magnetic-field-induced assembly of superparamagnetic cobalt nanoparticles both on solid substrates and at liquid-air interface was investigated. OA- and TOPO-coated Co NPs were synthesized via the thermolysis of cobalt carbonyl and dispersed into either hexane or toluene. The Co NP dispersion was dropped onto substrates (e.g., TEM grid, silicon wafer) and at liquid-air (water-air or ethylene glycol-air) interface. Due to the attractive dipolar interaction, 1-D chains formed in the presence of an external magnetic field. It is known that the concentration and the strength of the magnetic field can affect the assembly behavior of superparamagnetic Co NPs. Therefore, the influence of these two parameters on the morphology of the assemblies was studied. The formed 1-D chains were shorter and flexible at either lower concentration of the Co NP dispersion or lower strength of the external magnetic field due to thermal fluctuation. However, by increasing either the concentration of the NP dispersion or the strength of the applied magnetic field, these chains became longer, thicker and straighter. The reason could be that a high concentration led to a high fraction of short dipolar chains, and their interaction resulted in longer and thicker chains under applied magnetic field. On the other hand, when the magnetic field increased, the induced moments of the magnetic nanoparticles became larger, which dominated over the thermal fluctuation. Thus, the formed short chains connected to each other and grew in length. Thicker chains were also observed through chain-chain interaction. Furthermore, the induced moments of the NPs tended to direct into one direction with increased magnetic field, thus the chains were straighter. In comparison between the assembly on substrates, at water-air interface and at ethylene glycol-air interface, the assembly of Co NPs in hexane dispersion at ethylene glycol-air interface showed the most regular and homogeneous chain structures due to the better spreading of the dispersion on ethylene glycol subphase than on water subphase and substrates. The magnetic-field-induced assembly of superparamagnetic nanoparticles could provide a powerful approach for applications in data storage and electronic devices.

Chapter 5 presented the synthesis of superparamagnetic and ferromagnetic cobalt nanoparticles through a dual-stage thermolysis of cobalt carbonyl ($Co_2(CO)_8$) by using polystyrene as surfactant. The amine end-functionalized polystyrene surfactants with different molecular weight were prepared via atom transfer radical polymerization technique. The molecular weight determination of polystyrene was conducted by gel permeation chromatography (GPC) and matrix-assisted laser desorption/ionization time-of-flight (MALDI-ToF) mass spectrometry techniques. The results showed that, when the molecular weight distribution is low ($Mw/Mn < 1.2$), the measurement by GPC and MALDI-ToF MS provided nearly similar results. For example, the molecular weight of 10600 Da was obtained by MALDI-ToF MS, while GPC gave 10500 g/mol ($Mw/Mn = 1.17$). However, if the polymer is poly distributed, MALDI-ToF MS cannot provide an accurate value. This was exemplified for a polymer with a molecular weight of 3130 Da measured by MALDI-TOF MS, while GPC showed 2300 g/mol ($Mw/Mn = 1.38$). The size, size distribution and magnetic properties of the hybrid particles were different by changing either the molecular weight or concentration of the polymer surfactants. The analysis from TEM characterization showed that the size of cobalt nanoparticles stabilized with polystyrene of lower molecular weight (Mn =

2300 g/mol) varied from 12–22 nm, while the size with middle (Mn = 4500 g/mol) and higher molecular weight (Mn = 10500 g/mol) of polystyrene-coated cobalt nanoparticles showed little change. Magnetic measurements exhibited that the small cobalt particles (12 nm) were superparamagnetic, while larger particles (21 nm) were ferromagnetic and assembled into 1-D chains. The grafting density calculated from thermogravimetric analysis showed that a higher grafting density of polystyrene was obtained with lower molecular weight (Mn = 2300 g/mol) than those with higher molecular weight (Mn = 10500 g/mol). Due to the larger steric hindrance, polystyrene with higher molecular weight cannot form a dense shell on the surface of the nanoparticles, which resulted in a lower grafting density. Wide angle X-ray scattering measurements revealed the epsilon cobalt crystalline phases of both superparamagnetic Co NPs coated with polystyrene (Mn = 2300 g/mol) and ferromagnetic Co NPs coated with polystyrene (Mn = 10500 g/mol). Furthermore, a stability study showed that PS-Co NPs prepared with higher polymer concentration and polymer molecular weight exhibited a better stability.

In the future, there are three areas which are of special interest. First, the application of monodisperse superparamagnetic Co NPs in biological application could be investigated. Surface modification provides a general idea for the functionalization of hydrophobic Co NPs. For example, functional bio-molecules like amino acids, enzymes, peptides, due to the variety of -COOH, -NH_2 groups which have a strong affinity to the surface of Co NPs, can be used for ligand exchange. Because of the superparamagnetic properties of Co NPs, they will not agglomerate in the body after removal of the magnetic field. Furthermore, bio-molecules like enzymes can be recycled by a magnet when attached to Co NPs. Second, ferromagnetic Co NPs, due to dipole-dipole interaction, can self-assemble into 1-D chains. Thermo-responsive polymers, which have the critical solution temperature, can undergo the volume phase transition when changing the surrounding temperature. By coating a thick layer of such a smart polymer on the surface of ferromagnetic Co NPs, the self-assembly behavior can be easily tuned by changing the temperature. For example, PNIPAM has a lower critical solution temperature (LCST) around 32 °C and a core-shell microgel Co@PNIPAM could be synthesized through precipitaiton polymerization. Therefore, a cross-linked PNIPAM layer surrounding the surface of Co NPs would provide stability and exhibit a critical temperature, e.g., the volume phase transition temperature (VPTT). Below this temperature, the microgel swells in water and collapses above. With a large volume of the swollen PNIPAM layer, the dipolar interaction between Co NPs could be inhibited, thus the core-shell microgels Co@PNIPAM are randomly distributed and no chain structures form. When the surrounding temperature is higher than the VPTT, the coating layer shrinks, the distance between the particles becomes shorter, and thus they can form 1-D chain structures by the dipolar interaction. Third, due to the catalytic property of Co NPs, they can be used to catalyze reactions in various media including organic or aqueous solvent. There are lots of advantages by using magnetic Co NPs as catalyst. On the one hand, the catalytic properties can be controlled by coating stimuli-responsive polymers, such as thermo-, pH- and light-responsive polymers. Taking PNIPAM as example, the catalytic efficiency of Co@PNIPAM core-shell nanoreactors can be tuned by changing the temperature. When the temperature is lower than the VPTT, the gel is swollen by water, and the substrates can diffuse to the surface of Co NPs, thus the reaction rate is high. However,

increasing the temperature above the VPTT, shrinks the gel which becomes hydrophobic. This prevents molecules from reaching the Co NPs, thus the catalytic reaction does not take place. On the other hand, the magnetic Co NP catalysts can be recycled by a magnet, which reduces environmental pollution.

7 Zusammenfassung und Ausblick

Im Rahmen dieser Arbeit wurden superparamagnetische Cobalt Nanopartikel (NP) synthetisiert, deren Selbstassemblierung im Magnetfeld untersucht und die ursprünglichen Liganden Ölsäure (*Englisch oleic acid*, OA) und Trioctylphosphanoxid (TOPO) ersetzt, um eine Funktionalisierung der Nanopartikel mit einem Temperatur-responsiven Polymer zu erreichen. Außerdem wurden superparamagnetische und ferromagnetische Co NP mit end-funktionalisiertem Polystyrol als Stabilisator synthetisiert.

Co NP haben aufgrund ihrer herausragenden magnetischen und katalytischen Eigenschaften viele potentielle Anwendungen beispielsweise als Ferrofluide, in der Katalyse und der Magnetresonanztomografie (*Englisch magnetic resonance imaging*, MRI). Besonders interessant sind dabei superparamagnetische Co NP, da sie keine Koerzitivfeldstärke aufweisen. Sie werden in einem äußeren Magnetfeld magnetisiert und erreichen schnell ihre Sättigungsmagnetisierung, aber nach Entfernen des angelegten Magnetfelds verbleibt keine Magnetisierung. Bei biomedizinischen Anwendungen aggregieren sie daher nicht im Körper. Monodisperse magnetische Nanopartikel werden üblicherweise durch die Zersetzung von metallischen Vorstufen bei hohen Temperaturen hergestellt, wobei Größe und Form variiert werden können. Häufig werden hydrophobe Liganden wie OA, TOPO und Oleylamin verwendet, um sowohl das Wachsen der NP zu kontrollieren als auch ihr Aggregieren zu verhindern. Die magnetischen Nanopartikel können für biologische Anwendungen eingesetzt werden, falls sie in ein wässriges Medium überführt werden können. Außerdem haben ihre Superkristall-Überstrukturen Potential für Anwendungen in der Datenspeicherung mit hoher Speicherdichte und elektronische Bauteile. Neben kleinen Molekülen können auch Polymere als Stabilisatoren für ferromagnetische und superparamagnetische NP verwendet werden. Kapitel 2 gibt einen Überblick über die Synthese, Oberflächenmodifizierung und Selbstassemblierung von magnetischen Nanopartikeln.

Hydrophobe Co NP, die von kleinen Molekülen stabilisiert werden, eignen sich nicht für biologische Anwendungen, für die ein hydrophiles oder wässriges Medium notwendig ist. Kapitel 3 beschreibt einen Ligandenaustausch zur Funktionalisierung von Co Nanopartikeln. Poly(*N*-Isopropylacrylamid) (PNIPAM) ist eines der am häufigsten untersuchten und eigesetzten reversibel schaltbaren Polymere mit einer unteren kritischen Lösungstemperatur (*Englisch lower critical solution temperature*, LCST) um 32 °C, bei der ein reversibler Wechsel zwischen einem hydrophoben und einem hydrophilen Zustand stattfindet. Neue Nanokomposite aus superparamagnetischen Co NP und Temperatur-responsivem PNIPAM wurden in dieser Arbeit hergestellt. Zunächst wurden wohldefinierte superparamagnetische Co NP mit OA und TOPO als Stabilisatoren durch die Thermolyse von Cobalt Carbonyl synthetisiert. Die ursprünglichen Liganden wurden dann durch einen funktionalen Liganden mit einer Amingruppe (zum Binden an die Oberfläche) und einer 2-Brompropionat-Gruppe (Polymerisationsinitiator) ersetzt. Nach dem schnellen und einfachen Prozess der Oberflächenfunktionalisierung können die Nanopartikel ohne Aggregation in dem polaren Lösungsmittel DMF dispergiert werden. FT-IR Spektroskopie hat gezeigt, dass TOPO vollständig ersetzt wurde, aber ein kleiner Teil OA auf der Oberfläche verblieb. Nach thermogravimetrischen Messungen konnte die Dichte der Initiatoren mit ungefähr 3,2 Initiatoren / nm^2

berechnet werden. Anschließend wurde Oberflächen-initiierte ATRP zur Polymerisation von NIPAM durchgeführt. Temperatur-abhängige Messungen der dynamischen Lichtstreuung der nun in Wasser dispergierbaren Nanokomposite zeigte das reversible Aggregationsverhalten nach Erhitzen über 32 °C. Die Kombination von superparamagnetischen und Temperatur-responsiven Eigenschaften in diesen hybriden Nanopartikeln ist vielversprechend für zukünftige Anwendungen z. B. in der Biomedizin.

Kapitel 4 behandelt die Untersuchung der Assemblierung von superparamagnetischen Co NP im äußeren Magnetfeld sowohl auf festen Oberflächen als auch der Flüssigkeit-Luft Grenzfläche. OA- und TOPO-stabilisierte CO NP wurden durch Thermolyse von Cobalt Carbonyl synthetisiert und entweder in Hexan oder Toluol dispergiert. Die Co NP Dispersion wurde dann auf Substrate (TEM-Grids, Siliciumwafer) und die Flüssigkeit-Luft (Wasser-Luft, Ethylenglycol-Luft) Grenzfläche getropft. Durch die anziehende dipolare Wechselwirkung bildeten sich im äußeren Magnetfeld eindimensionale (1-D) Ketten. Es ist bekannt, dass die Konzentration der Dispersion und die Stärke des Magnetfelds die Assemblierung von superparamagnetischen Co NP beeinflussen. Daher wurde der Einfluss beider Parameter auf die Morphologie der assemblierten Strukturen untersucht. Bei niedrigerer Konzentration der Dispersion und geringerer Magnetfeldstärke bildeten sich kurze und flexible Ketten. Bei höherer Konzentration oder höherer Magnetfeldstärke wurden die Ketten länger, breiter und gerader. Eine höhere Konzentration führt voraussichtlich zu einem höheren Anteil an kurzen Ketten und deren Wechselwirkung zu längeren und dickeren Ketten im äußeren Magnetfeld. Andererseits sind die induzierten magnetischen Momente bei erhöhter Magnetfeldstärke größer und dominieren über die thermische Fluktuation. Daher verbinden sich die kurzen Ketten zu längeren, und dickere Ketten entstehen durch Interaktion benachbarter Ketten. Außerdem zeigen die induzierten Momente der NP verstärkt in die gleiche Richtung je größer das äußere Magnetfeld ist, weshalb die Ketten gerader werden. Im Vergleich der Assemblierung auf Substraten an der Wasser-Luft und Ethylenglycol-Luft Grenzfläche, zeigte die Assemblierung von Co NP aus Hexan-Dispersion an der Ethylenglycol-Luft Grenzfläche die geordnetsten und homogensten Strukturen. Die Assemblierung von superparamagnetischen Nanopartikeln im äußeren Magnetfeld könnte sich zu einem leistungsfähigen Ansatz für die Datenspeicherung und für elektronische Bauteile entwickeln.

Kapitel 5 präsentierte die Synthese von superparamagnetischen und ferromagnetischen Cobalt Nanopartikeln durch die zwei-stufige Thermolyse von Cobalt Carbonyl ($Co_2(CO)_8$) mit Polystyrol als Stabilisator. Polystyrol Polymere mit Amin-Endgruppen wurden durch ATRP-Technik mit unterschiedlichen Molekulargewichten hergestellt. Das Molekulargewicht wurde durch Gel-Permeations-Chromatographie (GPC) und MALDI-ToF (*Englisch matrix-assisted laser desorption/ionization time-of-flight*) Massenspektrometrie bestimmt. Bei enger Molekulargewichtsverteilung ($Mw/Mn<1.2$) zeigten GPC und MALDI-ToF MS nahezu gleiche Ergebnisse. Beispielsweise wurde 10600 Da durch MALDI-ToF MS erhalten, während GPC 10500 g/mol ($Mw/Mn = 1.17$) ergab. Bei einer breiten Molekulargewichtsverteilung kann man mit MALDI-ToF MS jedoch kein präzises Ergebnis erzielen. So wurden bei einem Polymer ein Molekulargewicht von 3130 Da mit MALDI-ToF MS gemessen, während GPC zu 2300 g/mol ($Mw/Mn = 1.38$) führte. Die Größe, Größenverteilung und magnetischen Eigenschaften der hybriden Partikel haben sich mit dem Molekulargewicht und der Konzentration der

Polymer-Stabilisatoren unterschieden. Eine Analyse mit Transmissionselektronenmikroskopie zeigte, dass die Größe der Co NP zwischen 12–22 nm variierte, wenn sie durch Polystyrol geringen Molekulargewichts (Mn = 2300 g/mol) stabilisiert wurden, während sich die Größe der Partikel mit Polystyrol mittleren (Mn = 4500 g/mol) und höheren (Mn = 10500 g/mol) Molekulargewichts kaum unterschied. Messungen der magnetischen Eigenschaften zeigten, dass die kleinen Cobalt Partikel (12 nm) superparamagnetisch waren, während größere Partikel (21 nm) ferromagnetisch waren und zu 1-D Ketten assemblierten. Die Dichte der Polymere auf der Oberfläche wurde nach einer thermogravimetrischen Analyse berechnet. Mit kleinem Molekulargewicht (Mn = 2300 g/mol) wurde eine höhere Dichte erreicht als mit hohem Molekulargewicht (Mn = 10500 g/mol). Durch eine stärker ausgeprägte sterische Hinderung kann ein Polymer hohen Molekulargewichts keine dichte Hülle um die Nanopartikel bilden. Das Vorliegen einer epsilon kristallinen Phase wurde durch Weitwinkel-Röntgenstreuung sowohl für superparamagnetische Co NP (mit PS Mn = 2300 g/mol) als auch ferromagnetische Co NP (mit PS Mn = 10500 g/mol) bestimmt. Die PS-Co NP, die mit einer höheren Konzentration und einem höheren Molekulargewicht des Polymers hergestellt wurden, zeigten eine höhere Stabilität über 3 Wochen.

In Zukunft sind drei Themengebiete weiterhin von besonderem Interesse. Erstens, kann der Einsatz von monodispersen superparamagnetischen Co NP für biologische Anwendungen näher untersucht werden. Die Oberflächenmodifikation bietet dabei ein generelles Konzept für die Funktionalisierung von ursprünglich hydrophoben Co NP. Beispielsweise können funktionale Biomoleküle wie Aminosäuren, Enzyme und Peptide – durch die Vielfalt an –COOH und -NH_2 Gruppen, die eine hohe Affinität zur Co NP Oberfläche haben – für den Ligandenaustausch verwendet werden. Superparamagnetische Co NP werden im Körper nach Wegnehmen des äußeren Magnetfelds nicht aggregieren. Außerdem können die Biomoleküle durch einen Magneten recycelt werden, wenn sie an Co NP gebunden sind. Zweitens, ferromagnetische Co NP assemblieren durch Dipol-Dipol Wechselwirkung zu 1-D Ketten. Thermoresponsive Polymere zeigen einen Phasenübergang bei entsprechender Temperaturänderung. Die Selbstassemblierung ferromagnetischer Co NP kann mithilfe einer dicken Schicht eines solchen Temperatur-responsiven Polymers und der Temperatur beeinflusst werden. PNIPAM hat beispielsweise eine untere kritische Lösungstemperatur (*Englisch lower critical solution temperature*, LCST) um 32 °C. Ein Mikrogel Co@PNIPAM mit einer verlinkten PNIPAM-Schicht um die Co NP würde unterhalb der Volumen-Phasenübergangstemperatur (*Englisch volume phase transition temperature*, VPTT) in Wasser schwellen und oberhalb kollabieren. Bei einem großen Volumen der geschwollenen PNIPAM-Schicht könnte die dipolare Wechselwirkung zwischen den Co NP unterbunden werden und die Mikrogele Co@PNIPAM wären zufällig verteilt statt einer Kettenstruktur auszubilden. Bei höherer Temperatur als der VPTT schrumpft die Polymerschicht, so dass der Abstand der NP kleiner wird und 1-D Ketten durch dipolare Wechselwirkung ausgebildet werden können. Drittens, durch ihre katalytischen Eigenschaften können Co NP verwendet werden, um Reaktionen in organischen und wässrigen Medien zu katalysieren. Die Verwendung von magnetischen Co NP als Katalysatoren bietet mehrere Vorteile. Einerseits können die katalytischen Eigenschaften durch Stimuli-responsive Polymere wie Thermo-, pH- und Licht-responsive Polymere kontrolliert werden. Mit PNIPAM als Beispiel könnte die katalytische Effizienz von

Co@PNIPAM Kern-Schale Nanoreaktoren durch die Temperatur gesteuert werden. Bei einer Temperatur unter der VPTT ist das Gel in Wasser geschwollen und die Substrate können zur Oberfläche der Co NP diffundieren; die Reaktionsrate ist also hoch. Bei Temperaturerhöhung über die VPTT ist die Polymerschicht jedoch hydrophob, wodurch die Moleküle die Co NP nicht erreichen können und die Katalyse nicht ablaufen kann. Andererseits können die magnetischen Co NP Katalysatoren durch einen Magneten recycelt werden, so dass die Umweltbelastung reduziert wird.

8 Acknowledgement

At the end of the thesis, I would like to express my sincere gratitude to many people for their support and encouragement during my scientific work.

Firstly, I am very grateful for Professor Dr. Alexander Böker to offer me the opportunity to pursue my PhD study. I sincerely appreciate him for his generous support, enthusiastic encouragement and professional mentoring in the development of my research work.

I am thankful to Dr. Ulrich Glebe, my daily guide and supervisor, who is always helpful in every area of my work. His diligent and meticulous approach towards my experimental work and optimistic attitude towards life inspires me a lot. Whenever I have questions about my work, he is always willing to take his time to discuss with me and offer suggestions.

I also want to express my thanks to Dr. Bing Liu, who initiated my thesis topic and shared a lot of scientific ideas and suggestions about my work. Although we only worked together for one year in Germany, I learned a lot from his diligent and critical scientific attitude spirit. We even discussed about my work through Skype when he was in China.

In addition, I would give my thanks and appreciation to China Scholarship Council (CSC) for the financial support of my PhD study in Germany.

I would like to thank Marc Zimmermann for teaching me how to use AFM and optical microscopy. I would also thank Tatjana.Egorov-Brening to offer access to glove box in her lab. I am thankful to Dr. Konrad Siemensmeyer for magnetic measurement; Dr. Andreas Holländer for XPS mearuements; Dr. Erik Wischerhoff for GPC measurements; Mrs. Kathrin Jesse for TGA measurements; Dr. Andreas Bohn for XRD measurements and Mrs. Steffi Grunst for SEM measurements. I would also like to thank my former colleague Himanshu Charan, who is humorous, helpful and always keeps me motivated.

I express my cheerful thank to my Chinese friends here in Fraunhofer IAP. Lynn always organizes activities and shares delicious food. Xuepu Wang, Shuhao Zhang and Xiao Cheng are always good partners to discuss work and life. I would like to thank all my friends and colleagues in Fraunhofer IAP.

Last but most sincerely, I am so grateful to my family: my mother, my father, my sisters and grandparents. Specifically, I would like to thank my boyfriend Wu Wang. He is also a PhD student in Karlsruhe, he gives me generous encouragement, understanding and help during my PhD study. Thank you for your unconditional love.